Title
Electronic, Vibrational and Thermoelectric Properties of Two-Dimensional Materials

Permalink
https://escholarship.org/uc/item/3d88b13x

Author
Wickramaratne, Darshana

Publication Date
2015

Peer reviewed|Thesis/dissertation

UNIVERSITY OF CALIFORNIA
RIVERSIDE

Electronic, Vibrational and Thermoelectric Properties of Two-Dimensional
Materials

A Dissertation submitted in partial satisfaction
of the requirements for the degree of

Doctor of Philosophy

in

Electrical Engineering

by

Darshana Wickramaratne

June 2015

Dissertation Committee:
      Dr. Roger K. Lake, Chairperson
      Dr. Alexander A. Balandin
      Dr. Chun Ning (Jeanie) Lau

The Dissertation of Darshana Wickramaratne is approved:

_____

_____

_____

Committee Chairperson

University of California, Riverside

Acknowledgments

I thank my advisor, Professor Roger K. Lake, for accepting me into his group and teaching me so much about materials physics, device modeling and scientific writing. As a student in Roger's group, he always made himself available for discussions on research and constantly provided guidance and support. I acknowledge support and guidance from Prof. Alexander Balandin and Prof. Jeanie Lau for allowing me to collaborate with their respective groups, valuable discussions on our collaborative research projects and for providing feedback during the dissertation process.

I am grateful for the opportunity I had to collaborate and discuss research with Dr. Ferdows Zahid, Dr. Mahesh Neupane, Dr. Yafis Barlas, Mr. Gen Yin, Mr. Rameez Samnakay, Mr. Zafer Mutlu and Dr. Shamsul Arafin. I thank Dr. Christian Witt and Dr. Marcelo Kuroda for the support and training I received at IBM Yorktown Heights and GLOBALFOUNDRIES as a 2013 summer intern. A special thanks to the members of the LAboratory for Terascale and Terahertz Electronics (LATTE) for their advice, support and many informal discussions during my PhD.

On the personal side I would like to acknowledge my friends and family for their continuous support over the past few years. To my parents, Nimal and Nilanthi Wickramaratne, and my sister, Anushka, I am thankful for their guidance and support of my education throughout these years. Last but not least, I would like to thank my wife, Priti Wickramaratne, who has unconditionally supported me throughout my

PhD.

The text of this dissertation, in part or in full, is a reprint of the material as it appears in the following journals:

- Journal of Chemical Physics [1]. Reprinted with permission from [1]. ©[2014]. American Institute of Physics

- Nano Letters [2]. Reprinted with permission from [2]. ©[2015]. American Chemical Society

ABSTRACT OF THE DISSERTATION

Electronic, Vibrational and Thermoelectric Properties of Two-Dimensional
Materials

by

Darshana Wickramaratne

Doctor of Philosophy, Graduate Program in Electrical Engineering
University of California, Riverside, June 2015
Dr. Roger Lake, Chairperson

The discovery of graphene's unique electronic and thermal properties has moti-
vated the search for new two-dimensional materials. Examples of these materials
include the layered two-dimensional transition metal dichalcogenides (TMDC) and
metal mono-chalcogenides. The properties of the TMDCs (eg. MoS_2, WS_2, TaS_2,
$TaSe_2$) and the metal mono-chalcogenides (eg. GaSe, InSe, SnS) are diverse - ranging
from semiconducting, semi-metallic and metallic. Many of these materials exhibit
strongly correlated phenomena and exotic collective states such as exciton conden-
sates, charge density waves, Lifshitz transitions and superconductivity. These prop-
erties change as the film thickness is reduced down to a few monolayers.

We use first-principles simulations to discuss changes in the electronic and the
vibrational properties of these materials as the film thickness evolves from a single
atomic monolayer to the bulk limit. In the semiconducting TMDCs (MoS_2, $MoSe_2$,
WS_2 and WSe_2) and monochalcogenides (GaS, GaSe, InS and InSe) we show con-
fining these materials to their monolayer limit introduces large band degeneracies or
non-parabolic features in the electronic structure. These changes in the electronic

structure results in increases in the density of states and the number of conducting modes. Our first-principles simulations combined with a Landauer approach show these changes can lead to large enhancements up to an order of magnitude in the thermoelectric performance of these materials when compared to their bulk structure.

Few monolayers of the TMDCs can be misoriented with respect to each other due to the weak van-der-Waals (vdW) force at the interface of two monolayers. Misorientation of the bilayer semiconducting TMDCs increases the interlayer van-der-Waals gap distance, reduces the interlayer coupling and leads to an increase in the magnitude of the indirect bandgap by up to 100 meV compared to the registered bilayer.

In the semi-metallic and metallic TMDC compounds ($TiSe_2$, TaS_2, $TaSe_2$) a phase transition to a charge density wave (CDW) ground state occurs at a temperature that is unique to each material. Confining these materials to a single monolayer or few-monolayers can increase or decrease their CDW transition temperature and change the magnitude of the CDW energy gap. We show the low energy Raman modes observed in 1T-$TaSe_2$ and 1T-TaS_2 in their CDW ground state can emerge from zone folded phonons due to the reconstruction of the lattice in the bulk and monolayer structures. In 1T-$TiSe_2$ the driving mechanism of the CDW is excitonic condensation. We show the excitonic gap of the monolayer and bilayer structures can increase by up to a factor of 3 compared to the excitonic gap of the bulk structure. The results from the studies conducted on these materials are currently hosted on an open-access repository sponsored by the University of California Curation Center (UC3).

Contents

List of Tables

List of Figures

xxiv

Chapter 1

Rationale

1.1 Introduction

The continued down-scaling of metal oxide semiconductor (MOS) field effect transistors (MOSFETs) in accordance with Moore's Law has enabled increasingly faster, highly-functional and low form factor electronic devices. A number of projections have suggested the ultimate limit silicon MOSFETs can be scaled down to is 5 nm channel lengths. [17–19] One of the solutions to the continued downscaling of transistors is the use of alternative channel materials to scale beyond the technology roadmap of 5nm. Two dimensional van-der-Waal (vdW) materials have been invoked as a possible solution to overcome the scaling challenges faced by using silicon MOSFETs. [18]

Graphene is the prototypical two dimensional vdW material that has served as a platform to study a variety of fundamental physics and device applications at the atomic two dimensional limit. This has also spurred research into a variety of other two dimensional layered materials beyond graphene. Each of these two dimensional materials has unique electronic and vibrational properties that quantitatively change when their film thickness is reduced to a single monolayer. While reducing dimen-

sionality can either enhance or reduce the lattice thermal conductivity and electrical conductivity of each material, real applications that utilize these properties require a finite cross section of material. We would like to enjoy the benefits of the special properties of an atomically thin two dimensional material and also have a finite cross section of material to transport a useful amount of heat or current. Hence, understanding the electronic, vibrational and thermoelectric properties of these two dimensional materials as their film thickness changes from the bulk to the monolayer limit is one of the primary objectives of this work. In the following sections we briefly introduce the different materials studied and the different phenomena investigated in this work and explain the formalism in later chapters.

1.1.1 Two-dimensional layered metal chalcogenides

The two dimensional transition metal dichalcogenides and metal monochalcogenides are an attractive candidate family of materials that may provide a solution to the search for alternative channel materials for CMOS devices. Two dimensional materials have been shown both experimentally and theoretically to have electronic, optical, mechanical and thermal properties that are superior to the behavior of these materials in their bulk form. [20, 21] The self passivated surfaces of these materials also makes it feasible to integrate heterostructures using different two dimensional materials and overcome limitations of dangling bonds associated with the growth and integration of unpassivated surfaces. [22, 23]

Beyond graphene, examples of new layered materials that have been discovered include the transition metal dichalcogenides [20], metal monochalcogenides [24], hexagonal-boron nitride [25], lead halides [26], bismuth and antimony selenides and tellurides [11], black phosphorus [27], transition metal carbides (MXene) [28] and the

group IV analogues of graphene (silicene and germanene) [29, 30] Illustrated below is a panel of some of the materials that will be investigated in this work. Each of these
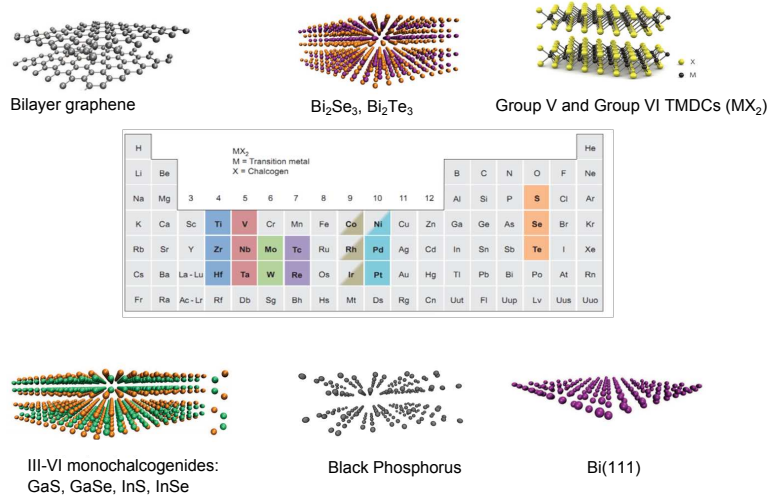
Figure 1.1: Range of two dimensional layered materials that are explored in this study. Their properties vary based on the choice of element from the periodic table and the registry between individual atomic planes. The image of the periodic table is reproduced with permission from [16] ©[2013] Nature Chemistry

materials listed above and illustrated in Figure 1.1 exhibit a wide range of structural, electronic, vibrational, optical and mechanical phenomena.

Studies of the transition metal dichalcogenides (TMDCs) and metal monochalcogenides predates the research that was conducted on graphene. Studies on these layered metal chalcogenide (LMC) materials can be found dating back to the 1950s. The first report on earth abundant MoS_2 dates back to 1953 with intercalation studies on bulk MoS_2. [31] The metallic and semi-metallic LMCs were the focus of several studies in the 1970s with the identification of superconducting and charge density wave phenomena in these materials. [15, 32] Intercalation studies were also conducted to understand the potential for using the layered dichalcogenides as materials for energy storage. [33] These experiments were complemented by the emergence of electronic structure calculations of a number of LMC compounds. [34] In 2004, the first

top gated thin film WSe_2 transistor was fabricated, with the proposal of applying LMCs for flexible electronics. [35] This was followed by transport studies on MoS_2 and TaS_2 nanopatches by Ayari et al. in 2007. [36] The first experimental investigations of transport in monolayer MoS_2 were published in 2010 by Andras Kis et al. [37] This was followed by the first demonstration of strong enhancement in the photoluminesence by Galli et. al and Heinz et. al when MoS_2 was reduced in thickness down to a single monolayer. [38, 39] These initial results on monolayer MoS_2 have resulted in a continuous increase in the number of publications that focus on the study of the layered metal chalcogenides and their various heterostructures.

The crystal structure and bonding in the layered metal chalcogenides is characterized by strong covalent or ionic bonding along the basal plane and weak bonding out of plane where the individual atomic planes are held together by weak van-der-Waal forces. The weak forces along the c-axis of this class of materials allows individual layers of these materials to be separated with relative ease either through mechanical or liquid exfoliation. The senstivity of the electronic structure of this class of materials to interlayer coupling means the properties of these materials qualitatively changes as their thickness approaches the monolayer limit. A number of other structural degrees of freedom can also alter the electronic properties of the layered materials. The layered materials can exist in a number of different stacking orders due to the weak forces between the individual monolayers. The different stacking configurations are a host to a wide variety of electronic properties.

In the transition metal dichalcogenides, the different stacking orders can alter the crystal field splitting of the transition metal d-orbital thus giving rise to different d-orbital physics. [40] For example in the TMDCs, the d-bands of the transition metal are split by the crystal field based on their coordination environment with respect to the chalcogen atoms. When the transition metal atoms are octahedrally coordinated

4

the d bands split into a e_g ($d_z{}^z$, $d_{x^2-y^2}$) and t_{2g} (d_{yz}, d_{xy}, d_{xz}) manifold. When the transition metal atom has trigonal prismatic coordination the the d-bands split into three manifolds of A1' (d_{z^2}), E' ($d_{x^2-y^2}$, d_{xy}) and E"(d_{xz}, d_{yz}). This simple ionic picture provides a qualitative understanding for the range of electronic properties observed in the TMDCs. The different degrees of structural freedom and the choice of metal and chalcogen atom give rise to different electronic and vibrational properties and phenomena in this family of materials. The changes in the electronic structure and phonon dispersions for a range of layered metal chalcogenide materials is studied using ab-initio calculations as these materials are confined from their bulk structure to a single monolayer. The results from these calculations are used to determine the application of these materials as thermoelectrics (1.1.2) and to understand the charge density wave phenomena that is observed in the metallic and semi-metallic TMDCs (1.1.3).

1.1.2   Thermoelectrics

One approach to improve the energy storage and conversion capabilities of a material has been to rely on nanostructuring and quantum confinement induced effects. Thermoelectric materials are a class of materials that may offer a possible solution to this endeavour. When a temperature gradient is maintained across a thermoelectric material, an electrostatic potential develops across the material which can be used to do work. This conversion of heat to electric potential is the Seebeck coefficient. In the state of art thermoelectric materials such as Bi_2Te_3 the maximum Seebeck coefficient is often $\sim 200\mu VK^{-1}$. [41] The performance of a material as a thermoelectric is

determined by its thermoelectric figure-of-merit, ZT. ZT is defined as

$$ZT = \frac{S^2 \sigma T}{\kappa_e \kappa_l} \qquad (1.1)$$

where S is the Seebeck coefficient, σ is the electrical conductivity, κ_e is the contribution of the electrons to the thermal conductivity, κ_l is the lattice thermal conductivity and T is the temperature at which the figure-of-merit is calculated. An ideal thermoelectric would thus have large electrical conductivity and low thermal conductivity. However these are competing effects and hence a considerable amount of effort is spent optimizing materials to maximize ZT or identifying materials where the desired properties are intrinsically present within the material. [42]

Motivated by the Hicks and Dresslhaus proposal that the thermoelectric figure of merit can be enhanced in quantum well superlattices [43], there have been a number of studies focused on identifying appropriate thin film thermoelectric materials. One of the most widely used thermoelectric material, Bi_2Te_3, is also a van-der-Waal material. Recent theoretical studies have predicted a single quintuple layer of Bi_2Te_3 can have a ZT up to 7 at room temperature. [44, 45] To understand if this large enhancement in ZT due to confinement translates to other layered materials, we study the thermoelectric properties in a variety of van-der-Waal materials as a function of film thickness. In these materials we investigate the influence of higher band degeneracy and non-parabolic bands on the thermoelectric response of each material. The electronic structure for each material computed using density functional theory is used to determine the thermoelectric response of each material.

1.1.3 Charge Density Waves

A charge density wave (CDW) is a phase transition that spontaneously occurs in metallic and semi-metallic materials. In a CDW, metallic electrons condense into a collective ground state with a periodic modulation of the charge density resulting in a single-particle energy gap 2Δ at the Fermi surface. Electrical conductors with a quasi-one dimensional structure were first predicted to undergo a phase transition to a charge density wave state. The appearance of a CDW state in quasi-1D materials is driven by a Peierls instability. [46] The lattice of atoms undergoes a periodic distortion and the electrons condense into a ground state with a periodic modulation of the charge density. Figure 1.2 illustrates the formation of a charge density wave in a one dimensional lattice.
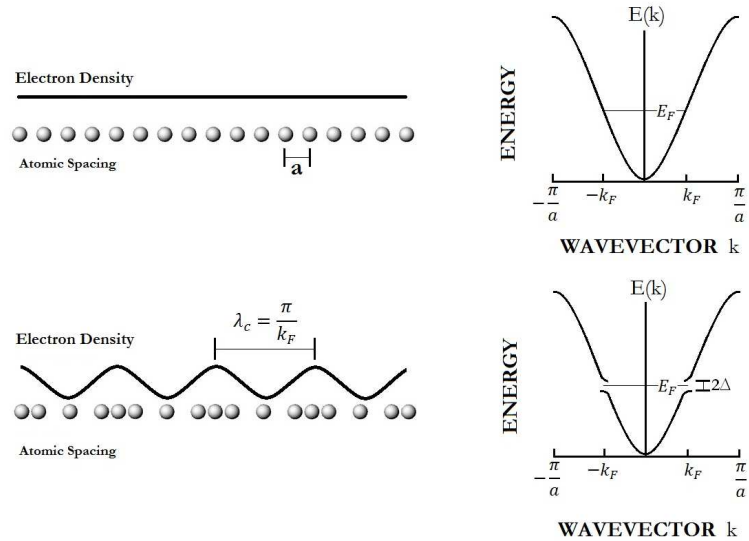
Figure 1.2: Illustration of the formation of the charge-density wave (CDW). Some materials (a) can reduce their energy by developing CDW as shown in (b).The charge-density wave is the couple modulation of the conduction electron density and the atomic positions. The modulations produce an energy gap 2Δ at the Fermi surface.

The presence of charge density waves have also been observed and characterized in a number of metallic two dimensional Group IV and Group V transition metal

dichalcogenides. The commensurate CDW transition in this family of materials results in a periodic distortion of the lattice and either a partial or complete gapping of the Fermi surface. The charge density wave transition in these materials is characterized by a unique transition temperature and a driving mechanism that is unique to each material. For example, it was suggested that CDW transition in $TiSe_2$ is driven by a transition to an excitonic insulating phase [47]. In 1T-TaS_2 and 1T-$TaSe_2$ ARPES experiments have shown partial gapping of the Fermi surface but the origin of the transition is still a subject of debate [48, 49]. In 2H-$NbSe_2$ the Fermi surface nesting was recently questioned as the origin of the CDW [50] while the origin of the exact mechanism still remains a subject of debate.

The CDW transition that occurs in these materials results in experimental signatures that are unique to each material. In the commensurate CDW transition, the periodic distortion of the lattice results in a number of new low energy modes in the Raman spectra. [51] In 1T-TaS_2 and 1T-$TiSe_2$ the gapped Fermi surface in the commensurate CDW phase gives rise to sharp increases in resistivity at the commensurate CDW transition temperature. [52, 53] Using ab-initio calculations we calculate the electronic properties and vibrational properties of 1T-$TaSe_2$ and 1T-$TiSe_2$. The results of these simulations are used to support the experimental Raman spectroscopy results of our collaborators and to understand the driving mechanism of the CDW transition in 1T-$TiSe_2$ as a function of film thickness.

1.2 Objective

The adoption and use of two dimensional layered materials in present day technology is still in its nascent stage. The electronic and vibrational properties of the layered metal chalcogenides as the film thickness changes from bulk to a single monolayer

is currently not known for a number of these materials. Currently, most studies are focused on either the bulk properties of these materials or the properties of a single monolayer. Extrapolating the electronic, optical and thermal properties based on studies at these two extremes may provide qualitatively incorrect trends and results. Hence, the objectives of this dissertation are:

1. Understand quantitative changes in the electronic structure of the Group VI semiconducting transition metal dichalcogenides MoS_2, $MoSe_2$, WS_2 and WSe_2 as the film thickness is reduced from bulk to a single monolayer.

2. Determine the impact of changes in the electronic structure of the Group VI TMDCs as a function of film thickness on the thermoelectric properties of each material

3. Understand changes in the Fermi ring that exists at the band extrema in a number of van-der-Waal materials as a function of film thickness. Determine the impact of the Fermi ring on the thermoelectric properties of a material and compare to the thermoelectric response of a parabolic band material.

4. Understand changes in the electronic and vibrational properties of the bulk and monolayer Group IV and Group V TMDCs due to the periodic lattice distortion that follows a commensurate CDW transition

1.3   Layout

The rest of this dissertation is organized as follows. In Chapter 2 a background of density functional theory (DFT) and the different approaches used with DFT is presented. In Chapter 3 a systematic study of the electronic properties of MoS_2, $MoSe_2$,

WS$_2$ and WSe$_2$ as the film thickness is confined from bulk to a single monolayer is presented. The thermoelectric properties as the film thickness transitions from bulk to monolayer for four of the TMDCs is also discussed extensively in Chapter 3 In Chapter 4 the electronic properties of misoriented bilayers of MoS$_2$, MoSe$_2$, WS$_2$ and WSe$_2$ is studied. In Chapter 5 we extend our study of the electronic and thermoelectric properties of van-der-Waal materials to study vdW materials that exhibit a Fermi ring in their band extrema. The evolution of this Fermi ring as a function of film thickness and the impact on the thermoelectric performance of these materials is studied in detail. In Chapter 6 we study the electronic and vibrational properties of the metallic transition metal dichalcogenides which exhibit a charge density wave transition. Experimental Raman spectroscopy has shown the the lattice distortion that follows a charge density wave transition results in the occurence of a number of low energy zone folded modes. We study the origin of these zone folded modes for two metallic TMDC compounds in their bulk and monolayer limits. Finally in Chapter 7 we summarize the key findings of this thesis. In Appendix A we summarize additional calculation results of the Group VI TMDCs (MoS$_2$, MoSe$_2$, WS$_2$ and WSe$_2$) obtained using hybrid functional DFT calculations. In Appendix C the MATLAB code used to numerically calculate the density of modes from the ab-initio calculations of the band structure of a material is given.

Chapter 2

Theoretical Methods

2.1 Density Functional Theory

Density functional theory is one of the most widely used methods to describe the properties of condensed matter systems. In addition to being applied to studies of standard bulk materials, DFT has been successfully applied to study complex materials and structures such as molecules, proteins, surfaces and their heterostructures. The standard quantum-mechanical approach to model the electronic properties of a many-electron problem (such as the systems listed above) requires a Hamiltonian for the given system. For a system of electrons and nuclei, the Hamiltonian (H) will be:

$$H = \hat{T} + \hat{V}_{ext} + \hat{V}_{int} + E_{nn} \tag{2.1}$$

where $\hat{T}$ is the electronic kinetic energy, $\hat{V}_{ext}$ is the potential due to the electron-nuclei interactions, $\hat{V}_{int}$ is the potential due to electron-electron interactions and E_{nn} is the interaction between nuclei. Density functional theory allows this many-electron wavefunction problem to be solved in practice. The basis of density functional the-

ory are the Hohenberg-Kohn (HK) theorems. [54] The first HK theorem proves the ground-state of a many-electron system can be uniquely determined by the electron density of the system. The second HK theory states the total ground-state energy of such a many-electron system is a functional of the ground-state electron density. For a given $\hat{V}_{ext}$, the total energy functional is:

$$E[n] = T[n] + E_{int}[n] + \int d^3 r V_{ext}(r) n(r) + E_{nn} \tag{2.2}$$

where T[n] is the kinetic energy, E_{int}[n] is the interaction energy of the electrons, V_{ext} is the external potential acting on the electrons from the nuclei.

The approach outlined by the Kohn-Sham approach [55] made the HK theorems computationally tractable. The Kohn-Sham approaches replaces the many-body electron wave function with a non-interacting system in an effective potential that has a ground state density that is identical to that of the many body interacting system. The effective Hamiltonian of the non-interacting particles in the Kohn-Sham is defined as:

$$V_{KS}(r) = V_{ext}(r) + V_H(r) + V_{XC}(r) \tag{2.3}$$

where V_{ext} is the external potential acting on the electrons due to the nuclei defined as:

$$V_{ext}(r) = \sum_n \frac{-Z_n e}{|r_n - r_e|} \tag{2.4}$$

where Z_n is the nuclear charge and r_n is the position of the nuclei. V_H(r) is the Hartree potential given by:

$$V_H = \int \frac{\rho(r)}{|r - r_e|} dr \tag{2.5}$$

which is just the Coulomb interaction between electrons. V_{XC}(r) is the exchange-correlation potential which includes electron-electron interactions not included in the

Hartree potential. Two common approaches to approximate the exchange correlation potential include the Local Density Approximation (LDA) and the Generalized Gradient Approximation (GGA). The main rationale behind these approximations is that for electron densities within a solid, exchange and correlation effects occur on a short length scale. Hence, LDA and GGA approximations of DFT accurately describe the properties of materials that resemble a homogeneous electron gas.

Approximating the exchange correlation potential using either the LDA or GGA approximation has shortcomings when describing the properties of semiconducting materials. The most well known problem is the band gaps of semiconductors and insulators are significantly underestimated by LDA and GGA calculations. For a number of semiconducting materials, LDA or GGA calculations can predict metallic behavior as well. In addition to incorrect descriptions of bandgaps, LDA and GGA calculations can also lead to inaccurate description of band-offsets, lattice constants and effective masses. These shortcomings can affect quantitative and qualitative predictions of properties such as the thermoelectric response or transistor transfer characteristics that use ab-initio calculations of a semiconducting material at the LDA or GGA level. To overcome this limitation more advanced theoretical approaches have been used in DFT calculations to overcome the *band-gap* problem. The approach used in this study is the inclusion of exact-exchange in the exchange-correlation functional using hybrid functionals, specifically the Heyd-Scuseria-Ernzerhof (HSE) functional.

2.1.1 Hybrid functional DFT calculations

Recent advances in density functional theory have led to the development of methods that overcome the underestimated bandgap often predicted using standard exchange correlation approximations such as LDA or GGA. One common approach is the use of

range separated hybrid functionals which include an amount of exact exchange within the exchange-correlation approximation. In this work we use the hybrid function implemented by Heyd, Scuseria and Ernerhof (HSE) to correct for the underestimated bandgaps and band offsets predicted by our GGA level calculations.

Hybrid functionals first proposed by Axel Becke in 1993 were proposed to mix either a LDA or GGA DFT calculation with an orbital dependent Hartree-Fock calculation. In the Hartree-Fock calculation, the many-electron wave function of the system is calculated using a single Slater determinant constructed using single particle orbitals combined in anti-symmetric approached. The many electron Hartree Fock wave function is defined as:

$$\psi_{HF}(r_1, r_2, r_3, \ldots, r_N) = \frac{1}{\sqrt{N!}} \begin{bmatrix} \psi_1(r_1) & \psi_2(r_2) & \psi_3(r_3) & \ldots & \psi_1(r_N) \\ \psi_2(r_1) & \psi_2(r_2) & \psi_3(r_3) & \ldots & \psi_2(r_N) \\ \vdots & \vdots & \vdots & & \vdots \\ \psi_N(r_1) & \psi_N(r_2) & \psi_N(r_3) & \ldots & \psi_N(r_N) \end{bmatrix} \tag{2.6}$$

Hence the single-particle Hartree Fock Hamiltonian is

$$H = \frac{-\Delta^2}{2m_e} + V_{ext} + V_{Hartree} + V_X^{HF} \tag{2.7}$$

where $V_{Hartree}$ is defined is the direct interaction between electrons and V_X^{HF} is the Hartree-Fock exact exchange that only acts on electrons of the same spin. A hybrid-functional DFT calculation mixes a fraction of exact Hartree-Fock exchange with a LDA or GGA functional. This allows the Kohn-Sham Hamiltonian to be re-written as

$$H = \frac{-\Delta^2}{2m_e} + V_{ext} + V_{Hartree} + V_{XC} + \alpha(V_X^{HF} + V_X^{DFT}) \tag{2.8}$$

The HSE hybrid functional we use in this study mixes screened Hartree Fock exchange with a GGA exchange-correlation functional implemented by Perdew-Burke and Ernzerhof (PBE). The exchange interaction in the HSE functional is separated into short-range (SR) and long-rang (LR) interaction components using an error function

$$\frac{1}{r} = \frac{erfc(\omega r)}{r} + \frac{erfc(\omega r)}{r} \tag{2.9}$$

where ω is the range-separation. In the default HSE calculation, HSE06, the PBE exchange correlation approximation is mixed with screened Hartree-Fock exchange in a 3 to 1 ratio for the SR interactions. The long-range exchange and correlation interactions are described by the PBE functional. Hence the exchange correlation Hamiltonian for the HSE06 function can be defined as

$$H_{XC}^{HSE06} = \frac{1}{4}E_X^{HF,SR}(\omega) + \frac{3}{4}E_X^{PBE,SR}(\omega) + E_X^{PBE,LR}(\omega) + E_C^{PBE} \tag{2.10}$$

where E_C^{PBE} is the correlation energy from the PBE functional. The HSE functional has been shown in calculations of a number of semiconducting systems to reduce the band-gap error introduced by using local or semi-local approximations of DFT.

The default mixing percentage of exact Hartree-Fock exchange (25%) is suitable for most semiconducting materials in their bulk structure. However for wide-band-gap materials and for low dimensional structures the amount of exact exchange has to be tuned to match the fundamental bandgap of the material. In this work we perform ab-initio calculations of materials starting with a PBE functional and compare our results to corrections made using a hybrid HSE functional.

2.2 Density Functional Perturbation Theory

Density functional theory calculations can also be applied to calculate the first-order response of a material. In this study density functional perturbation (DFPT) was used to calculate the phonon spectra and vibrational properties of bulk and thin film structures of layered materials. Here we summarize some of the underlying approximations made in DFPT calculations, more detail reviews and discussion of the formalism and approach can be found in Ref. [56, 57]. The underlying approximation to calculate vibrational properties of materials using DFT is the Born-Oppenheimer approximation. In the Born-Oppenheimer approximation the ionic and electronic degrees of freedom of the system are decoupled, since it it assumed the electrons respond instantaneously to changes in the ionic positions. Hence, in equilibrium the forces acting on the ions can be obtained from the energy calculated with DFT.

$$\mathbf{F_I} = -\frac{\delta \mathbf{E}(\mathbf{R_I})}{\delta \mathbf{R_I}} = \mathbf{0} \tag{2.11}$$

where $\mathbf{R}_I$ is the position of the Ith ion and $\mathbf{F}_I$ is the force acting on the ion. In the harmonic approximation, the second-order derivative of the ground state energy with respect to the atomic positions is used to define the dynamical matrix and calculate the vibrational frequencies of a material.

$$det \left| \frac{1}{\sqrt{M_I M_J}} \frac{\delta^2 E(\mathbf{R_j})}{\delta R_I \delta R_J} - \omega^2 \right| = 0 \tag{2.12}$$

In DFPT second order perturbation of the DFT total energy, $\delta^2 E$ is obtained by expanding the total energy with respect to changes in the electron wave functions. Using the Hellman-Feynman theorem [56], $\delta^2 E$ and the force acting on ion I in equilibrium

is defined as:

$$F_I = -\frac{\delta E(R_I)}{\delta R_I} \qquad (2.13)$$

where ψ is the ground-state wave function. The Hamiltonian H_{ele} depends on the ionic positions $\mathbf{R}_I$ through the electron-ion interaction which couples the electronic degrees of freedom with the lattice through changes in the electron charge density, n(r). Hence, calculation of the second derivative of the total energy with respect to the ionic positions requires the ground-state charge density, n(r) and its linear response to distortion of the ionic positions, $\frac{\delta n(r)}{\delta R_J}$. Using the DFPT formalism the charge density response to perturbations can be obtained for each phonon wave vector, $\mathbf{q}$ independently. Hence, a DFPT calculation for any phonon wave vector $\mathbf{q}$ provides the phonon eigen-energies at that point in the Brillouin zone.

Chapter 3

Electronic and Thermoelectric Properties of Few-Layer Transition Metal Dichalcogenides

3.1   Introduction

Semiconducting, transition-metal dichalcogenides (TMDCs) exhibit promising electronic [37, 58–61], opto-electronic [62] and spintronic [63] properties. Single monolayers (three atomic layers) can be either exfoliated or grown with chemically stable surfaces. The electronic, optical, and spin properties of monolayers are qualitatively different from those of the bulk. The band gap changes from indirect to direct, and the valence band edges at the K and K' points become spin polarized. [62, 63] These materials are discussed in a number of recent reviews. [20, 21, 64–66]

Experimental studies conducted on a different set of two-dimensional materials, namely Bi_2Te_3 and Bi_2Se_3, demonstrated an improvement in their thermoelectric performance as their thickness was reduced. [67, 68] A large increase in ZT has been

theoretically predicted for monolayer Bi_2Te_3 compared to that of the bulk. [45,69,70] This enhancement in ZT results from the unique, step-function shape of the density of modes at the valence band edge of a single quintuple layer. [45, 70] The shape of the density of modes increases the power factor, and the increase in the power factor increases ZT. For Bi_2Te_3, the large enhancement in the power factor and in ZT only occurs for a monolayer. For bilayer and trilayer Bi_2Te_3, the step-like shape of the density of modes disappears, and the calculated values of ZT are either slightly higher [71] or slightly lower [45] than that of the bulk.

Prior experimental and theoretical investigations of the thermoelectric performance of transition metal dichalcogenides have focused on either bulk or monolayer materials. [62, 72–77]. There has not been a study of the effect of film thickness on the power factor and ZT in the transition metal dichalcogenides. It is not known whether the power factor and ZT are maximum at monolayer thickness or at some other thickness.

This work theoretically investigates the electronic properties and the thermoelectric performance of bulk and one to four monolayers of 4 different TMDC materials: MoS_2, $MoSe_2$, WS_2, and WSe_2. The goal is to understand how their electronic and thermoelectric properties vary with thickness. Similar to monolayer Bi_2Te_3, the increase in ZT for the ultrathin films results from an enhanced degeneracy or near-degeneracy of the band edges. In the TMDCs, at few layer thicknesses, different valleys become nearly degenerate with energy differences of less than k_BT at room temperature. Because of weak interlayer coupling at certain valleys, additional bands from additional layers lie within k_BT of the bandedges for few layer thicknesses. The increased degeneracy results in a sharper turn on of the the density of modes near the band edges. In all cases, the thickness with the sharpest increase in the density of modes has the largest value for ZT. For the semiconducting TMDCs considered

here, that optimum thickness is not, in general, a single monolayer.

3.2 Theoretical Methods

Ab-initio calculations of the bulk and few-layer structures (one to four layers) are carried out using density functional theory (DFT) with a projector augmented wave method [78] and the Perdew-Burke-Ernzerhof (PBE) type generalized gradient approximation [79,80] as implemented in the Vienna *ab-initio* simulation package (VASP). [81, 82] The vdW interactions in $MoSe_2$ and MoS_2 are accounted for using a semi-empirical correction to the Kohn-Sham energies when optimizing the bulk structures (optimization of WS_2 and WSe_2 structures are done at the PBE level since the semi-empirical parameters for tungsten are currently not described by the dispersion potential). [83] The Monkhorst-Pack scheme is used for the integration of the Brillouin zone with a k-mesh of 12 x 12 x 6 for the bulk structures and 12 x 12 x 1 for the thin-films. The energy cutoff of the plane wave basis is 300 eV. All of the the electronic bandstructure calculations include spin-orbit coupling. Calculations are also performed without spin-orbit coupling and the results are compared.

To verify the results of the PBE calculations, the electronic structure of 1L, 2L, 3L and 4L MoS_2 are calculated using the much more computationally expensive hybrid Heyd-Scuseria-Ernzerhof (HSE) functional. [84] The HSE calculations incorporate 25% short-range Hartree-Fock exchange. The screening parameter μ is set to 0.4 $\mathring{A}^{-1}$.

The thermoelectric parameters are calculated from a Landauer formalism using the *ab-initio* derived density of modes. [45, 70, 76] In the linear response regime, the electronic conductivity (σ), the electronic thermal conductivity (κ_e), and the Seebeck

coefficient (S) are expressed as [85, 86]

$$\sigma = (2q^2/h)I_0 \quad (\Omega^{-1}\mathrm{m}^{-1}), \tag{3.1}$$

$$\kappa_e = (2Tk_B^2/h)(I_2 - I_1^2/I_0) \quad (\mathrm{Wm}^{-1}\mathrm{K}^{-1}), \tag{3.2}$$

$$S = -(k_B/q)\frac{I_1}{I_0} \quad (\mathrm{V/K}), \tag{3.3}$$

with

$$I_j = \frac{1}{L}\int_{-\infty}^{\infty} \left(\frac{E - E_F}{k_B T}\right)^j \bar{T}(E)\left(-\frac{\partial f_0}{\partial E}\right)dE \tag{3.4}$$

where L is the device length, q is the magnitude of the electron charge, h is Planck's constant, and k_B is Boltzmann's constant. The transmission function is

$$\bar{T}(E) = T(E)M(E) \tag{3.5}$$

where M(E) as the density of modes (DOM). In the diffusive limit,

$$T(E) = \lambda(E)/L, \tag{3.6}$$

and $\lambda(E)$ is the electron mean free path. When phonon scattering is dominant, the mean free path can be written as a constant, $\lambda(E) = \lambda_0$. As discussed in Ref. [87], the transport distribution, $\Xi(E)$, arising from the Boltzmann transport equation is related to the above quantities by $\Xi(E) = \frac{2}{h}T(E)M(E)$.

The density of modes M(E) can be defined as [45, 85]

$$M(E) = \left(\frac{L_\perp}{2\pi}\right)^{d-1}\int_{BZ}\sum_{k_\perp}\Theta(E - \epsilon(k_\perp))dk_\perp^{d-1} \tag{3.7}$$

where d is the dimensionality of the system, $L_\perp$ are the dimensions of the structure

perpendicular to the direction of transport ($L_\perp^2$ = W x t for d = 3, $L_\perp$ = W for d = 2; W = width of the structure, t = film thickness), Θ is the unit step function, and $k_\perp$ refers to the k states in the first Brillouin zone perpendicular to the transport direction. Using Eq. (5.7), M(E) of any material in any dimension can be numerically evaluated from a given electronic band structure by counting the bands that cross the energy of interest. The density of modes calculations are performed by integrating over the first Brillouin zone using a converged k point grid (51 x 51 x 10 k points for the bulk structures and 51 x 51 x 1 for the thin films).

We account for carrier scattering within each structure by fitting our calculated bulk electrical conductivity with bulk experimental data. An electron mean free path of λ_0 = 14 nm gives the best agreement with experimental data on the Seebeck response of bulk MoS$_2$ as a function of the electrical conductivity. [88, 89] The bulk p-type electrical conductivity of MoS$_2$ at room temperature was reported to be 5.1 Ω^{-1}cm^{-1} with a Seebeck coefficient of $\sim$450 μVK^{-1} at a carrier concentration of 10^{16} cm^{-3}. [89] Using λ_0 = 14nm we obtain an electrical conductivity of 4.97 Ω^{-1}cm^{-1} with a Seebeck coefficient of $\sim$398 μVK^{-1} at the same carrier concentration. This value of the mean free path is also consistent with a theoretically derived energy independent acoustic phonon-limited mean free path (λ_0 = 14 nm) for electrons in monolayer MoS$_2$, [90] and was successfully used to simulate and compare to experimental results of the transfer characteristics of single layer MoS$_2$ field effect transistor. [58] As an initial approximation of carrier scattering we use the same λ_0 value to model the thermoelectric properties of all the TMDC materials investigated in this study.

For the in-plane lattice thermal conductivity, a κ_l value of 19.5 $Wm^{-1}K^{-1}$ obtained from a molecular dynamics simulation on monolayer MoS$_2$ is used. [91] Prior experimental [92] and theoretical [76] studies of the lattice thermal conductivity in the TMDC materials have demonstrated that κ_L does not vary significantly for the

different TMDC compounds studied here. With the above quantities in hand, the power factor, $S^2\sigma$, and the thermoelectric figure of merit $ZT = S^2\sigma T/(\kappa_l + \kappa_e)$ are determined.

3.3 Results

All of the thermoelectric parameters are derived from the calculated electronic band-structures. Therefore, we begin this section with a discussion of the calculated band-structures. The bandstructure calculations produce considerably more information than is required for calculating the thermoelectric parameters. To preserve that information and contribute towards a database of material parameters, extracted properties such as effective masses and energy gaps at high symmetry points are tabulated.

Figure 3.1 shows the *ab-initio* band structure of one-layer (1L) through four-layer (4L) and bulk WS$_2$.

The large valence band splitting at the K-point and the direct-indirect gap transition as the film thickness increases above 1L are features that occur in the other TMDC materials included as part of this study. The last panel in Fig. 3.1 illustrates the effect of decreasing layer thickness on the bandgap for all of the materials studied. The optimized lattice parameters of the bulk TMDC compounds are listed in Table 3.1.

The results in Table 3.1 and Figure 3.1 are consistent with prior experimental characterization [3–5] and theoretical calculations of the bulk [93,94] and thin film [95,96] crystal structures and electronic band structures. The results of these electronic
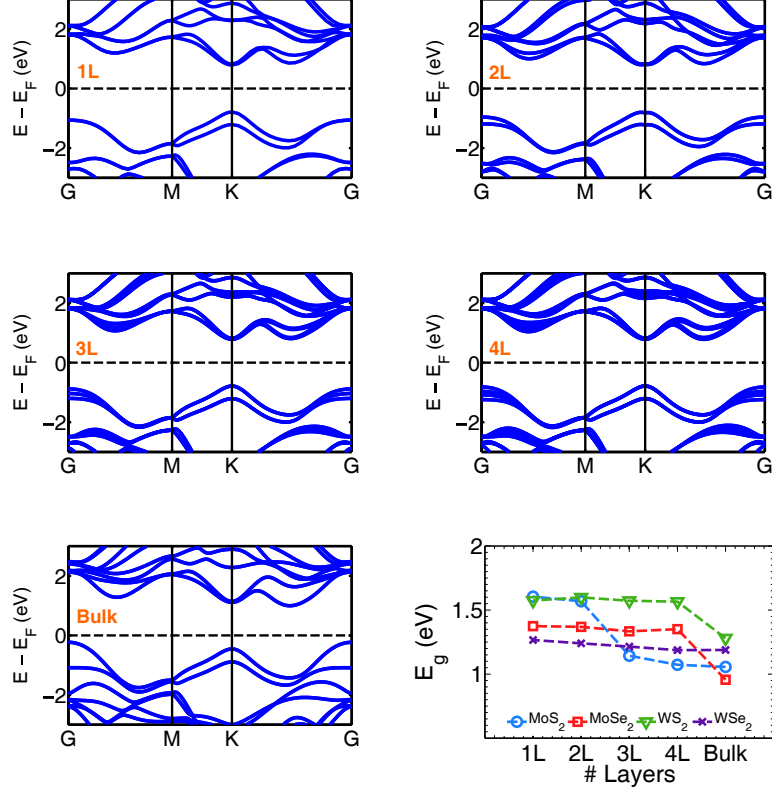
Figure 3.1: *Ab-initio* calculated band structures of WS_2: 1L, 2L, 3L, 4L and bulk. The bottom right panel illustrates the variation of the band gap of the TMDC materials as a function of the number of layers.

	$a_0(\mathring{A})$	$c_0(\mathring{A})$	z	$a_0^{expt}(\mathring{A})$	$c_0^{expt}(\mathring{A})$	z^{expt}	$E_g(eV)$	$E_g^{expt}(eV)$
MoS_2	3.179	12.729	0.627	3.160	12.290	0.629	1.060	1.29
$MoSe_2$	3.309	13.323	0.624	3.289	12.927	0.621	0.959	1.09
WS_2	3.183	13.131	0.630	3.150	12.320	0.622	1.283	1.35
WSe_2	3.319	13.729	0.627	3.282	12.960	0.621	1.188	1.20

Table 3.1: Calculated properties of bulk TMDC materials: lattice constant a_0, c-axis lattice constant c_0, z-parameter z, and bandgap $E_g(eV)$. Experimental values [3–5] have been included for comparison.

Structure	Point	MoS$_2$	MoSe$_2$	WS$_2$	WSe$_2$	MoS$_2$	MoSe$_2$	WS$_2$	WSe$_2$
		Hole Effective Mass (m$_0$)				**Electron Effective Mass (m$_0$)**			
1L	K$_l$	0.543	0.578	0.339	0.341	0.506	0.502	0.349	0.345
	K$_t$	0.546	0.588	0.339	0.348	0.504	0.503	0.347	0.345
2L	Γ	1.039	1.430	1.239	1.322	-	-	-	-
	K$_l$	0.548	0.595	0.345	0.349	0.521	0.539	0.359	0.411
	K$_t$	0.546	0.596	0.346	0.348	0.510	0.539	0.359	0.412
3L	Γ	1.239	1.432	1.246	1.382	-	-	-	-
	K$_t$	0.549	0.602	0.366	0.368	0.559	0.544	0.376	0.434
	K$_t$	0.548	0.604	0.366	0.368	0.559	0.544	0.377	0.434
4L	Γ	1.239	1.433	1.351	1.432	-	-	-	-
	K$_l$	0.548	0.604	0.366	0.367	0.554	0.542	0.376	0.435
	K$_t$	0.546	0.604	0.366	0.368	0.559	0.549	0.377	0.434
Bulk	Γ	0.838	0.973	0.832	0.997	-	-	-	-
	Σ_l	-	-	-	-	0.590	0.521	0.569	0.489
	Σ_t	-	-	-	-	0.845	0.776	0.665	0.643

Table 3.2: *Ab-initio* calculations of the hole and electron effective masses at the valence band maxima and conduction band minima respectively for each structure in units of the free electron mass (m$_0$). The subscripts l and t refer to the masses calculated at the symmetry point along the longitudinal and the transverse directions.

structure calculations at the high symmetry points are summarized in Tables 3.2 and

Table 3.3.   Table 3.2 gives the relative effective masses, and Table 3.3 gives the

energy gaps.

A number of prior theoretical studies of the electronic structure of monolayer and

few-layer TMDCs did not include spin-orbit interaction. [95–97] As a result, the band

bandgaps reported in those studies are slightly larger. For example the bandgaps

reported in a prior PBE level calculation [95] are greater by 70 meV, 260 meV and

and 284 meV for MoS$_2$ and MoSe$_2$, WS$_2$ and WSe$_2$ respectively when compared to

our calculation results. Without the inclusion of spin-orbit interaction, our values

for the bandgap of the monolayer TMDCs are consistent with the bandgaps reported

Structure	Transition	MoS$_2$	MoSe$_2$	WS$_2$	WSe$_2$	MoS$_2$	MoSe$_2$	WS$_2$	WSe$_2$
		Calculated (eV)				Experimental (eV)			
1L	Γ_v to K_c	1.705	1.768	1.849	1.776	-	-	-	-
	Γ_v to Σ_c	1.922	1.862	1.929	1.806	-	-	-	-
	K_{v1} to K_c	**1.600**	**1.375**	**1.573**	**1.254**	1.900	1.660	1.950	1.640
	K_{v2} to K_c	1.750	1.556	1.973	1.715	2.050	1.850	2.360	2.040
2L	Γ_v to K_c	**1.564**	**1.368**	**1.507**	1.586	1.600	-	1.730	-
	Γ_v to Σ_c	1.775	1.373	1.542	1.562	-	-	-	-
	K_{v1} to K_c	1.600	1.373	1.549	1.269	1.880	-	1.910	1.590
	K_{v2} to K_c	1.760	1.556	1.977	1.788	2.050	-	2.340	2.000
3L	Γ_v to K_c	**1.150**	**1.334**	**1.458**	1.586	-	-	-	-
	Γ_v to Σ_c	1.171	1.372	1.482	1.508	-	-	-	-
	K_{v1} to K_c	1.620	1.376	1.485	1.265	-	-	-	-
	K_{v2} to K_c	1.780	1.564	1.873	1.783	-	-	-	-
4L	Γ_v to K_c	**1.120**	**1.351**	**1.438**	1.546	-	-	-	-
	Γ_v to Σ_c	1.139	1.374	1.439	1.434	-	-	-	-
	K_{v1} to K_c	1.630	1.356	1.459	1.259	-	-	-	-
	K_{v2} to K_c	1.780	1.574	1.877	1.753	-	-	-	-
Bulk	Γ_v to Σ_c	**1.060**	**0.959**	**1.283**	**1.188**	1.290	1.090	1.350	1.200
	K_{v1} to K_c	1.590	1.349	1.453	1.258	1.880	1.350	1.880	1.580
	K_{v2} to K_c	1.780	1.588	1.889	1.737	2.060	1.380	2.320	1.950

Table 3.3: *Ab-initio* calculations of the bandgap energies and energy transitions between the valence (v) and conduction (c) band valleys for each structure and material. The splitting of the valence band at the K-point due to spin-orbit coupling and the inter-layer interactions are denoted as K_{v1} and K_{v2}. Σ is the mid-point between Γ and K. The bandgap at each dimension is highlighted in bold text. Experimental values when available [3–6] have been included for comparison.

in these studies. Including spin-orbit coupling results in a splitting of the valence bands, Δ_{SO}, at K. The spin orbit interaction shifts up one of the degenerate valence bands, and this reduces the bandgap. The degree of the energy shift ranges from 39.6 meV for MoS_2 to 210.9 meV for WS_2. The second degenerate valence band is shifted down by an energy that is also unique to each TMDC material; this ranges from 110.4 meV for MoS_2 to 316.2 meV for WSe_2. For example the calculated Δ_{SO} energies of the monolayer TMDCs are 150 meV, 181 meV, 425 meV and 461 meV for MoS_2, $MoSe_2$, WS_2 and WSe_2, respectively. This is in good agreement with a prior PBE level calculation [98] that accounted for spin-orbit interaction which obtained Δ_{SO} values of 146 meV, 183 meV, 425 meV and 461 meV for MoS_2, $MoSe_2$, WS_2 and WSe_2, respectively, and a Δ_{SO} energy of 188 meV obtained for monolayer MoS_2 with the use of optical absorption experiments. [39]

More sophisticated many-body *ab-initio* calculations which include HSE or GW calculations have been reported in prior studies of the band structure of monolayer [98–101] and bilayer [99, 101] structures of the molybdenum and tungsten dichalcogenides. The values for Δ_{SO} resulting from these theories are only slightly changed from those of the PBE model. The Δ_{SO} values reported for monolayer MoS_2, $MoSe_2$, WS_2 and WSe_2 with a GW (HSE) calculation are 164 (193) meV, 212 (261) meV, 456 (521) meV and 501 (586) meV. [98] The primary difference between the PBE and the HSE and GW calculations is an increase in the bandgap. However, the PBE bandgap is large enough compared to the temperatures considered that the exact magnitude of the bandgap has no effect on the thermoelectric parameters. An explicit comparison of the electronic structure and the thermoelectric parameters calculated from the PBE and the HSE functionals for 1L - 4L MoS_2 is given below.

Calculation of the thermoelectric parameters requires the density of modes extracted from the electronic bandstructure using Eq. (5.7). Figure 3.2 shows the
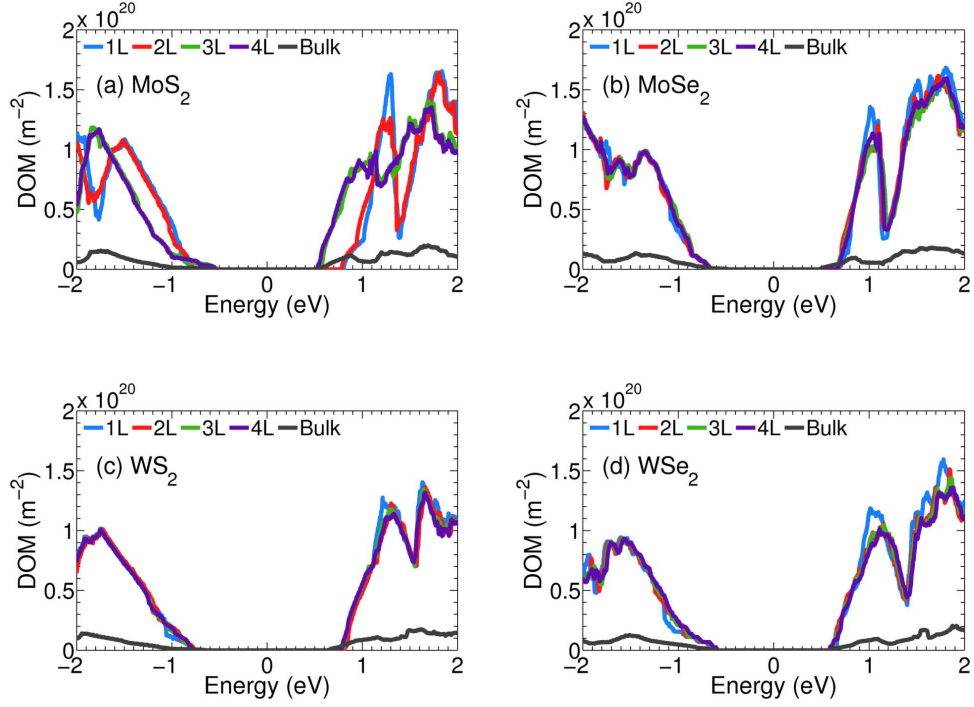
Figure 3.2: (Color online) Distribution of modes per unit area versus energy for (a) MoS_2, (b) $MoSe_2$, (c) WS_2 and (d) WSe_2 for bulk (black), 1L (blue), 2L (red), 3L (green) and 4L (purple) structures. The midgap energy is set to E=0.

density of modes versus energy for bulk, 1L, 2L, 3L, and 4L MoS_2, $MoSe_2$, WS_2, and WSe_2. To compare the density of modes of the bulk structure with the thin-film structures, we divide the density of modes of the thin-film structures by their respective thickness, t. As will be shown, for these TMDCs, small variations in the shape of the density of modes near the band edges can enhance the power factor and subsequently ZT. The thermoelectric properties of the bulk and thin-film structures are calculated from Eqs. (5.1) - (3.6) using the density of modes shown in Fig. 3.2.

The Seebeck coefficient, electrical conductivity, power-factor (PF), and the thermoelectric figure-of-merit (ZT) as a function of the reduced Fermi level, η_F are shown in Figures 3.3, 3.4, 3.5, and 3.6, respectively.

The reduced Fermi-level is $\eta_F = \frac{E_F - E_{C1}}{kT}$ for electrons in the conduction band,

28
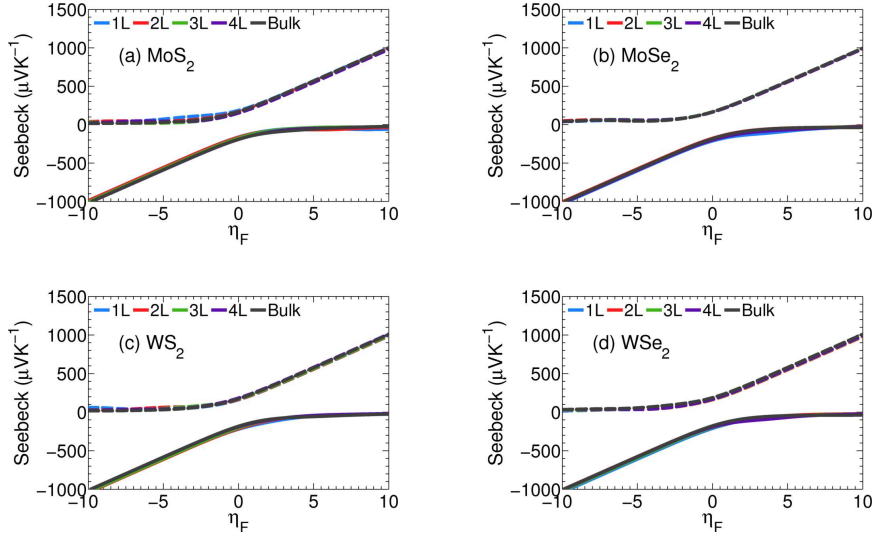
Figure 3.3: (Color online) Seebeck coefficient at 300K for (a) MoS$_2$, (b) MoSe$_2$, (c) WS$_2$ and (d) WSe$_2$ for bulk (black), 1L (blue), 2L (red), 3L (green) and 4L (purple) structures. The n-type Seebeck coefficients are plotted with a solid line and p-type coefficients with a broken line as a function of the reduced Fermi energy, η_F.
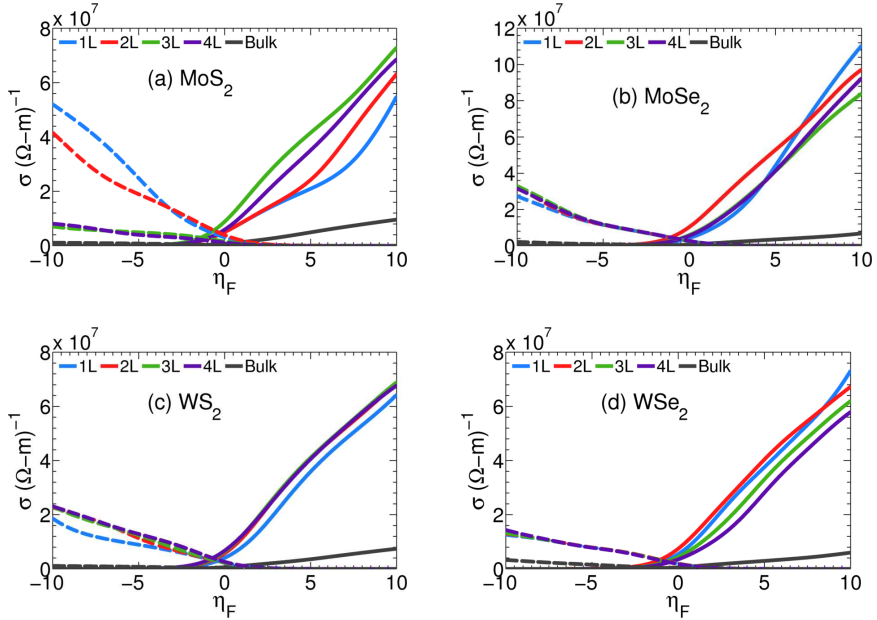
Figure 3.4: (Color online) Electrical conductivity, σ, at 300K for (a) MoS$_2$, (b) MoSe$_2$, (c) WS$_2$ and (d) WSe$_2$ for 1L (blue), 2L (red), 3L (green) and 4L (purple) and bulk (black) structures. The n-type electrical conductivity is plotted with a solid line and p-type conductivity with a broken line as a function of the reduced Fermi energy, η_F.
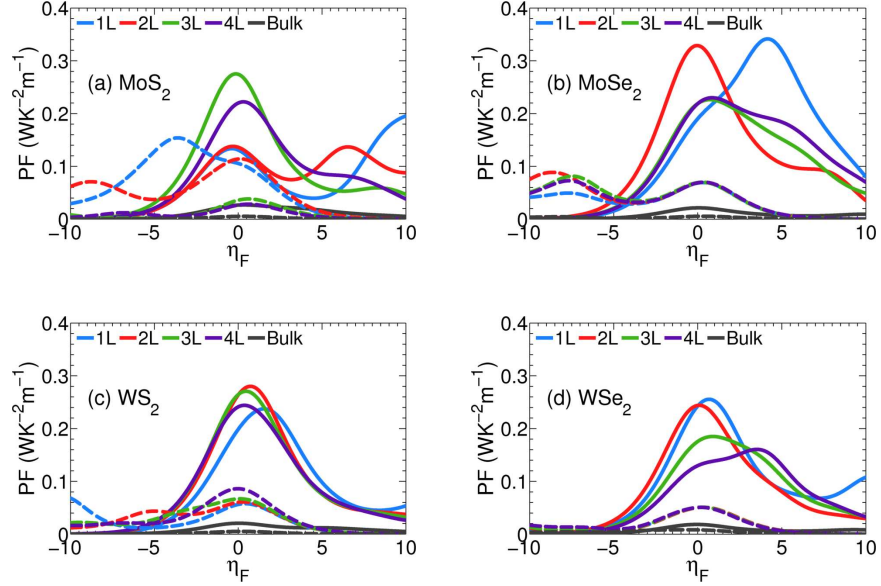
Figure 3.5: (Color online) Power factor (PF) at 300K for (a) MoS_2, (b) $MoSe_2$, (c) WS_2 and (d) WSe_2 for bulk (black), 1L (blue), 2L (red), 3L (green) and 4L (purple) structures. The n-type power factors are plotted with a solid line and p-type PFs with a broken line as a function of the reduced Fermi energy, η_F.
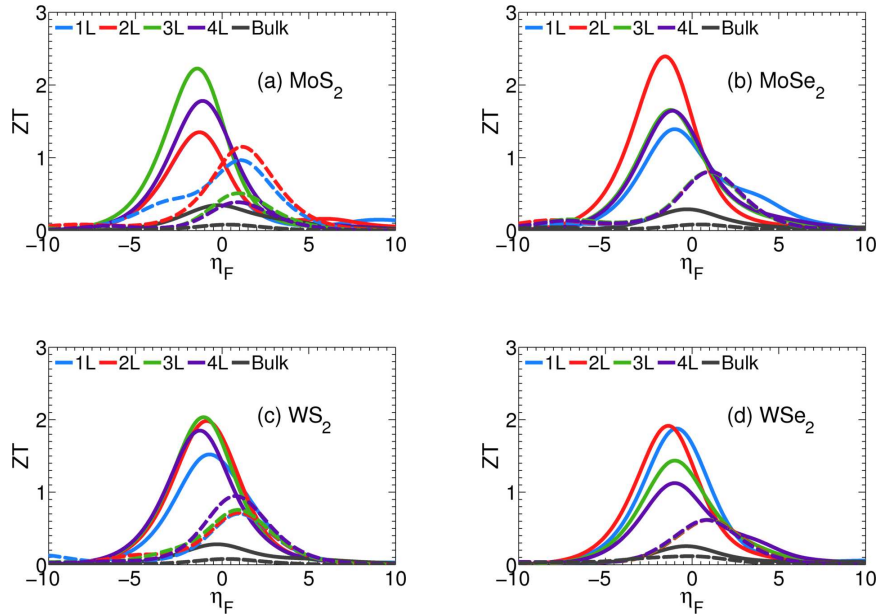
Figure 3.6: (Color online) ZT at 300K for (a) MoS_2, (b) $MoSe_2$, (c) WS_2 and (d) WSe_2 for bulk (black), 1L (blue), 2L (red), 3L (green) and 4L (purple) structures. The n-type ZT is plotted with a solid line and p-type ZT with a broken line as a function of the reduced Fermi energy, η_F.

	Temperature	1L	2L	3L	4L	Bulk
		Maximum n-type (p-type) Power Factor ($WK^{-2}m^{-2}$)				
MoS_2	300K	.130 (.150)	.140 (.110)	**.280** (.041)	.220 (.031)	.0320 (.010)
	150K	.093 (.072)	.093 (.071)	**.190** (.032)	.120 (.024)	.012 (.0042)
	77K	.072 (.043)	.072 (.053)	**.13** (.021)	.063 (.022)	.012 (.0031)
$MoSe_2$	300K	**.340** (.071)	.330 (.094)	.230 (.082)	.230 (.071)	.022 (.0061)
	150K	**.151** (.050)	.200 (.051)	.100 (.051)	.100 (.052)	.013 (.004)
	77K	**.062** (.031)	.120 (.032)	.062 (.031)	.052 (.032)	.013 (.0032)
WS_2	300K	.240 (.062)	**.280** (.061)	.270 (.071)	.240 (.092)	.022 (.0052)
	150K	.110 (.042)	**.160** (.042)	.150 (.041)	.130 (.051)	.010 (.0043)
	77K	.051 (.031)	**.081** (.032)	.070 (.032)	.081 (.031)	.010 (.0022)
WSe_2	300K	**.260** (.054)	.240 (.052)	.190 (.053)	.160 (.053)	.022 (.014)
	150K	**.141** (.030)	.140 (.031)	.081 (.031)	.070 (.031)	.010 (.004)
	77K	.071 (.031)	**.082** (.031)	.050 (.031)	.043 (.022)	.011 (0.0021)

Table 3.4: Peak n-type (p-type) power factor of 1L, 2L, 3L, 4L and bulk MoS_2, $MoSe_2$, WS_2 and WSe_2 at 300K, 150K and 77K. The maximum power factor for each material at a given temperature is in bold.

and $\eta_F = \frac{E_F - E_{V1}}{kT}$ for holes in the valence band. E_{C1} and E_{V1} are the energies of the conduction and valence band edges, respectively. For each material and each thickness the maximum power factor and ZT occurs for the conduction band states. The peak conduction band and valence band power factor and ZT for each structure and material at 77K, 150K and 300K are summarized in Table 3.4 and Table 3.5, respectively.

For all materials, the few layer structures show a large increase in the values of their power factor and ZT compared to those of the bulk.

The peak n-type ZT values (and corresponding layer thicknesses) for MoS_2, $MoSe_2$, WS_2 and WSe_2 are 2.23 (t=3L), 2.39 (t=2L), 2.03 (t=3L) and 1.91 (t=2L) which is an improvement by a factor of 6.4, 8.2, 7.2 and 7.5 over the respective bulk values. These peak ZT values occur when the Fermi level is moved by 1.39kT, 1.55kT, 1.08kT

31

	Temperature	1L	2L	3L	4L	Bulk
			Maximum n-type (p-type) ZT			
MoS_2	300K	1.35 (.970)	1.35 (1.15)	**2.23** (.510)	1.78 (.390)	.350 (.081)
	150K	.590 (.350)	.590 (.450)	**1.03** (.220)	.660 (.160)	.110 (.034)
	77K	.240 (.140)	.240 (.190)	**.420** (.093)	.210 (.062)	.031 (.012)
$MoSe_2$	300K	1.39 (.800)	**2.39** (.810)	1.66 (.810)	1.65 (.810)	.290 (.081)
	150K	.450 (.310)	**1.06** (.320)	.610 (.320)	.570 (.320)	.100 (.033)
	77K	.130 (.120)	**.410** (.120)	.220 (.120)	.170 (.120)	.030 (.014)
WS_2	300K	1.52 (.70)	1.98 (.720)	**2.03** (.760)	1.85 (.760)	.280 (.082)
	150K	.411 (.280)	.613 (.280)	**.770** (.280)	.721 (.350)	.104 (.030)
	77K	.120 (.110)	.181 (.113)	.211 (.113)	**.271** (.113)	.034 (.012)
WSe_2	300K	1.88 (.620)	**1.92** (.620)	1.44 (.620)	1.13 (.620)	.260 (.120)
	150K	.590 (.220)	**.750** (.220)	.490 (.220)	.380 (.220)	.091 (.032)
	77K	.180 (.100)	**.270** (.100)	.170 (.100)	.130 (.100)	.031 (.014)

Table 3.5: Peak n-type (p-type) thermoelectric figure of merit, ZT, of 1L, 2L, 3L, 4L and bulk MoS_2, $MoSe_2$, WS_2 and WSe_2 at 300K, 150K and 77K. The maximum ZT for each material at a given temperature is in bold.

and 1.39kT, respectively, below the conduction band at T=300K. This corresponds to electron carrier densities of 6.26×10^{19} cm^{-3}, 5.74×10^{19} cm^{-3}, 5.34×10^{19} cm^{-3} and 4.72×10^{19} cm^{-3} for MoS_2, $MoSe_2$, WS_2 and WSe_2 respectively. The peak p-type ZT values (and corresponding layer thicknesses) for MoS_2, $MoSe_2$, WS_2 and WSe_2 are 1.15 (t=2L), 0.81 (t=2L-4L), 0.76 (t=2L-3L) and 0.62 (t=1L-4L) which is an improvement by a factor of 14.4, 10.1, 9.5 and 5.2 over the respective bulk values. These peak ZT values occur when the Fermi level is moved by 1.16kT, 1.01kT, 0.93kT and 0.85kT, respectively, above the valence band at T=300K. This corresponds to hole carrier densities of 7.12×10^{19} cm^{-3}, 5.84×10^{19} cm^{-3}, 4.02×10^{19} cm^{-3} and 3.91×10^{19} cm^{-3} for MoS_2, $MoSe_2$, WS_2 and WSe_2 respectively. Of the four TMDC materials studied, MoS_2 is the only material to exhibit a p-type and n-type ZT > 1. In contrast to Bi_2Te_3, the peak value of ZT does not occur in any of the materials at

a monolayer thickness.

The Seebeck coefficients at the maximum n-type (p-type) ZT for each material are 275 (245.6) μVK^{-1}, 287 (230.7) μVK^{-1}, 279 (230.1) μVK^{-1} and 276 (216.7) μVK^{-1} for MoS_2, $MoSe_2$, WS_2 and WSe_2 respectively. However, the Seebeck coefficients at the maximum n-type (p-type) power factor for each material are 167 (90.4) μVK^{-1}, 100 (185.8) μVK^{-1}, 165 (177.1) μVK^{-1} and 171 (172.1) μVK^{-1} for MoS_2, $MoSe_2$, WS_2 and WSe_2, respectively. This is generally consistent with the conclusion of a report on engineering the Seebeck coefficient to obtain the maximum thermoelectric power factor. [102]

Without the inclusion of spin-orbit interaction our values of the ballistic ZT for the monolayer TMDC materials are consistent with a prior report on the monolayer thermoelectric properties of these TMDC materials. [76] Our calculations show that without the inclusion of spin-orbit interaction the peak n-type ZT values for all materials continue to occur at thicknesses above a single monolayer. The peak n-type ZT values (and corresponding layer thicknesses) without spin-orbit interaction for MoS_2, $MoSe_2$, WS_2 and WSe_2 are 1.38 (t=3L), 1.52 (t=2L), 1.13 (t=4L) and 1.28 (t=2L). However, the peak p-type ZT values without spin-orbit interaction occurs for a single monolayer for each TMDC material. The p-type ZT values without spin-orbit interaction for MoS_2, $MoSe_2$, WS_2 and WSe_2 are 1.42, 0.84, 0.90 and 0.69.

Recent electronic structure calculations using the Heyd-Scuseria-Ernzerhof (HSE) hybrid functional [101] give a bandgap that more accurately matches known experimental values. [101] To assess whether the trends in the thermoelectric parameters predicted with the PBE functional are the same as those resulting from the HSE functional, we calculate the electronic band structure of 1L, 2L, 3L and 4L MoS_2 with both the PBE and the HSE functional and plot the results in Fig. 3.7. Near the band edges, the HSE energies appear to be shifted with respect to the PBE energies.
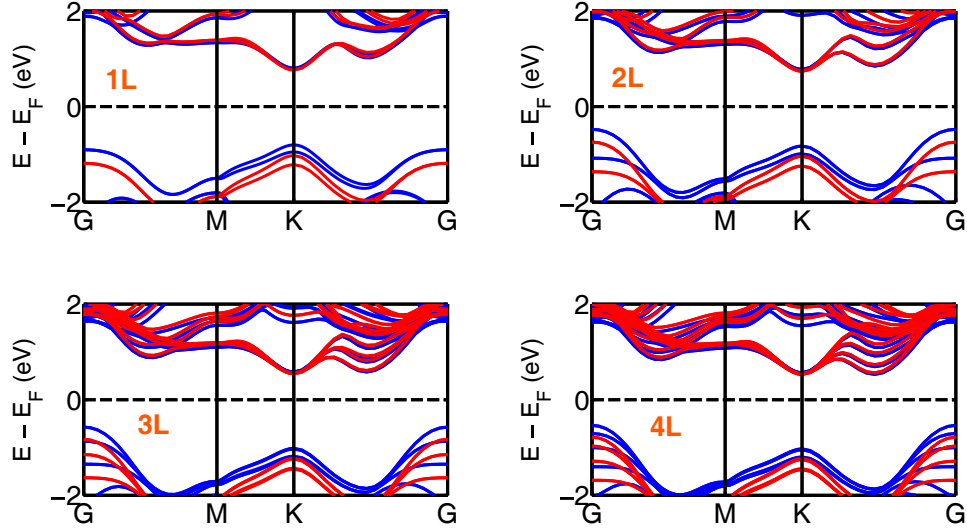
Figure 3.7: *Ab-initio* calculated electronic structure of MoS$_2$: 1L, 2L, 3L and 4L structures using a PBE (blue) and hybrid HSE (red) functional. The HSE functional provides a correction to the underestimated PBE bandgap while the salient features of the electronic structure that would affect the density-of-modes calculation remain the same.

The effective masses for the HSE band structures are lower by up to 17% for the conduction band valleys at K and Σ and are lower by up to 11% for the valence band valleys at K and Γ.

To verify that the HSE functional leaves the thermoelectric trends predicted from the PBE functional unchanged, we compute the density-of-modes and thermoelectric performance of 1L, 2L and 3L MoS$_2$ using the HSE functional with the inclusion of spin orbit coupling. Figure 3.8 illustrates the DOM, Seebeck coefficient, power factor and ZT for the 1L, 2L and 3L structures of MoS$_2$ computed with the HSE functional.

The quantitative values do differ. For the MoS$_2$ trilayer structure, the HSE (PBE) functionals give a peak n-type power factor of 0.41 (0.28) WK^{-2}m^{-2} and a peak n-type ZT of 2.4 (2.2). However, the HSE results for few-layer MoS$_2$ structures demonstrate the same trends in the shape of the density of modes and the same trends in the
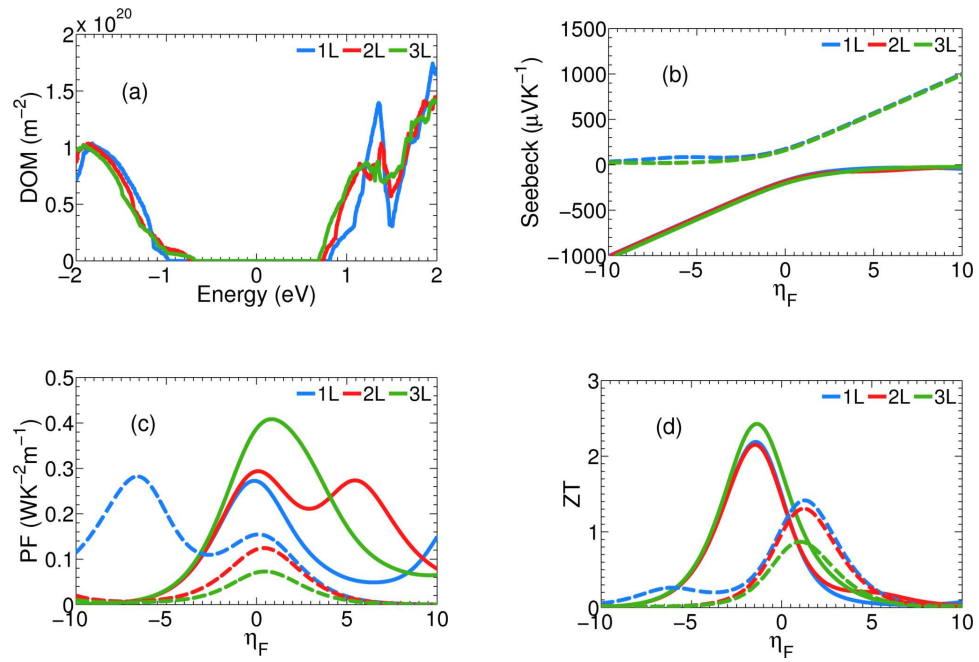
Figure 3.8: (Color online) HSE calculation of the (a) density-of-modes, (b) Seebeck coefficient, (c) Power factor and (d) ZT 1L (blue), 2L (red), 3L (green) MoS_2. The n-type thermoelectric parameters are plotted with a solid line and the p-type parameters are plotted with a broken line as a function of the reduced Fermi energy, η_F.
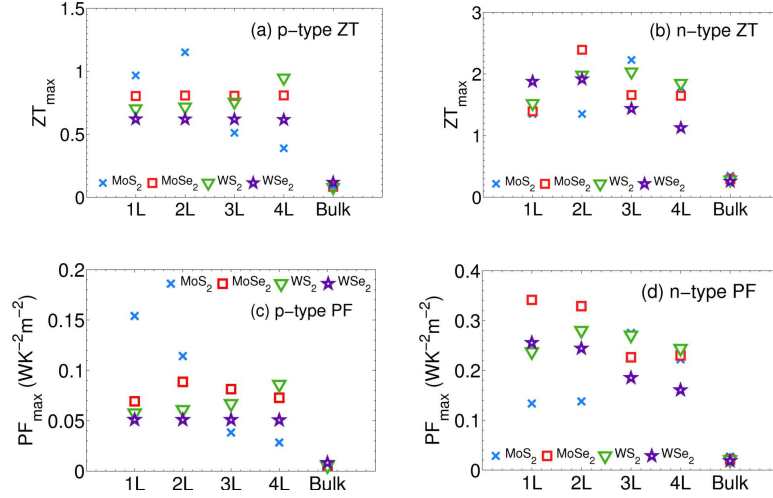
Figure 3.9: (Color online) Maximum thermoelectric performance for 1L (blue), 2L (red), 3L (green), 4L (purple) and bulk (black) MoS_2, $MoSe_2$, WS_2, WSe_2 at 300K: (a) Maximum p-type ZT, (b) Maximum n-type ZT, (c) Maximum p-type power factor, (d) Maximum n-type power factor.

values for the power factors and ZT. Both the HSE and PBE calculations show that the turn-on of the density of modes is sharpest for the tri-layer structure resulting in maximum values for the power factor and ZT. Since the primary effect on the low energy states of the exact exchange in the HSE functional is to shift the band edges with respect to those of a PBE calculation, the trends resulting from the shape of the density of modes should be preserved.

Figure 3.9 summarizes the values from the PBE calculations for the peak n-type and p-type ZT and power factors for each TMDC material and layer thickness.

In the n-type $MoSe_2$, WS_2 and WSe_2 structures, the peak power-factor and the peak ZT do not occur at the same film thickness. For example, in $MoSe_2$, a single monolayer has the highest power factor, and a bilayer has the highest ZT. This can be explained by the increase in the electronic thermal conductivity, κ_e as the Fermi level is moved into the conduction band.

Figure 3.10 shows the ratio of the total thermal conductivity, κ_{tot}, with respect
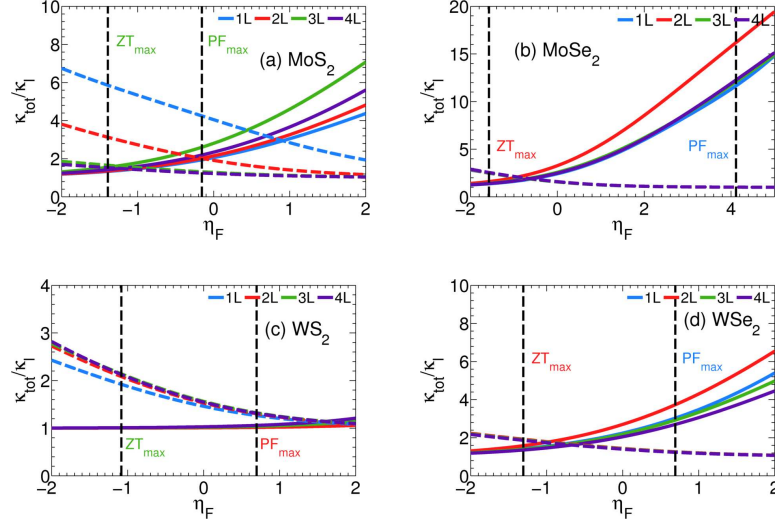
Figure 3.10: (Color online) Ratio of total thermal conductivity ($\kappa_l + \kappa_e$) over the lattice thermal conductivity (κ_l) at 300K for (a) MoS_2, (b) $MoSe_2$, (c) WS_2, (d) WSe_2 for 1L (blue), 2L (red), 3L (green) and 4L (purple) structures. The n-type ratio is plotted with a solid line and p-type ratio with a broken line as a function of the reduced Fermi energy, η_F. The two vertical dashed lines show the reduced Fermi level position at which the maximum n-type power factor and ZT occur.

to the lattice thermal conductivity, κ_l, for each TMDC material.

The two guide lines on each figure illustrate the reduced Fermi level position at which the maximum n-type power factor and ZT occurs. The ratio $\kappa_{\text{tot}}/\kappa_l = 1 + \kappa_e/\kappa_l$ is higher at the Fermi level position where the the maximum power factor occurs. This increase in κ_e explains why the peak power factor and ZT occur at different Fermi energies and film thicknesses.

A number of recent studies report on the theoretical [103, 104] and experimental values [105, 106] of the lattice thermal conductivity on monolayer and few-layer TMDC materials with values of κ_l ranging from 19 $Wm^{-1}K^{-1}$ to 83 $Wm^{-1}K^{-1}$. Experimental measurements of the in-plane κ_l in suspended samples of MoS_2 [106] find a value of 34.5 $Wm^{-1}K^{-1}$ for 1L MoS_2 and 52 $Wm^{-1}K^{-1}$ for few-layer MoS_2. To assess whether the inequivalent κ_l values for the monolayer and few-layer TMDC films
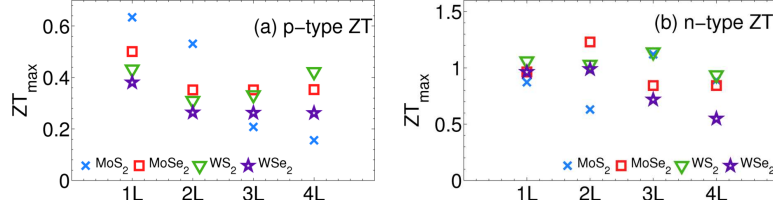
Figure 3.11: (Color online) Maximum ZT for (a) p-type and (b) n-type of MoS_2, $MoSe_2$, WS_2, WSe_2 at 300K for 1L (blue), 2L (red), 3L (green), 4L (purple) structures accounting for thickness-dependent lattice thermal conductivity. $\kappa_l = 34.5$ $Wm^{-1}K^{-1}$ used for the 1L structures and $\kappa_l = 52$ $Wm^{-1}K^{-1}$ used for the few-layer structures.

leave the predicted thermoelectric trends unchanged, we computed the thermoelectric parameters using $\kappa_l = 34.5$ $Wm^{-1}K^{-1}$ for the monolayer and $\kappa_l = 52$ $Wm^{-1}K^{-1}$ for the few-layer TMDC films of each material. The values of ZT differ compared to using $\kappa_l = 19$ $Wm^{-1}K^{-1}$ for each film thickness. For MoS_2, the room temperature n-type ZT values using the thickness dependent (constant) κ_l for the 1L, 2L, 3L and 4L structures are 0.87 (1.35), 0.63 (1.15), 1.11 (2.23), 0.89 (1.78). The maximum n-type ZT still occurs for the 3L structure and the minimum n-type ZT still occurs for the 1L structure. The trends for all of the n-type materials are preserved when a thickness dependent thermal conductivity is used. All of the values are shown in Fig. 3.11(b). For the n-type materials, changes in the density of modes are the dominant factor determining the trends. For p-type $MoSe_2$, WS_2, WSe_2, ZT varies little for different layer thicknesses when using a constant κ_l as shown in Fig. 3.9(a). For p-type MoS_2, the difference between the maximum ZT of a bilayer and the second highest value of a monolayer is small. Therefore, reducing the value of κ_l for a monolayer from 52 to 35.4 $WM^{-1}K^{-1}$ is sufficient to cause the peak value of ZT to occur at monolayer thickness for all 4 p-type materials as shown in Fig. 3.11(a).

In an attempt to study the transition of the thermoelectric performance from few-layer films to bulk like performance, we calculate the thermoelectric parameters for an 8L film of WS_2. Figure 3.12 illustrates the density of modes and the ZT for bulk,
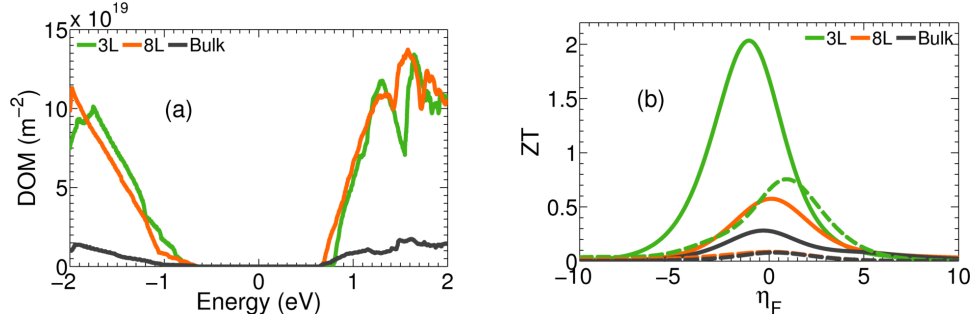
Figure 3.12: (Color online) (a) Density of modes and (b) ZT as a function of the reduced Fermi level for 3L (green), 8L (orange) and bulk (bulk) WS$_2$.

3L and 8L WS$_2$. The n-type 0.974 ZT value of the 8L film is a factor of 1.9 smaller than that of the 4L film, but it is still a factor of 3.5 larger than that of the bulk. The p-type 0.163 ZT value of the 8L film is a factor of 4.7 smaller than that of the 4L film, and it is a factor of 2.0 larger that that of the bulk. Even at 8 monolayers, there is still an enhancement of the ZT value compared to that of the bulk, and the enhancement is larger in the n-type material.

The thermoelectric performance in the low dimensional structures is enhanced by the more abrupt step-like shape of the density of modes distribution. [87] It is clear from Eq. (5.4), that with $E_F \leq 0$, a step-function density of modes removes all negative contributions to the integrand of I_1 giving a maximum value for I_1. The conduction band DOM distribution for the maximum and minimum ZT structures for each material are plotted in Figure 3.13.

In all cases, the DOM with the sharper turn-on at the band edge gives rise the the maximum value for ZT.
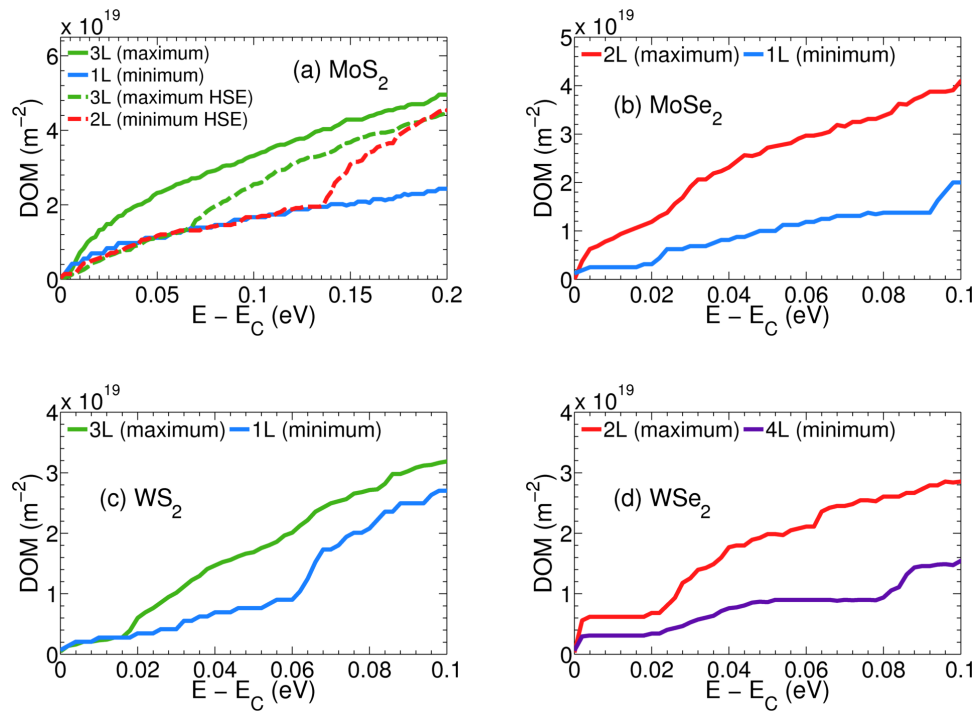
Figure 3.13: (Color online) Conduction band density of modes (DOM) for (a) MoS$_2$, (b) MoSe$_2$, (c) WS$_2$ and (d) WSe$_2$ at film thicknesses where the maximum and the minimum ZT occurs with respect to the energy away from the conduction band edge, E$_C$.

3.4 Discussion

The enhancement in the thermoelectric performance of *few* monolayer TMDC materials is in contrast to the enhanced thermoelectric performance observed for only a single quintuple (QL) layer of p-type Bi_2Te_3. Above 1 QL of Bi_2Te_3, the thermoelectric figure of merit approaches the bulk ZT. [45, 70]. The enhancement of ZT in n-type monolayer Bi_2Te_3 is minimal. This difference in the effect of layer thickness on ZT in the two different classes of materials can be explained by differences in the effect of thickness on the band-edge degeneracy and the density of modes. The valence band of monolayer Bi_2Te_3 is a ring in k-space that covers much of the Brillouin zone as shown in Fig. 4(d) of Ref. [45]. Thus, the integration over $k_\perp$ in Eq. (5.7) jumps from zero in the band gap to a finite number at the band edge resulting in a step-function turn-on of the valence band density of modes as seen in Fig. 3 of Ref. [70] and Fig. 2 of Ref. [45]. The size of the ring in k-space quickly collapses for thicknesses above a monolayer, and the large enhancement in ZT dissappears. In a parabolic band, the band edge is a point in k-space, and, in two-dimensions, the density of modes turns on smoothly as $\sqrt{E}$. [87] The band edge of n-type monolayer Bi_2Te_3 remains parabolic resulting in a smooth turn-on of the density-of-modes and no significant enhancement of ZT.

The bands of the TMDC materials also remain parabolic at the band edges, however the conduction bands at the K_c and the Σ_c valleys become nearly degenerate for few monolayer thicknesses as shown in Fig. 3.1. Since the Σ_c valley is 6-fold degenerate, and the K_c valley is 3-fold degenerate, this results in a near 9-fold degeneracy of the conduction band edge. This increases the density of modes in the conduction band by a factor of 9 from that of a single valley. Furthermore, with increasing film thickness from 1L to 4L, the splitting of the Σ_c bands resulting from interlayer cou-

pling is on the order of $k_B T$. In MoS$_2$, the splitting at Σ_C is 0.4 meV for the 2L and 40 meV for the 4L structure. The other materials show similar magnitudes of the energy splitting as a function of thickness. Therefore, the near-degeneracy of the bands at Σ_c increases linearly with the film thickness, so that the number of modes per layer becomes relatively insensitive to the layer thickness for few monolayer thicknesses.

The interlayer coupling of the out-of-plane d$_{z^2}$ and p$_z$ orbitals result in the strongest interlayer hybridization and energy level splitting. [107] In MoS$_2$ the orbital composition of the conduction band Σ_c valley is 36% d$_{z^2}$, 22% d$_{xy}$, 23% d$_{x^2-y^2}$, 6% p$_z$, and 5% p$_x$ and p$_y$. The d-orbital composition of the K_c valley is 67% d$_{z^2}$. With increasing layer number, the K_c valley splitting is larger than $k_B T$ so that the number of modes contributed by the K_c valleys remains 3 independent of layer number. Thus, when the Σ_c valley falls within $k_B T$ of the K_c valley, its contribution to the density of modes dominates for few-layer thicknesses. Beyond 4 layers, the total splitting becomes larger than $2k_B T$, and the number of accessible modes at Σ_c no longer increases linearly with thickness.

Beyond a monolayer, the valence band shifts to Γ_v for MoS$_2$, MoSe$_2$ and WS$_2$. The energy difference between Γ_v and K_v varies as a function of the film thickness and material. For MoS$_2$ the energy difference between Γ_v and K_v increases from 35 meV for the bilayer to 470 meV and 510 meV for the 3L and 4L structures respectively. The near degeneracy of the Γ_v and K_v valleys leads to the largest p-type density of modes for 2L MoS$_2$. For MoSe$_2$, the Γ_v and K_v valleys are nearly degenerate above a single monolayer. In WS$_2$, the energy difference of the Γ_v and K_v valleys decreases from 42 meV to 21 meV as the film thickness is increased from a bilayer to four layers. For WSe$_2$, the valence band maxima continues to reside at K_v beyond a monolayer. Once the valence band K_v valleys begin to contribute in MoSe$_2$, WS$_2$, and WSe$_2$, the density of modes per layer becomes relatively independent of layer thickness, since

there is little splitting of the K_v valleys due to the interlayer coupling. [107] The K_v valley orbital composition contains no d$_{z^2}$ or p_z components. In MoS$_2$, the splitting varies from 0.2 meV for the 2L structure to 7.6 meV for the 4L structure. The other materials show similar magnitudes of the energy splitting as a function of thickness. Thus, at room temperature, the number of contributed modes per layer within k_BT of the K_v valley minimum remains constant for thicknesses in the range of one to four monolayers.

For the 8 layer WS$_2$ structure, the conduction band K_c and Σ_c valleys are still nearly degenerate. The K_c valley lies 21 meV above the Σ_c valley. However, at both valleys, the total splitting of the 8 bands contributed from the 8 layers is much greater than k_BT at room temperature. At Σ_c, only two of the 8 bands are within 26 meV of the valley minimum. The overall energy splitting of the 8 bands at Σ_c is 193 meV. In the valence band, the K_v valley is 22 meV below the Γ_v valley. However, the 8 bands from the 8 monolayers are split over a total range of 180 meV, and the second band is 40 meV below the K_v valley maximum. Thus, as the number of layers increase, the total energy splitting of the bands contributed from each layer increases, and the number of modes per layer within k_BT of the valley minimums decreases.

As the number of layers becomes macroscopic such that the crystal is periodic in all three dimensions, the total splitting of the bands evolves into the width of the dispersive band along k_z for the bulk crystal. For bulk WS$_2$, the width of the band along the vertial k_z direction from Σ_c to R at the top of the Brillouin zone is 208 meV which is 15 meV larger than the total splitting of the 8 layer stack. Furthermore, in the bulk, the K_c valley is 126 meV above the Σ_c minimum, so the K_c contributes no modes to the density of modes near the conduction band edge. In the valence band, the K_v valley maximum is 225 meV below the Γ_v maximum, so that the density of modes near the valence band edge, is entirely from the Γ_v valley. The lack of valley

near-degeneracy and the width of the bulk dispersive bands along k_z, result in a minimum density of modes per layer near the band edges compared to those of few layer structures. The reduced number of modes per layer within $k_B T$ of the band edges results in reduced per-layer values of the thermoelectric figure of merit.

For both material systems Bi_2Te_3 and the semiconducting TMDCs, the enhancement of ZT results from the increased degeneracy or near-degeneracy of the band edges. The origin and nature of the degeneracy is different. In the Bi_2Te_3, the valence band edge becomes inverted into a ring as a result of the coupling of the topological surface states. In the TMDCs at few-layer thicknesses, different valleys become nearly degenerate. In the conduction band, the Σ_c valleys become nearly degenerate with the K_c valleys, and they contribute 6 more modes to the 3 modes from the K_c valleys. In the valence band, the K_v valleys become nearly degenerate with the Γ_v, and they contribute 3 more modes. Furthermore, because of the weak interlayer coupling at K_v and Σ_c, the additional bands from additional layers lie within $k_B T$ of the band edges for few layers. The increased band-edge degeneracy results in a sharper turn-on of the density of modes and an increased value of ZT.

3.5 Summary

The electronic structure of one to four monolayers of the semiconducting transition metal dichalcogenides MoS_2, $MoSe_2$, WS_2 WSe_2 are calculated using DFT with spin-orbit coupling and the PBE functional. Comparisons are made to results in the absence of spin-orbit coupling, and the PBE results are compared to HSE calculations for MoS_2. The peak n-type value of ZT increases by a factor of $6 - 8$ over the bulk value for all materials. Among the 4 materials and 4 thicknesses, bilayer $MoSe_2$ gives the maximum n-type ZT value of 2.4. The peak p-type value of ZT increases by a

factor of $5 - 14$ over the bulk value for all materials. The maximum p-type ZT value of 1.2 occurs for bilayer MoS_2. The maximum power factor generally occurs for a different layer thickness and at a more degenerate Fermi level than the maximum value of ZT. This difference can be explained by the increased electrical thermal conductivity at the Fermi level corresponding to the maximum power factor. For all materials, the maximum value of ZT coincides with the sharpest turn-on of the density of modes distribution at the band edge. The sharper turn-on is driven by the near valley degeneracy of the conduction band K_c and Σ_c valleys and the valence band Γ_v and K_v valleys. For few layer structures, the degeneracy is enhanced by the weak interlayer coupling at the Σ_c and K_v valleys.

Chapter 4

Electronic properties of misoriented transition metal dichalcogenides

4.1 Introduction

There is rapid progress fabricating electronic and optoelectronic devices with vertically stacked transition metal dichalcogenides (TMDCs). [108–110] The operation of these devices can rely on the alignment of the individual monolayers so that there is a preservation of inversion symmetry. [109] The fabrication of such devices often relies on mechanical stacking or the chemical growth of individual layers or few-layers of the TMDC materials. Such approaches are known to lead to interfaces that are turbostratically misoriented with respect to each other. [21, 111, 112] This motivates us to investigate the effect of crystal alignment and proximity on the electronic structure of perfectly registered and misoriented TMDC bilayers.

Prior experimental and theoretical studies of misorientation in graphene bilay-

ers demonstrated that a few degrees of misorientation are sufficient to decouple the low-energy electronic states of the individual layers. [113, 114] This is, in general, not true for TMDC bilayers. Rotated bilayers retain the qualitative electronic characteristics of a bilayer film rather than that of two independent monolayer films. While monolayers are direct gap, theoretical calculations showed that the bandgaps of bilayer MoS_2, $MoSe_2$, WS_2, and WSe_2 are indirect for all stacking orders. [115] When monolayers of MoS_2 are folded or rotated with respect to each other to form a bilayer, the bandgap becomes indirect with a value somewhat larger than that of an oriented bilayer. [116–119] AA stacked heterolayers of WS_2-WSe_2 and MoS_2-WSe_2 in which the chalcogen atoms are vertically aligned remained direct gap, [120] and heterolayers of MoS_2-$MoSe_2$ were shown to have a direct gap transition [107, 121] with the conduction band and valence band edges localized in different layers. Theoretical calculations demonstrated controlled decoupling of bilayer MoS_2 by bending. [122]. Experimentally, electronic decoupling of the TMDC monolayers has been achieved by inserting hexagonal boron nitride (h-BN) between the monolayers. [123, 124]

For bilayers of $MoSe_2$, WS_2 and WSe_2, the effect of rotation angle on the interlayer interaction has not yet been investigated. This work studies and compares the effect of misorientation on the electronic structure of bilayers of MoS_2, $MoSe_2$, WS_2 and WSe_2. Figure 4.1 shows a twisted MoS_2 bilayer, which is one of the structures studied in this work.

4.2   Methodology

Ab initio calculations of the bilayer and misoriented structures are carried out using density functional theory (DFT) with a projector augmented wave method [78] and the Perdew-Burke-Ernzerhof (PBE) type generalized gradient approximation [79, 80]
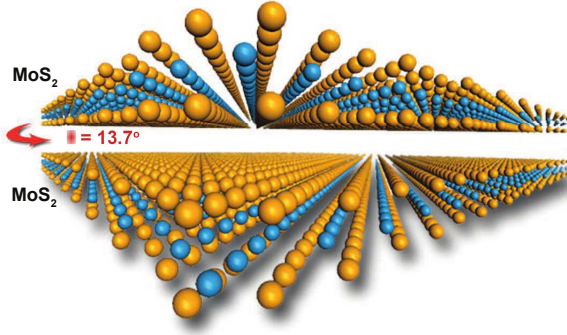
Figure 4.1: (Color online) (a) Atomic structure of rotated bilayer MoS_2.

as implemented in the Vienna *ab-initio* simulation package (VASP). [81, 82]

The lattice constants for the bilayer structure of each material are obtained from our prior calculations on the bulk structures of each material [1]. The registered bilayer structures rotated by 0° correspond to the 2H stacking order and the 60° structure corresponds 3R stacking order. The primitive unit cells of the misoriented structures rotated by $13.17°$, $21.78°$ and $27.79°$ are defined using an approach outlined in previous studies of misoriented bilayers of graphene. [125, 126] For the registered and rotated bilayer structures, 15Å of vacuum spacing was added in the perpendicular direction. Each rotated bilayer structure is optimized using the Grimme-D2 [83] and Tkatchenko-Scheffler [127] methods and the effect of each approach on the optimized geometry is compared. The atomic coordinates for all of the rotated bilayer structures were optimized in all directions until the interatomic forces are below 0.002 eV/Å. The Monkhorst-Pack scheme is used for the integration of the Brillouin zone with a k-mesh of 6 x 6 x 1 (12 x 12 x 1) for the rotated bilayer (registered bilayer) structures. The energy cutoff of the plane wave basis for the TMD structures is 400 eV. Spin orbit coupling is included self consistently in our calculations and the results are compared to calculations with no spin orbit interaction.
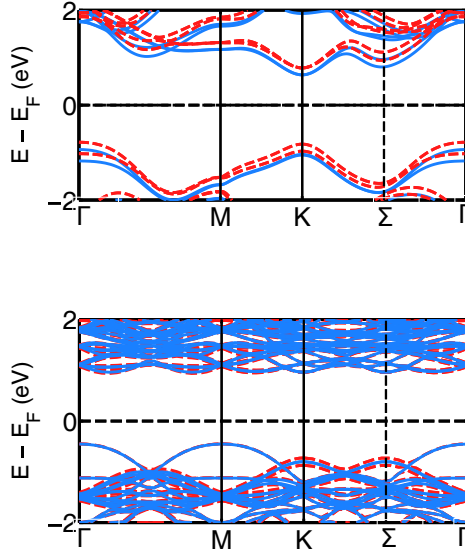
Figure 4.2: (Color online) (a) Electronic structure of (b) AA' stacked bilayer MoS_2 and (b) bilayer MoS_2 rotated at 21.78^o. Band structures are calculated with spin-orbit coupling (red - broken line) and without spin orbit coupling (blue - solid line).

4.3 Results

Figure 4.2 illustrates the atomic structure and the electronic structure of 2H bilayer MoS_2 and the bilayer MoS_2 supercell rotated at 21.78^o with and without SOC. The effect of SOC is most prominent in the splitting of the valence band at K_v for each unrotated and rotated bilayer structure. For MoS_2, the splitting, Δ_{SO} for $\theta=0°$, $21.78°$, $27.79°$ and $13.17°$ is 160 meV, 143 meV, 191.5 meV and 195 meV respectively. With and without SOC included in each calculation the valence band is Γ_v and the conduction band at K_c for the unrotated bilayer TMDCs. The trends resulting from misorientation angle predicted with or without the inclusion of SOC remain the same. Hence, unless otherwise noted, the reported results will be from the PBE functional without SOC.

The values of the energy transitions as a function of rotation angle for all four TMDCs are listed in Table 4.1, and the bandgap of each material as a function of

θ	d_{vdW}	Γ_v to K_c	K_v to K_c
	(Å)	(eV)	(eV)
MoS$_2$			
0 (2H)	3.11	1.259	1.659
13.17	3.42	1.481	1.674
21.78	3.38	1.455	1.667
27.79	3.40	1.459	1.674
60 (3R)	3.12	1.199	1.641
MoSe$_2$			
0 (2H)	3.20	1.309	1.439
13.17	3.49	1.361	1.458
21.78	3.45	1.331	1.470
27.79	3.47	1.351	1.468
60 (3R)	3.19	1.261	1.421
WS$_2$			
0 (2H)	3.14	1.489	1.799
13.17	3.39	1.556	1.819
21.78	3.36	1.518	1.822
27.79	3.37	1.522	1.819
60 (3R)	3.14	1.454	1.786
WSe$_2$			
0 (2H)	3.19	1.431	1.504
13.17	3.46	1.518	1.534
21.78	3.41	1.469	1.530
27.79	3.43	1.491	1.533
60 (3R)	3.20	1.396	1.495

Table 4.1: Ab-initio calculations of the energy transitions (non-SOC) for MoS$_2$, MoSe$_2$, WS$_2$ and WSe$_2$ for the AA' bilayer structure and structures rotated at angles 21°, 27°, 13°, 33°, 38° and 60° (AA). d$_{vdW}$ is the van-der-Waals gap distance between adjacent monolayers. Angles are in degrees. NOTE: The bandgap of the WSe$_2$ structures occurs between K$_v$ and Σ_c. The bandgaps for the $\theta=0^o$, 13°, 21°, 27°, 60° structures are 1.409 eV, 1.430 eV, 1.433 eV and 1.434 eV and 1.410 eV respectively. Σ is the mid-point between Γ and K.

rotation angle is plotted in Fig. 4.3. For all of the commensurate rotation angles considered, the K high symmetry points in the rotated Brillouin zone map on to the same high symmetry points of the unrotated Brillouin zone. [125] For all 4 TMDCs, misorientation increases the bandgap with respect to that of the unrotated bilayer. This trend qualitatively agrees with the experimental data for MoS_2 that is also shown in Fig. 4.3. The twist angles for the experimental measurements for twisted bilayer MoS_2 from Ref. [117] range from 3° to 57°. All of the theoretically calculated values are well-aligned with the experimental ones, and they show the same trends. Extremely large supercells are required to model twist angles $0° < \theta < 13°$ and $50° < \theta < 60°$, so that in those ranges of angles, there are no theoretical values for comparison. For the range of angles $10° \leq \theta \leq 40°$, both the theory and the experiment show little change in the bandgap. For the full range of angles, the experimental indirect gap increases by ~ 140 meV compared to the indirect bandgap of the registered bilayer. The quantitative increase of the PBE non-SOC indirect gap is 200 meV.

The *direct* bandgap between K_v and K_c is less sensitive to misorientation betwen the layers. This trend is consistent among the 4 TMDC materials and with the experimental data [117, 119]. The increase in the bandgaps of the rotated structures occurs due to shifts in the the absolute energies of the valence band edges.

The changes in the bandgap as a function of rotation angle occurs due to changes in the interlayer vdW gap between the monolayers. This was previously explained due to configuration dependent steric effects that occur due to the different positions of the chalcogen atoms and the repulsive effects associated with the overlap of the p_z orbitals from each sulfur atom. [119] To further test this we optimized the misoriented bilayer structures using two different semi-empirical corrections of vdW interactions, the Grimme-D2 and the Tkatchenko-Scheffler correction. Each correction provides
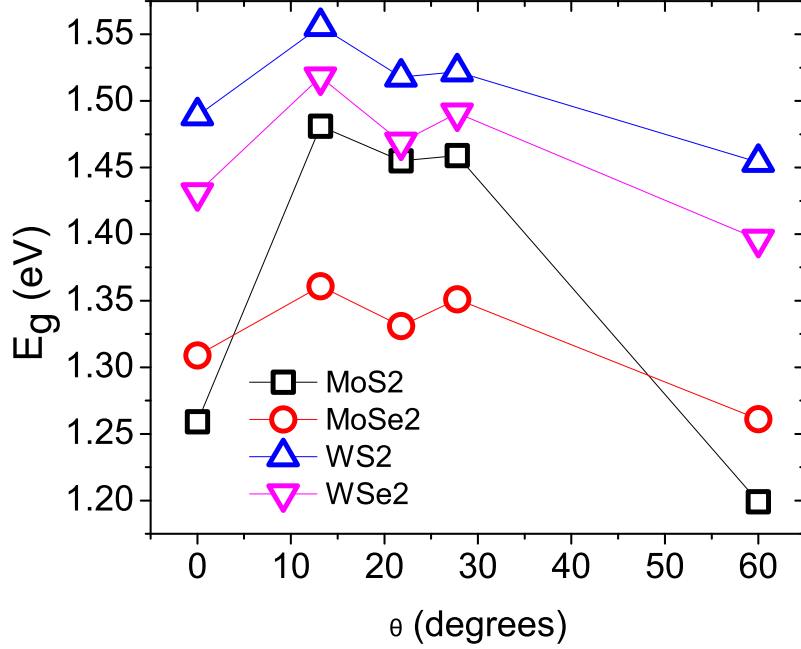
Figure 4.3: (Color online) Band gap energy as a function of rotation angle for MoS_2 ($\square$), $MoSe_2$ ($\circ$), WS_2 ($\triangle$), WSe_2 ($\triangledown$)

quantitatively similar interlayer van-der-Waal gap distances as a function of rotation angle. In the misoriented bilayers, the chalcogen atoms at the van-der-Waal interface have out-of-plane undulations up to $0.004\mathring{A}$ around the mean z-coordinate of the chalcogen atoms along the c-axis of the bilayer structure. Hence, the interlayer van-der-Waal gap, d_{vdW}, is defined as the distance between the average value of the z-coodinates of the chalcogen atoms at the interface between two monolayers. Rotation of the bilayer TMDC structures increases the vdW gap, d_{vdW}, between the two layers by as much as 9.7% compared to the vdW gap of the registered bilayer with 2H stacking. The values of d_{vdW} for all structures are given in Table 4.1 . The increase in d_{vdW} as a function of rotation angle with respect to the 0° structure is illustrated in Fig. 4.4
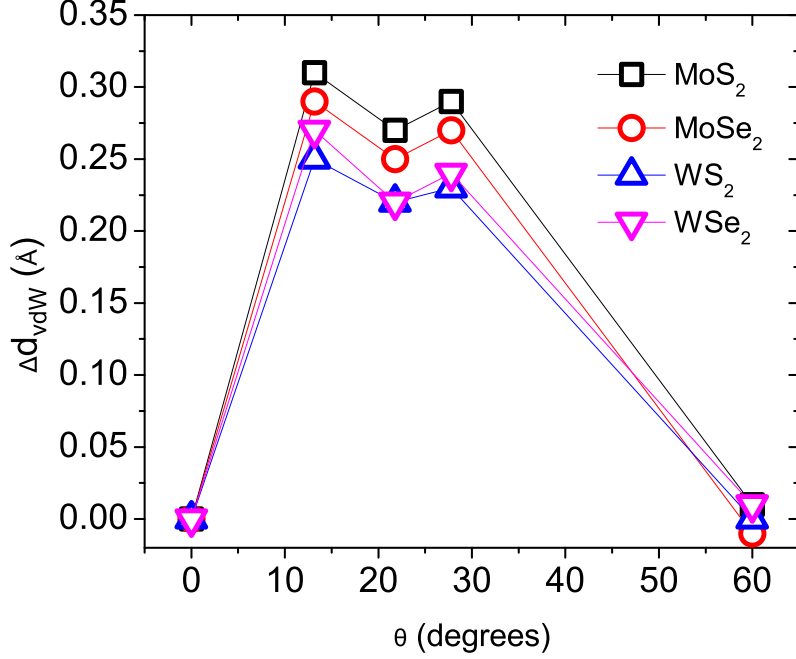
Figure 4.4: (Color online) Change in the van der Waals gap, $\Delta d_{\mathrm{vdW}} = d_{\mathrm{vdW}}(\theta) - d_{\mathrm{vdW}}(0)$, as a function of rotation angle for MoS_2 ($\square$), $MoSe_2$ ($\circ$), WS_2 ($\triangle$), WSe_2 ($\triangledown$

The increased separation between the rotated layers reduces the interlayer coupling. For the oriented and rotated bilayers of MoS_2, $MoSe_2$, WS_2, the valence band is at Γ and the conduction band is at K. For the oriented and rotated bilayers of WSe_2, the valence band is at K and the conduction band edge is at Σ. Since the band edges at Γ_v and K_c are primarily composed of p_z and d_{z^2} orbitals from the chalcogen and metal atoms [1, 107] they are more sensitive to rotation and changes in interlayer coupling. The K_v valley is composed of d_{xy}, d_{x^2} and p_{xy} orbitals which makes it insensitive to changes in twist angle. This reduction in interlayer coupling leads to shifts in the Γ_v, K_c and Σ_c valleys. The largest shift in energy is associated with the largest change in the interlayer vdW gap.

4.4 Conclusion

The electronic structure of bilayer MoS_2, $MoSe_2$, WS_2 and WSe_2 rotated by 21.78°, 27.79° and 13.17° are calculated using DFT with the PBE functional and the results are compared to the unrotated structures. Comparisons are made to calculations with spin-orbit coupling and the geometries of the bilayer structures optimized with the Grimme-D2 and the TS corrections applied are compared. Rotation of the bilayer structures increases the van-der-Waal distance between the individual monolayers by upto 9.7%, which reduces the interlayer coupling and increases the magnitude of the indirect bandgap for each material. The reduced interlayer coupling is driven by shifts in the absolute positions of the valence band Γ_v valley.

Chapter 5

Electronic and thermoelectric properties of van der Waals materials exhibiting ring shaped valence bands

5.1 Introduction

The electronic bandstructure of many two-dimensional (2D), van der Waals (vdW) materials qualitatively changes as the thickness is reduced down to a few monolayers. One well known example is the indirect to direct gap transition that occurs at monolayer thicknesses of the Mo and W transition metal dichalcogenides (TMDCs) [39]. Another qualitative change that occurs in a number of 2D materials is the inversion of the parabolic dispersion at a band extremum into a 'Mexican hat' dispersion. [128–130] Mexican hat dispersions are also referred to as a Lifshiftz transition [129,131,132], an electronic topological transition [133] or a camel-back dis-

persion [134, 135]. In a Mexican hat dispersion, the Fermi surface near the band-edge is approximately a ring in k-space, and the radius of the ring can be large, on the order of half of the Brillouin zone. The large degeneracy coincides with a singularity in the two-dimensional (2D) density of states close to the band edge. A similar feature occurs in monolayer Bi due to the Rashba splitting of the valence band. [136] This also results in a valence band edge that is a ring in k-space although the diameter of the ring is generally smaller than that of the Mexican hat dispersion. This also results in a valence band edge that is a ring in k-space although the diameter of the ring is generally smaller than that of the Mexican hat dispersion.

Mexican hat dispersions are relatively common in few-layer two-dimensional materials. Ab-initio studies have found Mexican hat dispersions in the valence band of many few-layer III-VI materials such as GaSe, GaS, InSe, InS [129, 130, 137–140]. Experimental studies have demonstrated synthesis of monolayers and or few layers of GaS, GaSe and InSe thin films. [10, 137, 141–145]. Monolayers of Bi_2Te_3 [70], and Bi_2Se_3 [146] also exhibit a Mexican hat dispersion in the valence band. The conduction and valence bands of bilayer graphene distort into Mexican hat dispersions when a a vertical field is applied across AB-stacked bilayer graphene. [128, 132, 147] The large density of states of the Mexican hat dispersion can lead to instabilities near the Fermi level, and two different ab initio studies have recently predicted Fermi-level controlled magnetism in monolayer GaSe and GaS [139, 140]. The singularity in the density of states and the large number of conducting modes at the band edge can enhance the Seebeck coefficient, power factor, and the thermoelectric figure of merit ZT. [148–150] Prior analytical studies of the thermoelectric power due to a Lifshitz transition demonstrated the thermopower is enhanced by up to a factor of 5 with respect to the thermopower for a constant energy iso-surface. [151].

The direct conversion from heat to electricity enabled by solid state thermoelectric

technology has been responsible for several NASA deep-space missions [152], exhaust heat recovery [153], and niche applications in the microelectronics industry. [154] Recent advancements in the ability to engineer the microstructure of a material combined with qualitative and quantitative predictions of the electronic and thermoelectric properties of materials provided by ab-initio and empirical simulations has led to a flurry of activity to identify suitable thermoelectric materials, as discussed in a number of review articles. [42, 155, 156] The thermoelectric performance of a material is gauged by the dimensionless figure of merit, ZT. The traditional way to maximize ZT is to either increase the power factor, PF, [157, 158] or reduce the lattice contribution to the thermal conductivity. [159, 160] Enhancing the density of states enhances the power factor.

Prior studies have achieved this enhancement in the density of states by using nanowires [41, 161], introducing resonant doping levels [149, 150], high band degeneracy [1, 162, 163], and using the Kondo resonance associated with the presence of localized d and f orbitals [164–166]. The large increase in ZT predicted for monolayer Bi_2Te_3 resulted from the formation of a Mexican hat bandstructure and its large band-edge degeneracy [45, 70]. Efforts to engineer the bandstructure often rely on the use of nanostructuring or the controlled introduction of dopants in quantum confined structures. [157, 158, 167, 168] Alteration of the material structure often leads to a degradation of one of the interrelated parameters; electrical conductivity, Seebeck or the thermal conductivity, which leads to a concomitant reduction in the thermoelectric figure of merit, ZT. Identifying materials with optimum electronic structures that intrinsically exhibit a high density of states could decouple the inter-dependent material parameters.

In the 2D materials mentioned above, the optimum electronic structure emerges at few-monolayer thicknesses. Used as single films, these materials could provide local

on-chip thermal management via active cooling [169], or they could perform energy scavenging [170]. An example of local on-chip passive thermal management was recently demonstrated using graphene as a heat spreader. [171] A common problem with exploiting low-dimensional materials is that to provide macroscopic power or transport macroscopic quantites of heat, a larger cross-section is required. [172] To achieve this, few-layer films would have to be stacked but separated sufficiently to prevent the interlayer coupling from destroying the few-layer electronic structure. One recent demonstrated approach is using intercalation to separate the layers. [173, 174] This approach reduces the deleterious effect of parallel heat conduction paths, provided that the filling factors of the intercalated gaps are relatively low such that the gaps primarily consist of vacuum.

This work theoretically investigates the electronic and thermoelectric properties of a variety of van der Waals materials that exhibit a Mexican hat dispersion or Rashba dispersion. The Mexican hat and Rashba dispersions are first analyzed using an analytical model. Then, density functional theory is used to calculate the electronic and thermoelectric properties of bulk and one to four monolayers of GaX, InX (X = Se, S), Bi_2Se_3, monolayer Bi(111), and bilayer graphene as a function of vertical electric field. Figure 5.1 illustrates the investigated structures that have either a Mexican hat or Rashba dispersion. The analytical model combined with the numerically calculated orbital compositions of the conduction and valence bands explain the layer dependent trends that are relatively consistent for all of the few-layer materials. While numerical values are provided for various thermoelectric metrics, the emphasis is on the layer-dependent trends and the analysis of how the bandstructure affects both the electronic and thermoelectric properties. The metrics are provided in such a way that new estimates can be readily obtained given new values for the electrical or thermal conductivity.

(a) GaS, GaSe, InS, InSe

(b) Bi$_2$Se$_3$

(c) Bilayer Graphene
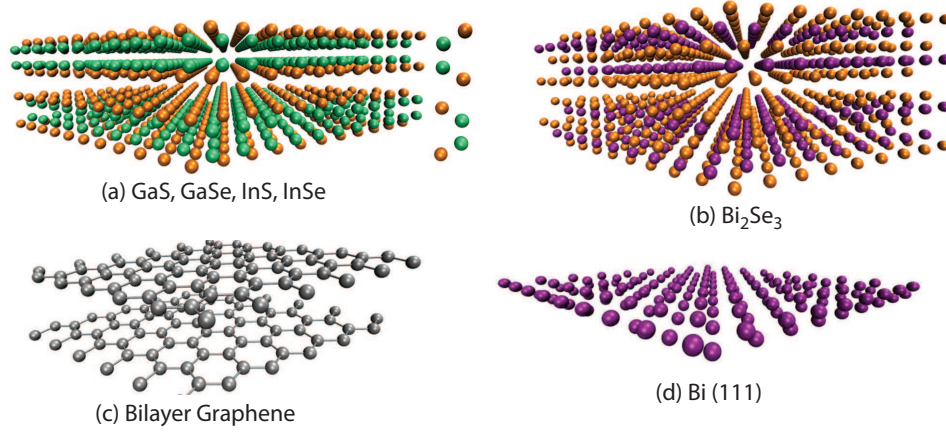
(d) Bi (111)

Figure 5.1: (Color online) Atomic structures of van-der Waals materials with a Mexican hat or Rashba dispersion: (a) Bilayer III-VI material. The β phase stacking geometry is shown at right. (b)Bi$_2$Se$_3$, (c) Bilayer Graphene and (d) Bi(111) monolayer

5.2 Models and Methods

5.2.1 Landauer Thermoelectric Parameters

In the linear response regime, the electronic and thermoelectric parameters are calculated within a Landauer formalism. The basic equations and their equivalence to standard equations resulting from the Boltzmann transport equation have been described previously, [85, 86] and we list them below for convenience. The equations for the electronic conductivity (σ), the electronic thermal conductivity (κ_e), and the

Seebeck coefficient (S) are

$$\sigma = (2q^2/h)I_0 \quad (\Omega^{-1}\mathrm{m}^{2-\mathrm{D}}), \tag{5.1}$$

$$\kappa_e = (2Tk_B^2/h)(I_2 - I_1^2/I_0) \quad (\mathrm{Wm}^{2-\mathrm{D}}\mathrm{K}^{-1}), \tag{5.2}$$

$$S = -(k_B/q)\frac{I_1}{I_0} \quad (\mathrm{V/K}), \tag{5.3}$$

with

$$I_j = L \int_{-\infty}^{\infty} \left(\frac{E - E_F}{k_B T}\right)^j \bar{T}(E) \left(-\frac{\partial f}{\partial E}\right) dE \tag{5.4}$$

where L is the device length, D is the dimensionality (1, 2, or 3), q is the magnitude of the electron charge, h is Planck's constant, k_B is Boltzmann's constant, and f is the Fermi-Dirac factor. In the diffusive limit, the transmission function $\bar{T}$ is

$$\bar{T}(E) = M(E)\lambda(E)/L \tag{5.5}$$

where M(E) as the density of modes, and $\lambda(E)$ is the electron mean free path. The power factor (PF) and the thermoelectric figure of merit (ZT) are given by $PF = S^2\sigma$ and

$$ZT = S^2\sigma T/(\kappa_l + \kappa_e) \tag{5.6}$$

where κ_l is the lattice thermal conductivity.

5.2.2 Analytical Models

As the thicknesses of the considered layered materials are reduced to a few monolayers, the valence band dispersion transitions from parabolic to Mexican hat. In this section, we consider analytical models to understand the effect of this band inversion on the electronic and thermoelectric properties. The trends and insight provided by the

analytical models provide a guide to understanding the numerical results that follow.

The single-spin density of modes for transport in the x direction is [85, 175]

$$M(E) = \frac{2\pi}{L^D} \sum_{\mathbf{k}} \delta(E - \epsilon(\mathbf{k})) \frac{\partial \varepsilon}{\partial k_x} \tag{5.7}$$

where D is the dimensionality, E is the energy, and $\varepsilon(\mathbf{k})$ is the band dispersion. The sum is over all values of $\mathbf{k}$ such that $\frac{\partial \varepsilon}{\partial k_x} > 0$, i.e. all momenta with positive velocities. The dimensions are $1/L^{D-1}$, so that in 2D, $M(E)$ gives the number of modes per unit width at energy E. If the dispersion is only a function of the magnitude of $\mathbf{k}$, then Eq. (5.7) reduces to

$$M(E) = \frac{N_D}{(2\pi)^{D-1}} \sum_b k_b^{D-1}(E) \tag{5.8}$$

where $N_D = \pi$ for $D = 3$, $N_D = 2$ for $D = 2$, and $N_D = 1$ for $D = 1$. k_b is the magnitude of $\mathbf{k}$ such that $E = \varepsilon(k_b)$, and the sum is over all bands and all values of k_b within a band. When a band-edge is a ring in k-space with radius k_0, the single-spin 2D density of modes at the band edge is

$$M(E_{\text{edge}}) = N \frac{k_0}{\pi}, \tag{5.9}$$

where N is either 1 or 2 depending on the type of dispersion, Rashba or Mexican hat. Thus, the 2D density of modes at the band edge depends only on the radius of of the k-space ring. For a two dimensional parabolic dispersion, $E = \frac{\hbar^2 k^2}{2m^*}$, the radius is 0, and Eq. (5.8) gives a the single-spin density of modes of [87]

$$M_{\text{par}}(E) = \frac{\sqrt{2m^* E}}{\pi \hbar}. \tag{5.10}$$

In real III-VI materials, there is anisotropy in the Fermi surfaces, and a 6th order,

angular dependent polynomial expression is provided by Zólyomi et al. that captures the low-energy anisotropy [129, 130]. To obtain physical insight with closed form expressions, we consider a 4th order analytical form for an isotropic Mexican hat dispersion

$$\epsilon(k) = \epsilon_0 - \frac{\hbar^2 k^2}{2m^*} + \frac{1}{4\epsilon_0}\left(\frac{\hbar^2 k^2}{2m^*}\right)^2 \tag{5.11}$$

where ε_0 is the height of the hat at $k = 0$, and m^* is the magnitude of the effective mass at $k = 0$. A similar quartic form was previously used to analyze the effect of electron-electron interactions in biased bilayer graphene [128]. The function is plotted in Figure 5.2(a). The band edge occurs at $\varepsilon = 0$, and, in k-space, in two dimensions (2D), it forms a ring in the $k_x - k_y$ plane with a radius of

$$k_0^{\mathrm{MH}} = \frac{2\sqrt{m^*\varepsilon_0}}{\hbar}. \tag{5.12}$$

For the two-dimensional Mexican hat dispersion of Eq. (5.11), the single-spin density of modes is

$$M_{\mathrm{MH}}(E) = \begin{cases} \frac{k_0^{\mathrm{MH}}}{\pi}\left(\sqrt{1+\sqrt{\frac{E}{\epsilon_0}}} + \sqrt{1-\sqrt{\frac{E}{\epsilon_0}}}\right) & (0 \leq E \leq \varepsilon_0) \\ \frac{k_0^{\mathrm{MH}}}{\pi}\left(\sqrt{1+\sqrt{\frac{E}{\epsilon_0}}}\right) & (\varepsilon_0 \leq E). \end{cases} \tag{5.13}$$

Figure 5.2(b) shows the density of mode distributions plotted from Eqs. (5.10) and (5.13). At the band edge ($E = 0$), the single-spin density of modes of the Mexican hat dispersion is finite,

$$M_{\mathrm{MH}}(E = 0) = \frac{2k_0^{\mathrm{MH}}}{\pi}. \tag{5.14}$$

The Mexican hat density of modes decreases by a factor of $\sqrt{2}$ as the energy increases from 0 to ε_0, and then it slowly increases. The step-function turn-on of the density of
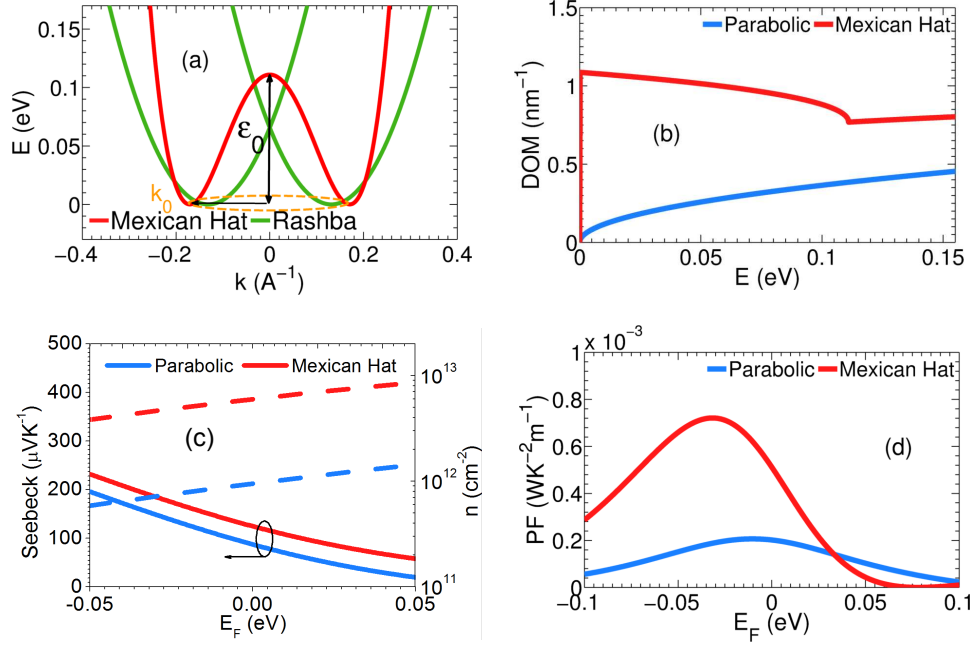
Figure 5.2: (Color online) (a) Comparison of a Mexican hat dispersion (red) and a Rashba dispersion (green). The band edges are rings in k-space with radius k_0 illustrated for the Mexican hat band by the orange dotted circle. The height of the Mexican hat band at $k = 0$ is $\epsilon_0 = 0.111$ eV. The Rashba parameter is 1.0 eV Å, and the effective mass for both dispersions is $0.5m_0$. (b) Density of modes of the Mexican hat dispersion (red) versus parabolic band (blue). The parabolic dispersion also has an effective mass of 0.5. (c) Room temperature Seebeck coefficients (solid lines) and carrier concentrations (broken lines) of the Mexican hat band (red) and the parabolic band (blue) as a function of Fermi level position, E_F. (d) Room temperature ballistic power factor of the Mexican hat band (red) and the parabolic band (blue) calculated from Eqs. (5.1), (5.3), and (5.4) with $T(E) = 1$.

modes is associated with a singularity in the density of states. The single-spin density of states resulting from the Mexican hat dispersion is

$$
D_{\mathrm{MH}}(E) = \begin{cases} \frac{m^*}{\pi\hbar^2}\sqrt{\frac{\varepsilon_0}{E}} & (0 \leq E \leq \varepsilon_0) \\[2mm] \frac{m^*}{2\pi\hbar^2}\sqrt{\frac{\varepsilon_0}{E}} & (\varepsilon_0 < E) \ . \end{cases} \tag{5.15}
$$

Rashba splitting of the spins also results in a valence band edge that is a ring in k-space. The Bychkov-Rashba model with linear and quadratic terms in k gives an

analytical expression for a Rashba-split dispersion, [176]

$$\varepsilon(\mathbf{k}) = \varepsilon_0 + \frac{\hbar^2 k^2}{2m^*} \pm \alpha_R k \tag{5.16}$$

where the Rashba parameter, α_R, is the strength of the Rashba splitting. In Eq. (5.16), the bands are shifted up by $\varepsilon_0 = \frac{\alpha_R^2 m^*}{2\hbar^2}$ so that the band edge occurs at $\varepsilon = 0$. The radius of the band edge in k-space is

$$k_0^{\mathrm{R}} = \frac{m^* \alpha_R}{\hbar^2} = \frac{\sqrt{2m^* \varepsilon_0}}{\hbar}. \tag{5.17}$$

The energy dispersion of the split bands is illustrated in Figure 5.2(a). The density of modes, *including both spins*, resulting from the dispersion of Eq. (5.16) is

$$M_{\mathrm{R}}^{2\,\mathrm{spins}}(E) = \begin{cases} \frac{2k_0^{\mathrm{R}}}{\pi} & (0 \leq E \leq \varepsilon_0) \\ \frac{2k_0^{\mathrm{R}}}{\pi}\sqrt{\frac{E}{\varepsilon_0}} & (\varepsilon_0 \leq E) \end{cases} \tag{5.18}$$

For $0 \leq E \leq \varepsilon_0$, the density of modes is a step function and the height is determined by α_R and the effective mass. Values for α_R vary from 0.07 eVÅ in InGaAs/InAlAs quantum wells to 0.5 eVÅ in the Bi(111) monolayer. [177] The density of states including both spins is

$$D_{\mathrm{R}}(E) = \begin{cases} \frac{m^*}{\pi\hbar^2}\sqrt{\frac{\varepsilon_0}{E}} & (0 \leq E \leq \varepsilon_0) \\ \frac{m^*}{\pi\hbar^2} & (\varepsilon_0 < E) \end{cases} \tag{5.19}$$

In general, we find that the diameter of the Rashba k-space rings are less than the diameter of the Mexican hat k-space rings, so that the enhacements to the thermoelectric parameters are less from Rashba-split bands than from the inverted Mexican hat bands.

Figure 5.2(c) compares the Seebeck coefficients and the electron densities calculated from the Mexican hat dispersion shown in Fig. 5.2(a) and a parabolic dispersion. The quantities are plotted versus Fermi energy with the conduction band edge at $E = 0$. An electron effective mass of $m^* = 0.5m_0$ is used for both dispersions, and, for the Mexican hat, $\epsilon_0 = 0.111$ eV which is the largest value for ϵ_0 obtained from our ab-initio simulations of the III-VI compounds. The temperature is $T = 300$ K. The Seebeck coefficients are calculated from Eqs. (5.3), (5.4), and (5.5) with $T(E) = 1$. The electron densities are calculated from the density of state functions given by two times Eq. (5.15) for the Mexican hat dispersion and by $m^*/\pi\hbar^2$ for the parabolic dispersion. The electron density of the Mexican hat dispersion is approximately 6 times larger than that of the parabolic dispersion at a fixed Fermi energy. This is a result of the singular density of states at the bandedge of the Mexican hat dispersion. There are two important points to take away from this plot. At the same electron density, the Fermi level of the Mexican hat dispersion is much lower than that of the parabolic dispersion. As a result, at the same electron density, the Seebeck coefficient of the Mexican hat dispersion is much larger than the Seebeck coefficient of the parabolic dispersion.

Figure 5.2(d) compares the ballistic power factors calculated from the Mexican hat dispersion shown in Fig. 5.2(a) and the parabolic dispersion, again with $m^* = 0.5m_0$ for both dispersions. The temperature is $T = 300$ K. The ballistic power factor is calculated from Eqs. (5.1), (5.3), (5.4), and (5.5) with $T(E) = 1$. Eqs. (5.10) and (5.13) for the density of modes are used in Eq. (5.5). The peak power factor of the Mexican hat dispersion occurs when $E_F = $ -32 meV, i.e. 32 meV below the conduction band edge. The peak power factor of the parabolic dispersion occurs when $E_F = $ -9.5 meV. At the peak power factors, the value of I_1 of the Mexican hat dispersion is 3.5 times larger than I_1 of the parabolic dispersion, and I_0 of the Mexican hat dispersion

is 3.2 times larger than I_0 of the parabolic dispersion. I_0 gives the conductivity, the ratio I_1/I_0 gives the Seebeck coefficient, and I_1^2/I_0 gives the power factor. Therefore, the inversion of the parabolic band into a Mexican hat band results in an increase in the Seebeck coefficient and a large increase in the peak power factor. This is the trend that we consistently observe in the numerical simulations as the bands invert from a parabolic to a Mexican hat dispersion as the number of layers is reduced.

From the Landauer-Büttiker perspective of Eq. (5.5), the increased conductivity results from the increased number of modes near the bandedge as shown in Fig. 5.2(b). From a more traditional perspective, the increased conductivity results from an increased density of states resulting in an increased charge density n. At their peak power factors, the charge density of the Mexican hat dispersion is 4.9×10^{12} cm^{-2}, and the charge density of the parabolic dispersion is 1.5×10^{12} cm^{-2}. The charge density of the Mexican hat dispersion is 3.3 times larger than the charge density of the parabolic dispersion even though the Fermi level for the Mexican hat dispersion is 22 meV less than the Fermi level of the parabolic dispersion. This, in general, will result in a higher conductivity. These trends are consistently followed by the numerical results. The above analytical discussion illustrates the basic concepts and trends concerning the relationship between the Mexican hat dispersion and the electronic and thermoelectric parameters, and it motivates and guides the following numerical investigation of various van der Waals materials exhibiting either Mexican hat or Rashba dispersions.

5.2.3 Computational Methods

Ab-initio calculations of the bulk and few-layer structures (one to four layers) of GaS, GaSe, InS, InSe, Bi$_2$Se$_3$, Bi(111) surface, and bilayer graphene are carried out using

density functional theory (DFT) with a projector augmented wave method [78] and the Perdew-Burke-Ernzerhof (PBE) type generalized gradient approximation [79, 80] as implemented in the Vienna ab-initio Simulation Package (VASP). [81, 82] The vdW interactions in GaS, GaSe, InS, InSe and Bi_2Se_3 are accounted for using a semi-empirical Grimme-D2 correction to the Kohn-Sham energies when optimizing the bulk structures of each material. [83] All atomic positions were fully optimized until the forces acting on each atom are less than 0.01 eV/Å. The thickness of each bulk unit cell optimized with the Grimme-D2 potential is within 1.6% of the bulk experimental data for each material. For the GaX, InX (X = S,Se), Bi(111) monolayer, and Bi_2Se_3 structures, a Monkhorst-Pack scheme is used for the integration of the Brillouin zone with a k-mesh of 12 x 12 x 6 for the bulk structures and 12 x 12 x 1 for the thin-films. The energy cutoff of the plane wave basis is 300 eV. The electronic bandstructure calculations include spin-orbit coupling (SOC) for the GaX, InX, Bi(111) and Bi_2Se_3 compounds. To verify the results of the PBE band structure calculations of the GaX and InX compounds, the electronic structures of one to four monolayers of GaS and InSe are calculated using the Heyd-Scuseria-Ernzerhof (HSE) functional. [84] The HSE calculations incorporate 25% short-range Hartree-Fock exchange. The screening parameter μ is set to 0.2 Å^{-1}. For the calculations on bilayer graphene, a 32 × 32 × 1 k-point grid is used for the integration over the Brillouin zone. The energy cutoff of the plane wave basis is 400 eV. 15Å of vacuum spacing was added to the slab geometries of all few-layer structures. The optimized lattice parameters for each of the materials studied are listed in Table 5.1 below. Band structures of the monolayer and few-layer structures are calculated using the lattice constants of the optimized bulk structures. The conduction and valence band effective masses at Γ are calculated for each material by fitting the dispersion to a sixth order polynomial and then calculating $\frac{1}{m^*} = \frac{1}{\hbar^2}\frac{\partial^2 E}{\partial k^2}$.

	a_0(Å)	c_0(Å)	d (Å)	d_{vdW} (Å)	a_0^{expt}(Å)	c_0^{expt}(Å)	d^{expt} (Å)
GaS	3.630	15.701	4.666	3.184	3.587	15.492	4.599
GaSe	3.755	15.898	4.870	3.079	3.752	15.950	4.941
InS	3.818	15.942	5.193	2.780	. . .	. . .	. . .
InSe	4.028	16.907	5.412	3.040	4.000	16.640	5.557
Bi$_2$Se$_3$	4.140	28.732	7.412	3.320	4.143	28.636	. . .
BLG	2.459	-	3.349	3.349	2.460	-	3.400
Bi(111)	4.34	-	3.049	-	4.54	-	-

Table 5.1: Calculated and experimental properties of bulk Mexican-hat materials GaS, GaSe, InS, InSe, Bi$_2$Se$_3$, bilayer graphene (BLG), and Bi(111). The in-plane and c-axis lattice constants are a_0 and c_0, respectively. The thickness of an individual layer is d, and the van-der-Waal distance between individual monolayers is d$_{vdW}$. The calculated thickness, d, is the atom-center to atom-center distance between the top and bottom chalcogen atoms of a single layer in GaS, GaSe, InS, InSe, Bi$_2$Se$_3$ and atom center to atom center distance of the top and bottom carbon atoms in bilayer graphene. The thickness d in monolayer Bi is the height of the buckling distance between the two Bi atoms. Experimental values when available [7–12] are included for comparison.

The ab-initio calculations of the electronic structure are used as input for calculating the thermoelectric parameters. The two quantities requred are the density of states and the density of modes. The density of states is directly provided by VASP. The density of modes calculations are performed by integrating over the first Brillouin zone using a converged k-point grid, $51 \times 51 \times 10$ k-points for the bulk structures and $51 \times 51 \times 1$ k-points for the III-VI, Bi$_2$Se$_3$ and Bi(111) thin film structures. A $101 \times 101 \times 1$ grid of k-points is required for the density of mode calculations on bilayer graphene. The details of the formalism are provided in several prior studies. [1,45,86] The temperature dependent carrier concentrations for each material and thickness are calculated from the density-of-states obtained from the ab-initio simulations. To obtain a converged density-of-states a minimum k-point grid of $72 \times 72 \times 36$ ($72 \times 72 \times 1$) is required for the bulk (monolayer and few-layer) III-VI and Bi$_2$Se$_3$ structures. For the density-of-states calculations on bilayer graphene and monolayer Bi(111) a $36 \times 36 \times 1$

grid of k-points is used.

The calculation of the in-plane thermoelectric parameters, such as conductivity, the power factor, and ZT, requires values for the electron and hole mean free paths and the lattice thermal conductivity. Electron and hole scattering are included using an average mean free path, λ determined by matching Eq. (5.1) to literature conductivity data using an average value for λ in Eq. (5.5). The definition of the average λ is

$$\lambda = \frac{\int dE M(E) \lambda(E) \left(\frac{\partial f}{\partial E}\right)}{\int dE M(E) \left(\frac{\partial f}{\partial E}\right)}. \tag{5.20}$$

It is the average mean free path per mode in the thermal transport window of a few $k_B T$ defined by $(-\partial f / \partial E)$. For all of the few-layer materials, the peak ZT occurs when E_F is in the band gap, below the conduction band edge for n-type material or above the valence band edge for p-type material. Therefore, only the low-energy states within a few $k_B T$ of the band-edges contribute to the transport.

For GaS, GaSe, InS and InSe, $\lambda_0 = 25$ nm gives the best agreement with experimental data. [178–181] The room temperature bulk n-type electrical conductivity of GaS, GaSe, InS and InSe was reported to be 0.5 $\Omega^{-1}\mathrm{m}^{-1}$, 0.4 $\Omega^{-1}\mathrm{m}^{-1}$, 0.052 $\Omega^{-1}\mathrm{m}^{-1}$ and 0.066 $\Omega^{-1}\mathrm{m}^{-1}$, respectively, at a carrier concentration of 10^{16} cm^{-3}. Using $\lambda_0 = 25$ nm for bulk GaS, GaSe and InSe we obtain an electrical conductivity of 0.58 $\Omega^{-1}\mathrm{m}^{-1}$, 0.42 $\Omega^{-1}\mathrm{m}^{-1}$, 0.058 $\Omega^{-1}\mathrm{m}^{-1}$ and 0.071 $\Omega^{-1}\mathrm{m}^{-1}$, respectively at the same carrier concentration. For the Bi(111) monolayer surface, the electrical conductivity at 300K is reported to be of 0.011 $\Omega^{-1}\mathrm{m}^{-1}$ at a carrier concentration of 2.6×10^{18} cm^{-3}. [182] An electron and hole mean free path of 4.7nm gives the best agreement with the electrical conductivity of bulk Bi. For Bi$_2$Se$_3$ an electron mean free path, λ_e=5.2nm and a hole mean free path, λ_p=2.1 nm, gives the best agreement with experimental data on conductivity for bulk single crystal Bi$_2$Se$_3$. [183] The room temperature bulk n-type

69

electrical conductivity is reported to be 1.5 Ω^{-1}m^{-1} at a carrier concentration of 10^{17} cm^{-3} and the p-type electrical conductivity at room temperature is 4.8 Ω^{-1}m^{-1} at a carrier concentration of 10^{19} cm^{-3} For bilayer graphene, $\lambda_0 = 88$ nm gives the best agreement with experimental data on conductivity at room temperature. [184]

Values for the lattice thermal conductivity are also taken from available experimental data. The experimental value of 10 Wm^{-1}K^{-1} reported for the in-plane lattice thermal conductivity κ_l of bulk GaS at room temperature is used for the gallium chalcogenides. [185] The experimental, bulk, in-plane, lattice thermal conductivities of 7.1 Wm^{-1}K^{-1} and 12.0 Wm^{-1}K^{-1} measured at room temperature are used for InS and InSe, respectively. [186] For monolayer Bi(111), the calculated κ_l from molecular dynamics [187] at 300K is 3.9 Wm^{-1}K^{-1}. For Bi$_2$Se$_3$, the measured bulk κ_l value at 300K is 2 Wm^{-1}K^{-1}. [183, 188] A value of 2000 Wm^{-1}K^{-1} is used for the room temperature in-plane lattice thermal conductivity of bilayer graphene. This is consistent with a number of experimental measurements and theoretical predictions on the lattice thermal conductivity of bilayer graphene. [189, 190] Prior studies of thermal conductivity in the layered chalcogenides and few layer graphene have demonstrated that κ_l can vary by up to a factor of 2 as the film thickness decreases from bulk to a monolayer. [103, 106, 191] Maximum and minimum values for ZT are calculated for GaS, GaSe, InS, InSe and Bi$_2$Se$_3$ using the bulk values of κ_l and twice the bulk values of κ_l.

When evaluating ZT in Eq. (5.6) for the 2D thin film structures, the bulk lattice thermal conductivity is multiplied by the film thickness. When tabulating values of the electrical conductivity and the power factor of the 2D films, the calculated conductivity from Eq. (5.1) is divided by the film thickness.

Much of the experimental data from which the values for λ_0 and κ_l have been determined are from bulk studies, and clearly these values might change as the materials

are thinned down to a few monolayers. However, there are presently no experimental values available for few-layer III-VI and Bi_2Se_3 materials. Our primary objective is to obtain a qualitative understanding of the effect of the bandstructure in these materials on their thermoelectric properties. To do so, we use the above values for λ_0 and κ_l to calculate ZT for each material as a function of thickness. We tabulate these values and provide the corresponding values for the electron or hole density, Seebeck coefficient, and conductivity at maximum ZT. It is clear from Eqs. (5.3) and (5.4) that the Seebeck coefficient is relatively insensitive to the value of the mean free path. Therefore, if more accurate values for the conductivity or κ_l become available, new values for ZT can be estimated from Eq. (5.6) using the given Seebeck coefficient and replacing the electrical and/or thermal conductivity.

5.3   Numerical Results

5.3.1   III-VI Compounds GaX and InX (X = S, Se)

The lattice parameters of the optimized bulk GaX and InX compounds are summarized in Table 5.1. In this study, the default stacking is the β phase illustrated in Fig. 5.2a. The β phase is isostructural to the AA' stacking order in the 2H polytypes of the molybdenum and tungsten dichalcogenides. [115] The bandgap of the one to four monolayer structures is indirect for GaS, GaSe, InS and InSe. Figure 5.3 illustrates the PBE band structure for one-layer (1L) through four-layers (4L), eight-layer (8L) and bulk GaS. The PBE SOC band gaps and energy transitions for each of the III-VI materials and film thicknesses are listed in Table 5.2. For GaS, the HSE SOC values are also listed. The effective masses extracted from the PBE SOC electronic bandstructure are listed in Table 5.3.

Structure	Transition	GaS	GaSe	InS	InSe
1L	E_v to Γ_c	2.563 (3.707)	2.145	2.104	1.618
	E_v to K_c	2.769 (3.502)	2.598	2.684	2.551
	E_v to M_c	2.549 (3.422)	2.283	2.520	2.246
2L	E_v to Γ_c	2.369 (3.156)	1.894	1.888	1.332
	E_v to K_c	2.606 (3.454)	2.389	2.567	2.340
	E_v to M_c	2.389 (3.406)	2.065	2.353	2.025
3L	E_v to Γ_c	2.288 (3.089)	1.782	1.789	1.152
	E_v to K_c	2.543 (3.408)	2.302	2.496	2.201
	E_v to M_c	2.321 (3.352)	1.967	2.273	1.867
4L	E_v to Γ_c	2.228 (3.011)	1.689	1.749	1.086
	E_v to K_c	2.496 (3.392)	2.224	2.471	2.085
	E_v to M_c	2.267 (3.321)	1.879	2.242	1.785
Bulk	Γ_v to Γ_c	1.691 (2.705)	0.869	0.949	0.399
	Γ_v to K_c	1.983 (2.582)	1.435	1.734	1.584
	Γ_v to M_c	1.667 (2.391)	0.964	1.400	1.120

Table 5.2: PBE SOC calculations of the bandgap energies and energy transitions between the valence band edge of the Mexican hat band (E_v) and the conduction (c) band valleys for 1L to 4L GaS, GaSe, InS and InSe. The bandgap at each dimension is highlighted in bold text. The HSE-SOC energy transitions for GaS are in parentheses.

Structure	GaS	GaSe	InS	InSe	GaS	GaSe	InS	InSe
	Hole Effective Mass (m_0)				Electron Effective Mass (m_0)			
1L	0.409	0.544	0.602	0.912	0.067 (0.698)	0.053	0.080	0.060
2L	0.600	0.906	0.930	1.874	0.065 (0.699)	0.051	0.075	0.055
3L	0.746	1.439	1.329	6.260	0.064 (0.711)	0.050	0.074	0.053
4L	0.926	2.857	1.550	3.611	0.064 (0.716)	0.049	0.073	0.055

Table 5.3: Ab-initio calculations of the hole and electron effective masses at the Γ valley of the valence band and conduction band respectively for each structure in units of the free electron mass (m_0). The conduction band effective masses at M_c are included in parentheses for one to four layers of GaS.
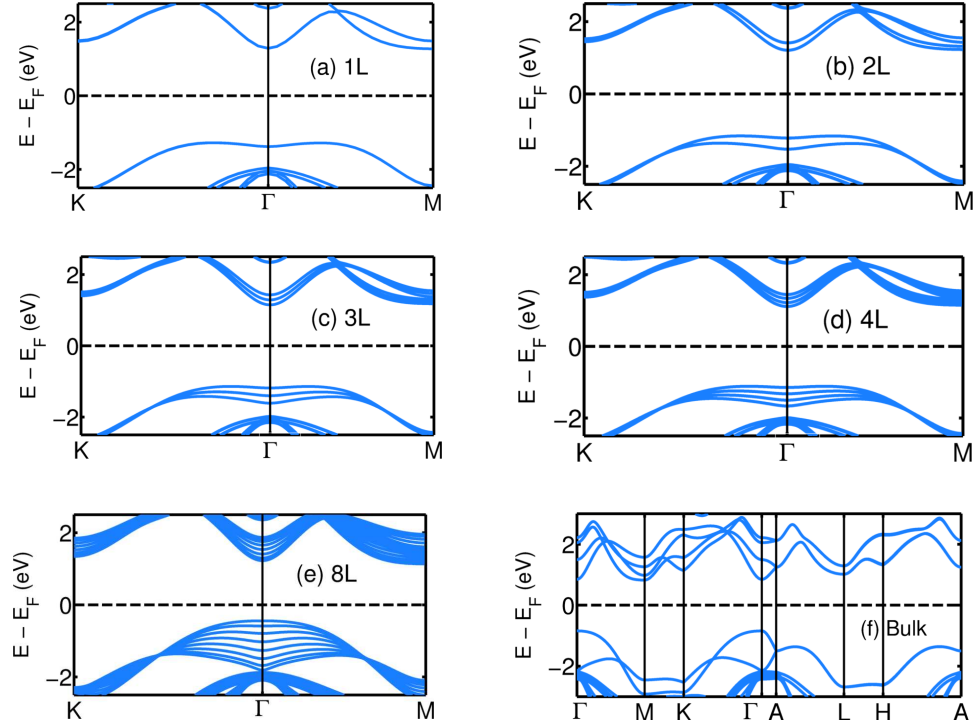
Figure 5.3: (Color online) PBE SOC band structure of GaS: (a) 1L, (b) 2L, (c) 3L and (d) 4L, (e) 8L and (f) bulk GaS.

The conduction band minimum of GaSe, InS, and InSe are at Γ for all layer thicknesses, from monolayer to bulk. The conduction band minimum of monolayer GaS is at M. This result is consistent with that of Zólyomi et al. [129]. However, for all thicknesses greater than a monolayer, the conduction band of GaS is at Γ. Results from the PBE functional give GaS conduction valley separations between M and Γ that are on the order of $k_B T$ at room temperature, and this leads to qualitatively incorrect results in the calculation of the electronic and thermoelectric parameters. For the three other III-VI compounds, the minimum PBE-SOC spacing between the conduction Γ and M valleys is 138 meV in monolayer GaSe. For InS and InSe, the minimum conduction Γ-M valley separations also occur for a monolayer, and they are 416 eV and 628 eV, respectively. For monolayer GaS, the HSE-SOC conduction M valley lies 80 meV below the K valley and 285 meV below the Γ valley. At two to four

73

layer thicknesses, the order is reversed, the conduction band edge is at Γ, and the energy differences between the valleys increase. For the electronic and thermoelectric properties, only energies within a few $k_B T$ of the band edges are important. Therefore, the density of modes of n-type GaS is calculated from the HSE-SOC bandstructure. For p-type GaS and all other materials, the densities of modes are calculated from the PBE-SOC bandstructure.

The orbital composition of the monolayer GaS conduction Γ valley contains 63% Ga s orbitals and 21% S p_z orbitals. The orbital compositions of the other III-VI conduction Γ valleys are similar. As the film thickness increases from a monolayer to a bilayer, the conduction Γ valleys in each layer couple and split by 203 meV as shown in Fig. 5.3b. Thus, as the film thickness increases, the number of low-energy Γ states near the conduction band-edge remains the same, or, saying it another way, the number of low-energy Γ states per unit thickness decreases by a factor of two as the the number of layers increases from a monolayer to a bilayer. This affects the electronic and thermoelectric properties.

The Mexican hat feature of the valence band is present in all of the 1L - 4L GaX and InX structures, and it is most pronounced for the monolayer structure shown in Fig. 5.3a. For monolayer GaS, the highest valence band at Γ is composed of 79% sulfur p_z orbitals (p_z^S). The lower 4 valence bands at Γ are composed entirely of sulfur p_x and p_y orbitals (p_{xy}^S). When multiple layers are brought together, the p_z^S valence band at Γ strongly couples and splits with a splitting of 307 meV in the bilayer. For the 8-layer structure in Fig. 5.3e, the manifold of 8 p_z^S bands touches the manifold of p_{xy}^S bands, and the bandstructure is bulklike with discrete k_z momenta. In the bulk shown in Fig. 5.3f, the discrete energies become a continuous dispersion from Γ to A. At 8 layer thickness, the large splitting of the p_z^S valence band removes the Mexican hat feature, and the valence band edge is parabolic as in the bulk. The nature and

orbital composition of the bands of the 4 III-VI compounds are qualitatively the same.

Material (Theory/Stacking Order)	ε_0 (meV) 1L, 2L, 3L, 4L	k_0 (nm^{-1}) 1L, 2L, 3L, 4L
GaS	111.2, 59.6, 43.8, 33.0	3.68, 2.73, 2.52, 2.32
GaS (no-SOC)	108.3, 60.9, 45.1, 34.1	3.16, 2.63, 2.32, 2.12
GaS (HSE)	97.9, 50.3, 40.9, 31.6	2.81, 2.39, 2.08, 1.75
GaS (AA)	111.2, 71.5, 57.1, 47.4	3.68, 2.93, 2.73, 2.49
GaSe	58.7, 29.3, 18.1, 10.3	2.64, 2.34, 1.66, 1.56
GaSe (ϵ)	58.7, 41.2, 23.7 , 5.1	2.64, 1.76, 1.17 , 1.01
InS	100.6, 44.7, 25.8, 20.4	4.03, 3.07, 2.69, 2.39
InSe	34.9, 11.9, 5.1, 6.1	2.55, 1.73, 1.27, 1.36
InSe (HSE)	38.2, 15.2, 8.6, 9.2	2.72, 2.20, 1.97, 2.04
Bi$_2$Se$_3$	314.7, 62.3, 12.4, 10.4	3.86, 1.23, 1.05, 0.88
Bi$_2$Se$_3$ (no-SOC)	350.5, 74.6, 22.8, 20.1	4.19, 1.47, 1.07, 1.02

Table 5.4: Values of ε_0 and k_0 are listed in order of thicknesses: 1L, 2L, 3L, and 4L. The default level of theory is PBE with spin-orbit coupling, and the default stacking is AA'. Only deviations from the defaults are noted.

In the few-layer structures, the Mexican hat feature of the valence band can be characterized by the height, ϵ_0, at Γ and the radius of the band-edge ring, k_0, as illustrated in Figure 5.2(b). The actual ring has a small anisotropy that has been previously characterized and discussed in detail [129,130,139]. For all four III-VI compounds of monolayer and few-layer thicknesses, the valence band maximum (VBM) of the inverted Mexican hat lies along $\Gamma - K$, and it is slightly higher in energy compared to the band extremum along $\Gamma - M$. In monolayer GaS, the valence band maximum along $\Gamma - K$ is 4.7 meV above the band extremum along $\Gamma - M$. In GaS, as the film thickness increases from one layer to four layers the energy difference between the two extrema decreases from 4.7 meV to 0.41 meV. The maximum energy difference of 6.6 meV between the band extrema of the Mexican hat occurs in a monolayer of InS. In all four III-VI compounds the energy difference between the band extrema is maximum for the monolayer structure and decreases below 0.5 meV in all of the materials for the four-layer structure. The tabulated values of k_0 in Table 5.4 give the
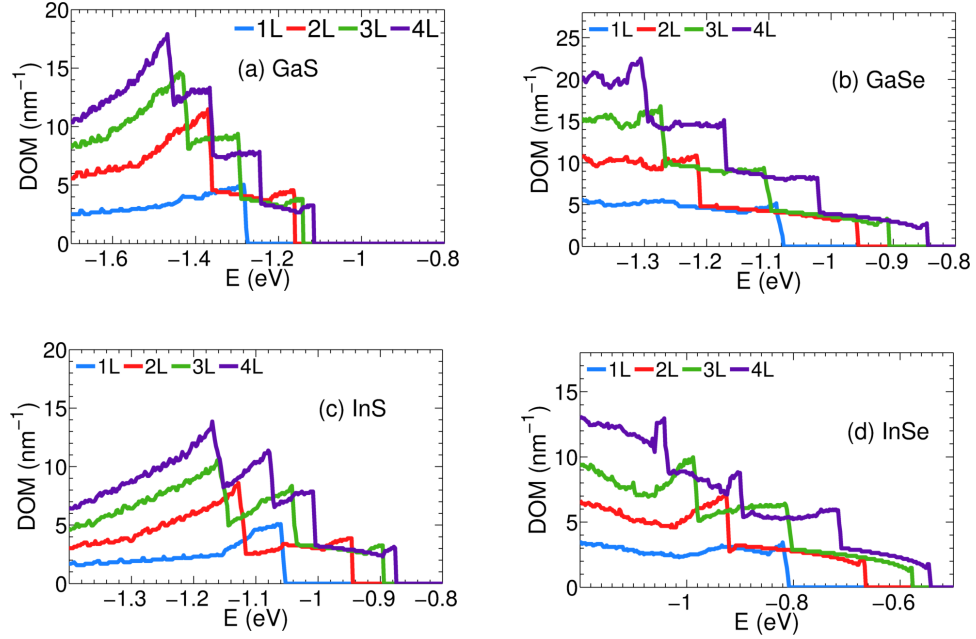
Figure 5.4: (Color online) Distribution of valence band modes per unit width versus energy for (a) GaS, (b) GaSe, (c) InS and (d) InSe for 1L (blue), 2L (red), 3L (green) and 4L (purple) structures. The midgap energy is set to E=0.

distance from Γ to the VBM in the $\Gamma - K$ direction. Results calculated from PBE and HSE functionals are given, and results with and without spin-orbit coupling are listed. The effects of AA' versus AA stacking order of GaS and AA' versus ϵ stacking order of GaSe [192, 193] are also compared.

Table 5.4 shows that the valence band Mexican hat feature is robust. It is little affected by the choice of functional, the omission or inclusion of spin-orbit coupling, or the stacking order. A recent study of GaSe at the G_0W_0 level found that the Mexican hat feature is also robust against many-electron self-energy effects. [139] For all materials, the values of ϵ_0 and k_0 are largest for monolayers and decrease as the film thicknesses increase. This suggests that the height of the step function density of modes will also be maximum for the monolayer structures.

Figure 5.4 illustrates the valence band density of modes for 1L, 2L, 3L and 4L
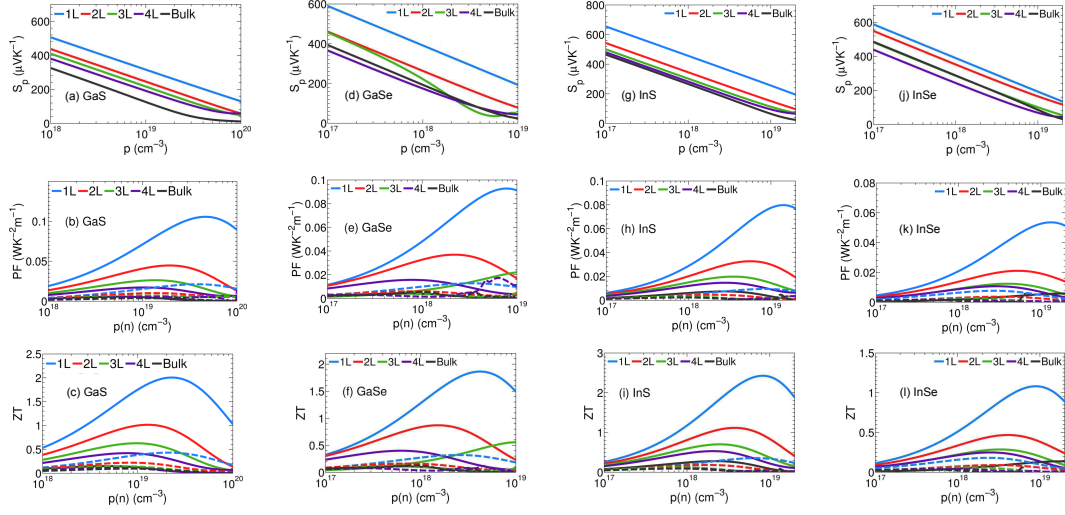
Figure 5.5: (Color online) Seebeck coefficient, power factor and thermoelectric figure-of-merit, ZT, of p-type (solid line) and n-type (broken line) 1L (blue), 2L (red), 3L (green), 4L (purple) and bulk (black) (a)-(c) GaS, (d)-(f) GaSe, (g)-(i) InS and (j)-(l) InSe at room temperature.

GaS, GaSe, InS and InSe. The valence band density of modes is a step function for the few-layer structures, and the height of the step function at the valence band edge is reasonably approximated by Eq. (5.14). The height of the numerically calculated density of modes step function for monolayer GaS, GaSe, InS and InSe is 4.8 nm^{-1}, 5.2 nm^{-1}, 5.1 nm^{-1} and 3.4 nm^{-1} respectively. Using the values for k_0 and Eq. (5.14) and accounting for spin degeneracy, the height of the step function for monolayer GaS, GaSe, InS and InSe is 4.1 nm^{-1}, 3.4 nm^{-1}, 5.1 nm^{-1} and 3.2 nm^{-1}. The height of the numerically calculated density of modes in GaS decreases by $\sim 30\%$ when the film thickness increases from one to four monolayers, and the value of k_0 decreases by $\sim 38\%$. The height of the step function using Eq. (5.14) and k_0 is either underestimated or equivalent to the numerical density of modes. For all four materials GaS, GaSe, InS and InSe, decreasing the film thickness increases k_0 and the height of the step-function of the band-edge density of modes. A larger band-edge density of modes gives a larger power factor and ZT compared to that of the bulk.

The p-type Seebeck coefficients, the p-type and n-type power factors, and the thermoelectric figures-of-merit (ZT) as functions of carrier concentration at room temperature for GaS, GaSe, InS and InSe are shown in Figure 5.5. The thermoelectric parameters at $T = 300$ K of bulk and one to four monolayers of GaS, GaSe, InS and InSe are summarized in Tables 5.5 - 5.12. For each material the peak p-type ZT occurs at a monolayer thickness. The largest room temperature p-type ZT occurs in monolayer InS. At room temperature, the peak p-type (n-type) ZT values in 1L, 2L, 3L and 4L GaS occur when the Fermi level is 42 meV, 38 meV, 34 meV and 30 meV (22 meV, 17 meV, 11 meV, and 7 meV) above (below) the valence (conduction) band edge, and the Fermi level positions in GaSe, InS and InSe change in qualitatively the same way. The p-type hole concentrations of monolayer GaS, GaSe, InS and InSe at the peak ZT are enhanced by factors of 9.7, 10.8, 7.2 and 5.5 compared to those of their respective bulk structures. At the peak p-type room-temperature ZT, the Seebeck coefficients of monolayer GaS, GaSe, InS and InSe are enhanced by factors of 1.3, 1.4, 1.3, and 1.3, respectively, compared to their bulk values. However, the monolayer and bulk peak ZT values occur at carrier concentrations that differ by an order of magnitude. At a fixed carrier concentration, the monolayer Seebeck coefficients are approximately 1.4 times larger than the bulk Seebeck coefficients. The p-type power factor (PF) at the peak ZT for 1L GaS is enhanced by a factor of 17 compared to that of bulk GaS. Assuming a constant κ_l for the bulk and few-layer structures, the p-type ZT values of monolayer GaS, GaSe, InS and InSe are enhanced by factors of 14.3, 16.9, 8.7 and 7.7, respectively, compared to their bulk values. At the peak p-type ZT, the contribution of κ_e to κ_{tot} is minimum for the bulk structure and maximum for the monolayer structure. The contributions of κ_e to κ_{tot} in bulk and monolayer GaS are 5% and 24%, respectively. The increasing contribution of κ_e to κ_{tot} with decreasing film thickness reduces the enhancement of ZT relative to that

t	p (10^{19}cm^{-3})	S_p $(\mu V K^{-1})$	σ_p $(10^6\Omega m)^{-1}$	ZT_p
1L	3.2	251.6	1.41	2.01 (1.42)
2L	1.5	222.9	.776	1.02 (.641)
3L	1.1	213.2	.530	.630 (.412)
4L	.92	211.2	.390	.421 (.290)
Bulk	.33	187.6	.149	.140

Table 5.5: GaS thermoelectric properties for bulk and one to four monolayers at $T = 300$ K. Hole carrier concentrations (p), Seebeck coefficients (S_p), and electrical conductivties (σ_p) at the peak p-type ZT. The maximum and minimum ZT is listed for two different approximations of κ_l, the minimum ZT is listed in parentheses. The thermoelectric parameters are computed using an electron and hole mean free path, λ=25 nm and a lattice thermal conductivity, κ_l, of 10 Wm^{-1}K^{-1} for the maximum ZT and 20 Wm^{-1}K^{-1} for the minimum ZT.

of the power factor.

The increases in the Seebeck coefficients, the charge densities, and the electrical conductivities with decreases in the film thicknesses follow the increases in the magnitudes of I_0 and I_1 as discussed at the end of Sec. 5.2.2. For bulk p-type GaS, the values of I_0 (I_1) at peak ZT are 0.94 (1.85), and for monolayer GaS, they are 8.87 (23.4). They increase by factors of 9.4 (12.6) as the film thickness decreases from bulk to monolayer. In 4L GaS, the values of I_0 (I_1) are 2.45 (5.38), and they increase by factors of 3.6 (5.4) as the thickness is reduced from 4L to 1L. For all four of the III-VI compounds, the increases in I_1 are larger than the increases in I_0 as the film thicknesses decrease. As described in Sec. 5.2.2, these increases are driven by the transformation of the dispersion from parabolic to Mexican hat with an increasing radius of the band edge k-space ring as the thickness is reduced from bulk to monolayer.

t	n	$\lvert$—S_e $\rvert$	σ_e	ZT_e
	$(10^{19}$ cm$^{-3})$	$(\mu V K^{-1})$	$(10^6 \Omega m)^{-1}$	
1L	1.02	237.0	.35	.431 (.620)
2L	.621	219.6	.23	.218 (.362)
3L	.595	200.9	.21	.147 (.273)
4L	.545	191.9	.20	.111 (.231)
Bulk	.374	210.8	.12	.095

Table 5.6: GaS thermoelectric properties for bulk and one to four monolayers at $T = 300$ K. Electron carrier concentrations (n), Seebeck coefficients (S_e), and electrical conductivties (σ_n) at the peak n-type ZT. The maximum and minimum ZT is listed for two different approximations of κ_l, the minimum ZT is listed in parentheses. The thermoelectric parameters are computed using an electron and hole mean free path, λ=25 nm and a lattice thermal conductivity, κ_l, of 10 Wm^{-1}K^{-1} for the maximum ZT and 20 Wm^{-1}K^{-1} for the minimum ZT.

t	p	S_p	σ_p	ZT_p
	$(10^{18}$cm$^{-3})$	$(\mu V K^{-1})$	$(\Omega m)^{-1}$	
1L	5.8	256.1	1.28	1.86 (1.07)
2L	2.7	225.3	.711	.870 (.471)
3L	2.1	221.2	.450	.561 (.293)
4L	1.4	210.2	.352	.391 (.211)
Bulk	.54	180.9	.121	.112

Table 5.7: GaSe thermoelectric properties for bulk and one to four monolayers at 300K. Hole carrier concentrations (p), Seebeck coefficients (S_p), and electrical conductivties (σ_p) at the peak p-type ZT. The maximum and minimum ZT is listed for two different approximations of κ_l, the minimum ZT is listed in parentheses. The minimum value of ZT uses twice the value of κ_l reported for bulk GaSe.

Thickness	n	$|-S_e|$	σ_e	ZT_e
	$(10^{18}$ cm$^{-3})$	$(\mu V K^{-1})$	$(10^6 \Omega m)^{-1}$	
1L	2.71	202.9	.310	.321 (.172)
2L	1.20	201.4	.152	.162 (.081)
3L	.79	194.0	.103	.110 (.054)
4L	.69	186.4	.085	.082 (.041)
Bulk	.29	127.9	.033	.132

Table 5.8: GaSe thermoelectric properties for bulk and one to four monolayers at 300K. Electron carrier concentrations (n), Seebeck coefficients (S_e), and electrical conductivties (σ_n) at the peak n-type ZT. The maximum and minimum ZT is listed for two different approximations of κ_l, the minimum ZT is listed in parentheses. The thermoelectric parameters are computed using an electron and hole mean free path, λ=25 nm and a lattice thermal conductivity, κ_l, of 10 Wm^{-1}K^{-1} for the maximum ZT and 20 Wm^{-1}K^{-1} for the minimum ZT.

While the focus of the paper is on the effect of the Mexican hat dispersion that forms in the valence band of these materials, the n-type thermoelectric figure of merit also increases as the film thickness is reduced to a few layers, and it is also maximum at monolayer thickness. The room temperature, monolayer, n-type thermoelectric figures of merit of GaS, GaSe, InS and InSe are enhanced by factors of 4.5, 2.4, 3.8 and 5.3, respectively, compared to the those of the respective bulk structures. The largest n-type ZT occurs in monolayer GaS. In a GaS monolayer, the 3-fold degenerate M valleys form the conduction band edge. This large valley degeneracy gives GaS the largest n-type ZT among the 4 III-VI compounds. As the GaS film thickness increases from a monolayer to a bilayer, the conduction band edge moves to the non-degenerate Γ valley so that the number of low-energy states near the conduction band edge decreases. With an added third and fourth layer, the M valleys move higher, and the Γ valley continues to split so that the number of low-energy conduction states does not increase with film thickness. Thus, for a Fermi energy fixed slightly below the band edge, the electron density and the conductivity decrease as the number of

t	p (10^{18}cm^{-3})	S_p $(\mu V K^{-1})$	σ_p $(10^6 \Omega m)^{-1}$	ZT_p
1L	9.3	244.2	1.26	2.43 (1.38)
2L	4.2	228.7	.610	1.12 (.612)
3L	2.3	229.5	.361	.701 (.383)
4L	1.9	222.0	.292	.532 (.281)
Bulk	1.3	195.1	.180	.280

Table 5.9: InS thermoelectric properties for bulk and one to four monolayers at $T = 300$ K. Hole carrier concentrations (p), Seebeck coefficients (S_p), and electrical conductivties (σ_p) at the peak p-type ZT. The maximum and minimum ZT is listed for two different approximations of κ_l, the minimum ZT is listed in parentheses. The minimum value of ZT uses twice the value of κ_l reported for bulk InS.

layers increase as shown in Tables 5.5 - 5.12. As a result, the maximum n-type ZT for each material occurs at a single monolayer and decreases with each additional layer.

5.3.2 Bi_2Se_3

Bi_2Se_3 is an iso-structural compound of the well known thermoelectric, Bi_2Te_3. Both materials have been intensely studied recently because they are also topological insulators. [194,195] Bulk Bi_2Se_3 has been studied less for its thermoelectric properties due to its slightly higher thermal conductivity compared to Bi_2Te_3. The bulk thermal conductivity of Bi_2Se_3 is 2 W-$(mK)^{-1}$ compared to a bulk thermal conductivity of 1.5 W-$(mK)^{-1}$ reported for Bi_2Te_3. [68,188] However, the thermoelectric performance of bulk Bi_2Te_3 is limited to a narrow temperature window around room temperature because of its small bulk band gap of approximately 160 meV. [194] The band gap of single quintuple layer (QL) Bi_2Te_3 was previously calculated to be 190 meV. [70] In contrast, the bulk bandgap of Bi_2Se_3 is ∼300 meV [196] which allows it to be utilized

t	n	$|-S_e|$	σ_e	ZT_e
	$(10^{18}\ cm^{-3})$	$(\mu V K^{-1})$	$(10^6 \Omega m)^{-1}$	
1L	3.7	210.8	.210	.350 (.191)
2L	1.6	200.0	.113	.181 (.093)
3L	1.3	196.9	.078	.120 (.062)
4L	1.0	198.1	.059	.094 (.048)
Bulk	1.2	179.8	.070	.092

Table 5.10: InS thermoelectric properties for bulk and one to four monolayers at $T = 300$ K. Electron carrier concentrations (n), Seebeck coefficients (S_e), and electrical conductivties (σ_n) at the peak n-type ZT. The maximum and minimum ZT is listed for two different approximations of κ_l, the minimum ZT is listed in parentheses. The minimum value of ZT uses twice the value of κ_l reported for bulk InS.

t	p	S_p	σ_p	ZT_p
	$(10^{18} cm^{-3})$	$(\mu V K^{-1})$	$(10^6 \Omega m)^{-1}$	
1L	9.7	229.8	.981	1.08 (.592)
2L	4.0	219.8	.430	.471 (.251)
3L	4.2	204.2	.471	.292 (.150)
4L	2.4	201.0	.261	.252 (.131)
Bulk	1.8	179.1	.181	.142

Table 5.11: InSe thermoelectric properties for bulk and one to four monolayers at $T = 300$ K. Hole carrier concentrations (p), Seebeck coefficients (S_p), and electrical conductivties (σ_p) at the peak p-type ZT. The maximum and minimum ZT is listed for two different approximations of κ_l, the minimum ZT is listed in parentheses. The minimum value of ZT uses twice the value of κ_l reported for bulk InSe.

Thickness	n	$\lvert -S_e \rvert$	σ_e	ZT_e
	(10^{18} cm^{-3})	$(\mu V K^{-1})$	$(10^6 \Omega m)^{-1}$	
1L	2.34	200.5	.192	.180 (.092)
2L	1.22	194.7	.111	.090 (.046)
3L	.781	189.1	.067	.059 (.029)
4L	.610	186.8	.053	.045 (.023)
Bulk	.652	160.9	.054	.034

Table 5.12: InSe thermoelectric properties for bulk and one to four monolayers at $T = 300$ K. Electron carrier concentrations (n), Seebeck coefficients (S_e), and electrical conductivties (σ_n) at the peak n-type ZT. The maximum and minimum ZT is listed for two different approximations of κ_l, the minimum ZT is listed in parentheses. The thermoelectric parameters are computed using an electron and hole mean free path, λ=25 nm and a lattice thermal conductivity, κ_l, of 12 Wm^{-1}K^{-1} for the maximum ZT and 24 Wm^{-1}K^{-1} for the minimum ZT.

at higher temperatures.
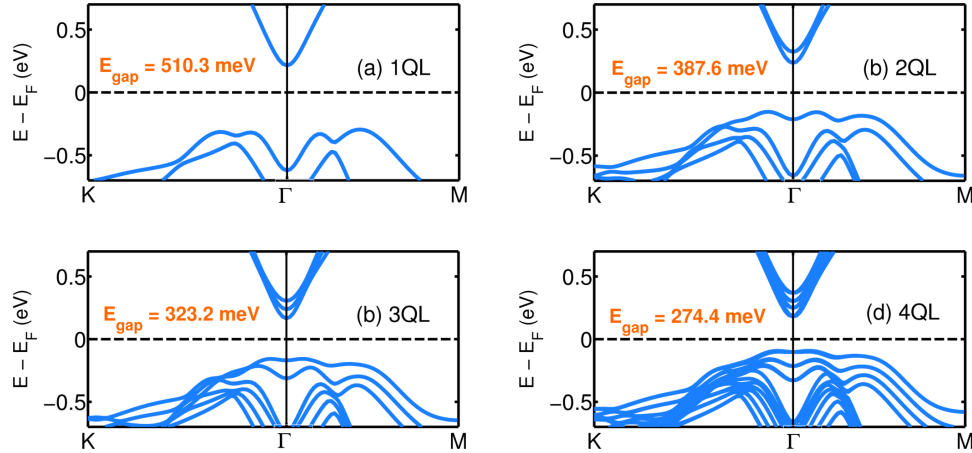
Figure 5.6: (Color online) Ab-initio band structure including spin-orbit interaction of Bi$_2$Se$_3$: (a) 1 QL, (b) 2 QL, (c) 3 QL and (d) 4 QL.

The optimized lattice parameters for bulk Bi$_2$Se$_3$ are listed in Table 5.1. The optimized bulk crystal structure and bulk band gap is consistent with prior experimental and theoretical studies of bulk Bi$_2$Se$_3$. [11, 146] Using the optimized lattice parameters of the bulk structure, the electronic structures of one to four quintuple

layers of Bi_2Se_3 are calculated with the inclusion of spin-orbit coupling. The electronic structures of 1 to 4 QLs of Bi_2Se_3 are shown in Figure 5.6. The band gaps for one to four quintuple layers of Bi_2Se_3 are 510 meV, 388 meV, 323 meV and 274 meV for the 1QL, 2QL, 3QL and 4QL films, respectively. The presence of a gapped surface state in few-layer Bi_2Se_3 has been observed in prior experiments up to 4 QLs [197] and is consistent with the presence of a gapped state in ab-initio calculations up to 6QLs. [146, 198].

The effective masses of the conduction and valence band at Γ for 1QL to 4QL of Bi_2Se_3 are listed in Table 5.13. For each of the thin film structures, the conduction bands are parabolic and located at Γ. The conduction band at Γ of the 1QL structure is composed of 13% Se s, 24% Se p_{xy}, 16% Bi p_{xy}, and 39% Bi p_z. The orbital composition of the Γ valley remains qualitatively the same as the film thickness increases to 4QL. The orbital composition of the bulk conduction band is 79% Se p_z and 16% Bi s. As the film thickness increases above 1QL, the conduction band at Γ splits, as illustrated in Figs. 5.6(b)-(d). In the 2QL, 3QL and 4QL structures the conduction band splitting varies between 53.9 meV and 88.2 meV. As with the III-VIs, the number of low-energy conduction band states per unit thickness decreases with increasing thickness.

The valence bands have slightly anistropic Mexican hat dispersions. The values of ϵ_0 and k_0 used to characterize the Mexican hat for the 1QL to 4QL structures of Bi_2Se_3 are listed in Table 5.4. The radius k_0 is the distance from Γ_v to the band extremum along $\Gamma_v - M_v$, which is the valence band maxima for the 1QL to 4QL structures. The energy difference between the valence band maxima and the band extremum along $\Gamma_v - K_v$ decreases from 19.2 meV to 0.56 meV as the film thickness increases from 1QL to 4QL. The Mexican hat dispersion in 1QL of Bi_2Se_3 is better described as a double brimmed hat consisting of two concentric rings in k-space characterized by

four points of extrema that are nearly degenerate. The band extremum along $\Gamma_v - M_v$ adjacent to the valence band maxima, is 36 meV below the valence band maxima. Along $\Gamma_v - K_v$ the energy difference between the two band extrema is 4.2 meV. At Γ_v, the orbital composition of the valence band for 1QL of Bi_2Se_3 is 63% p_z orbitals of Se, 11% p_{xy} orbitals of Se and 18% s orbitals of Bi, and the orbital composition remains qualitatively the same as the film thickness increases to 4QL. As the thickness increases above a monolayer, the energy splitting of the valence bands from each layer is large with respect to room temperature k_BT and more complex than the splitting seen in the III-VIs. At a bilayer, the highest valence band loses most of the outer k-space ring, the radius k_0 decreases by a factor 3.1 and the height (ε_0) of the hat decreases by a factor of 5.1. This decrease translates into a decrease in the initial step height of the density of modes shown in Figure 5.7(a). The second highest valence band retains most of the shape of the original monolayer valence band, but it is now too far from the valence band edge to contribute to the low-energy electronic or thermoelectric properties. Thus, Bi_2Se_3 follows the same trends as seen in Bi_2Te_3; the large enhancement in the thermoelectric properties resulting from bandstructure are only significant for a monolayer [45].

Structure	Γ_v (m_0)	Γ_c (m_0)
1L	0.128	0.132
2L	0.436	0.115
3L	1.435	0.176
4L	1.853	0.126

Table 5.13: Ab-initio calculations of the hole and electron effective masses at the Γ-valley valence and conduction band edges of Bi_2Se_2.

The p-type and n-type Seebeck coefficient, electrical conductivity, power factor and the thermoelectric figure-of-merit (ZT) as a function of carrier concentration at room temperature for Bi_2Se_3 are illustrated in Figure 5.7. The thermoelectric

t	p	S_p	σ_p	ZT_p
	(10^{18}cm^{-3})	$(\mu V K^{-1})$	$(10^6 \Omega m)^{-1}$	
1L	7.7	279.3	.321	2.62 (1.76)
2L	4.6	251.3	.245	1.07 (.691)
3L	2.8	259.4	.152	.791 (.622)
4L	2.6	237.8	.141	.624 (.561)
Bulk	1.9	210.7	.085	.610

Table 5.14: Bi_2Se_3 thermoelectric properties for bulk and one to four quintuple layers at $T = 300$ K. Hole carrier concentrations (p), Seebeck coefficients (S_p), and electrical conductivties (σ_p) at the peak p-type ZT. The maximum and minimum ZT is listed for two different approximations of κ_l, the minimum ZT is listed in parentheses. The minimum value of ZT uses twice the value of κ_l reported for bulk Bi_2Se_3.

t	n	$|\text{—}S_e|$	σ_e	ZT_e
	$(10^{18} \text{ cm}^{-3})$	$(\mu V K^{-1})$	$(10^6 \Omega m)^{-1}$	
1L	4.6	210.1	.112	.463 (.249)
2L	3.4	208.2	.081	.280 (.182)
3L	2.9	198.3	.071	.218 (.120)
4L	2.6	185.8	.062	.176 (.081)
Bulk	1.2	191.9	.033	.129

Table 5.15: Bi_2Se_3 thermoelectric properties for bulk and one to four quintuple layers at $T = 300$ K. Electron carrier concentrations (n), Seebeck coefficients (S_e), and electrical conductivties (σ_n) at the peak n-type ZT. The maximum and minimum ZT is listed for two different approximations of κ_l, the minimum ZT is listed in parentheses. The minimum value of ZT uses twice the value of κ_l reported for bulk Bi_2Se_3.
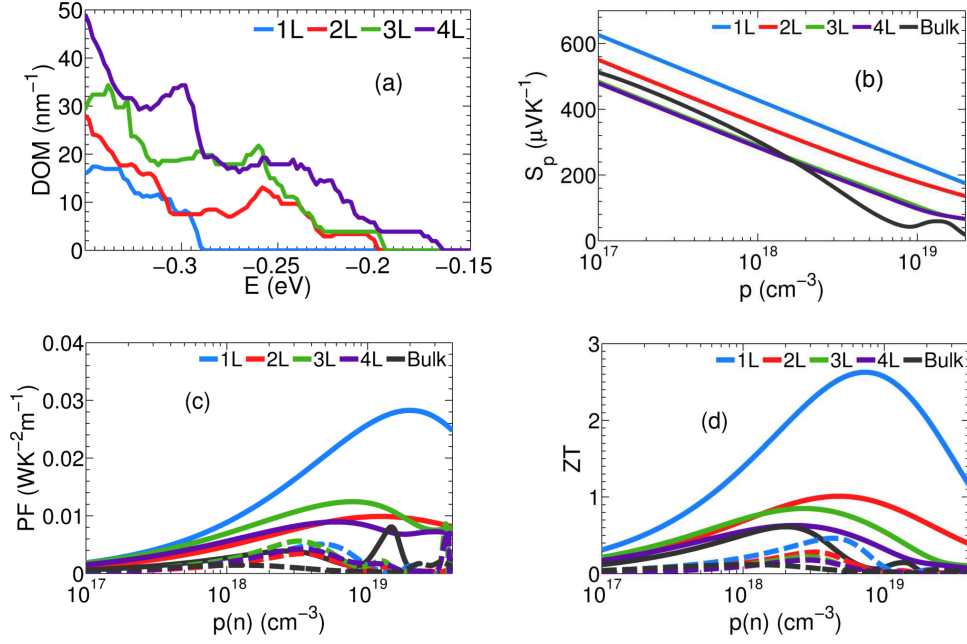
Figure 5.7: (Color online) (a) Distribution of modes per unit width versus energy for Bi_2Se_3. The midgap energy is set to E=0. Thermoelectric properties of p-type (solid line) and n-type (broken line) Bi_2Se_3: (b) Seebeck coefficient, (c) power factor and (d) thermoelectric figure-of-merit, ZT, at room temperature for 1L (blue), 2L (red), 3L (green), 4L (purple) and bulk (black)

parameters at $T = 300$ K of bulk and one to four quintuple layers for Bi_2Se_3 are summarized in Table 5.14 and. 5.15.

Assuming the same κ_l for the bulk and single quintuple layer structure, the p-type ZT for the single quintuple layer is enhanced by a factor of 4.3 compared to that of the bulk film. At the peak ZT, the hole concentration is 4 times larger than that of the bulk, and the position of the Fermi energy with respect to the valence band edge $(E_F - E_V)$ is 45 meV higher than that of the bulk. The bulk and monolayer magnitudes of I_0 (I_1) are 0.77 (1.87) and 3.01 (9.72), respectively, giving increases of 3.9 (5.2) as the thickness is reduced from bulk to monolayer. As the film thickness is reduced from 4 QL to 1 QL, the magnitudes of I_0 and I_1 at the peak ZT increase by factors of 2.4 and 2.8, respectively.

The peak room temperature n-type ZT also occurs for 1QL of Bi_2Se_3. In one to four quintuple layers of Bi_2Se_3, two degenerate bands at Γ contribute to the conduction band density of modes. The higher Γ valleys contribute little to the conductivity as the film thickness increases. The Fermi levels at the peak n-type, room-temperature ZT rise from 34 meV to 12 meV below the conduction band edge as the film thickness increases from 1 QL to 4 QL while the electron density decreases by a factor of 1.8. This results in a maximum n-type ZT for the 1QL structure.

There have been several prior studies of the thermoelectric properties of single and few quintuple layer Bi_2Se_3, and it is useful to make comparisons to understand the differences and similarities. Saeed et al. [146] calculated a p-type ZT value of 0.27 and a p-type peak power factor of 0.432 $mWm^{-1}K^{-2}$ for 1QL of Bi_2Se_3 using ab initio band structure, a hole relaxation time of 2.7 fs, and a thermal conductivity of 0.49 W/mK. The disparity between their values and ours result from the different approximations made for the relaxation time (2.7 fs) and lattice thermal conductivity (0.49 W/mK). To reproduce their results, we convert the relaxation time of 2.7 fs into a mean free path of 0.27 nm, using an average thermal velocity of 10^5 m/s determined from the 1QL valence bandstructure. This hole mean free path is approximately 2/3 of the in-plane lattice constant which pushes the limits of validity of the semiclassical Boltzmann transport approach. Using the hole mean free path of 0.27 nm and the lattice thermal conductivity of 0.49 W/mK, our calculation gives a peak p-type ZT of 0.28 and peak p-type power factor of 0.302 $mWm^{-1}K^{-2}$, which agrees well with the results in Ref. [146].

5.3.3 Bilayer Graphene

AB stacked bilayer graphene (BLG) is a gapless semiconductor with parabolic conduction and valence bands that are located at the K (K') symmetry points. Prior experimental [132, 199] and theoretical [147] studies demonstrated the formation of a bandgap in BLG with the application of a vertical electric field. The vertical electric field also deforms the conduction and valence band edges at K into a Mexican-hat dispersion [128, 132]. Using ab-initio calculations we compute the band structure of bilayer graphene subject to vertical electric fields ranging from 0.1 V/nm to 1 V/nm. The lattice parameters for the bilayer graphene structure used in our simulation are given in Table 5.1. The ab-initio calculated band gaps are in good agreement with prior calculations. [147, 200] The bandgap increases from 31.4 meV to 223.1 meV as the applied field increases from 0.1 V/nm to 1 V/nm.

For each applied field ranging from 0.1 V/nm to 1 V/nm both the valence band and the conduction band edges lie along the path $\Gamma - K$, and the radius k_0 is the distance from K to the band edge along $\Gamma - K$. The magnitude of k_0 increases approximately linearly with the electric field as shown in Figure 5.8(a). The dispersions of the valence band and the conduction band quantitatively differ, and k_0 of the valence band is up to 10% larger than k_0 of the conduction band. The anisotropy of the conduction and valence Mexican hat dispersions increase with increasing vertical field. The extremum point along $K - M$ of the valence (conduction) band Mexican hat dispersion is lower (higher) in energy compared to the band extremum along $\Gamma - K$. As the field increases from 0.1 V/nm to 1.0 V/nm the energy difference between the two extrema points increases from 1.2 meV to 21.6 meV in the valence band and 3.7 meV to 30.1 meV in the conduction band. This anisotropy in the Mexican hat of the valence and conduction band leads to a finite slope in the density of modes illustrated in Figure

Field (V/nm)	p ($\times 10^{12}$ cm^{-2})	S_p ($\mu V K^{-1}$)	σ_p ($\times 10^7 \Omega m)^{-1}$)	ZT$_p$
0.0	.06	73.4	.53	.0108
0.2	.07	148.6	.69	.0161
0.4	.08	152.6	.73	.0221
0.6	.12	159.4	.83	.0271
0.8	.14	179.1	.94	.0275
1.0	.16	192.1	1.1	.0281

Table 5.16: Bilayer graphene p-type thermoelectric properties as a function of vertical electric field at $T = 300$ K. Hole carrier concentrations, p-type Seebeck coefficient, and electrical conductivity at the peak p-type ZT.

5.8(b).

As the applied field is increased from 0.1 V/nm to 1.0 V/nm the height of the density of modes step function in the valence and conduction band increases by a factor of 2.6 as illustrated in Fig. 5.8(b). Even though the bandgap increases with bias, at a fixed Fermi level, the charge density also increases with bias. For Fermi energies within the bandgap, the energy per carrier, with respect to the Fermi energy, also increases resulting in an increase in the Seebeck coefficient shown in Fig. 5.8(c). The increase in the Seebeck coefficient and the charge density lead to the increase in ZT shown in Fig. 5.8(d). For an applied electric field of 1 V/nm the p-type and n-type ZT is enhanced by a factor of 2.8 and 2.6 in bilayer graphene compared to the ZT of bilayer graphene with no applied electric field. The p-type thermoelectric parameters of bilayer graphene subject to vertical electric fields ranging from 0.0 V/nm to 1.0 V/nm are summarized in Table 5.16. The p-type and n-type thermoelectric parameters are similar.
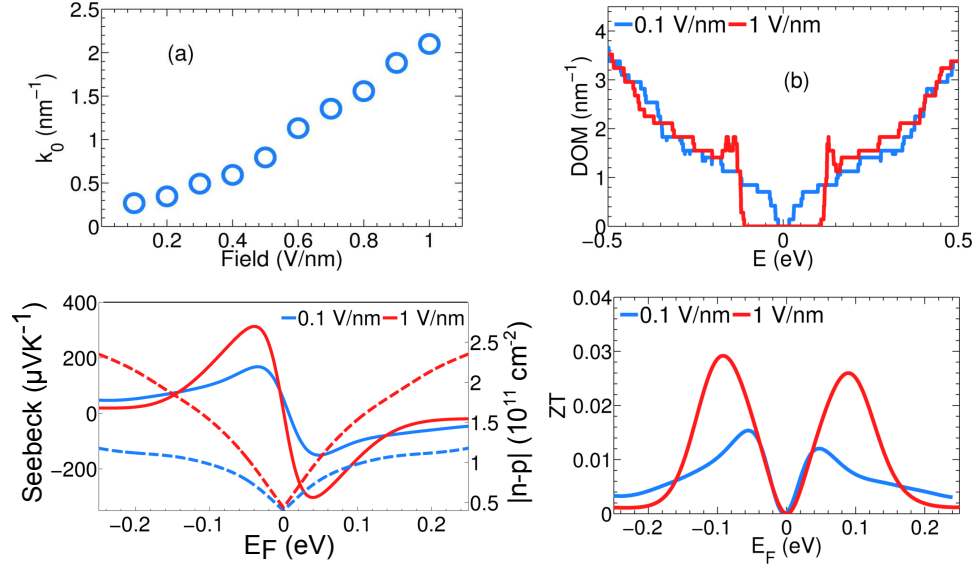
Figure 5.8: (Color online) (a) Evolution of the radius k_0 of the Mexican hat in bilayer graphene as a function of an applied vertical electric field. (b) Density of modes per unit width for two different vertical fields of 0.1 V/nm (blue) and 1 V/nm (red). (c) Seebeck coefficients (solid lines) and carrier concentrations (broken lines) for two different vertical fields. (d) ZT of bilayer graphene as a function of the Fermi level for two different vertical fields.

5.3.4 Bi Monolayer

The large spin-orbit interaction in bismuth leads to a Rasha-split dispersion of the valence band in a single monolayer of bismuth. The lattice parameters for the Bi(111) monolayer used for the SOC ab-initio calculations are summarized in Table 5.1. The bandgap of the bismuth monolayer is 503 meV with the conduction band at Γ_c. The inclusion of spin-orbit interaction splits the two degenerate bands at Γ_v by 79 meV and deforms the valence band maxima into a Rashba split band. The calculated band structure of the Bi(111) monolayer is shown in Figure 5.9(a,b). The Rashba parameter for the bismuth monolayer is extracted from the ab-initio calculated band structure. The curvature of the valence band maxima of the Rashba band gives an effective mass of $m^* = 0.135$. The effective mass of the conduction band at Γ_c is $m^* = 0.008$. The vertical splitting of the bands at small k gives an $\alpha_R = 2.14$ eVÅ.
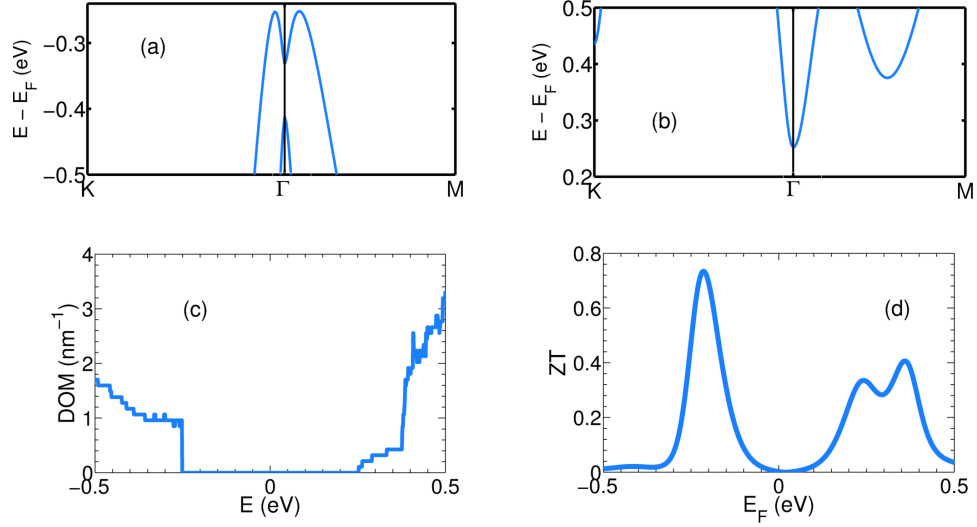
Figure 5.9: (Color online) Electronic structure and thermoelectric properties of Bi(111) monolayer. (a) Valence band, (b) Conduction band of Bi(111) monolayer with spin-orbit interaction. (c) Density of modes with SOC interactions included, (c) Thermoelectric figure of merit, ZT, at room temperature.

Prior experimental and theoretical studies on the strength of the Rashba interaction in Bi(111) surfaces demonstrate α_R values ranging from 0.55 eVÅ^{-1} to 3.05 eVÅ^{-1}. [177] A slight asymmetry in the Rashba-split dispersion leads to the valence band maxima lying along $\Gamma_v - M_v$. The band extremum along $\Gamma_v - K_v$ is 0.5 meV below the valence band maxima. The radius of the valence band-edge k_0, which is the distance from Γ_v to the band extremum along $\Gamma_v - M_v$ is 1.40 nm^{-1} similar to 4L InSe. The valence band-edge density of modes shown in Fig. 5.9(c) is a step function with a peak height of 0.96 nm^{-1}. Figure 5.9(d) shows the resulting thermoelectric figure of merit ZT as a function of Fermi level position at room temperature. The thermoelectric parameters at $T = 300$ K are summarized in Table 5.17.

There is one prior study of the thermoelectric performance of monolayer Bi. [187] In this study Cheng et. al calculate a p-type (n-type) ZT of 2.4 (2.1), a peak p-type (n-type) Seebeck coefficient of 800 μV/K (-780 μV/K) using a lattice thermal conductivity of 3.9 Wm^{-1}K^{-1} and a relaxation time of 0.148 ps. We convert the

	p-type	n-type
n/p ($\times 10^{19}$cm^{-3})	.61	.35
Seebeck ($\mu V K^{-1}$)	239.7	234.1
σ ($\times 10^6 \Omega m)^{-1}$)	.19	.089
ZT	.73	.41

Table 5.17: Bi(111) thermoelectric properties at $T = 300$ K. Hole and electron carrier concentrations (p and n), Seebeck coefficients (S$_p$ and S$_e$), and electrical conductivties (σ_p and σ_n) at the peak p-type and n-type ZT.

relaxation time of 0.148 ps into an electron mean free path of 59.2 nm and a hole mean free path of 14.8nm using average electron and hole thermal velocities of 4×10^5 m/s and 1×10^5, respectively, determined from the Bi(111) monolayer bandstructure. With these values for λ and a lattice thermal conductivity of 3.9 Wm^{-1}K^{-1}, our calculation gives a peak p-type (n-type) ZT and Seebeck values of 1.9 (1.8) and 786 μV/K (-710 μV/K) respectively, which agrees well with the results in Ref. [187]

5.4 Summary and Conclusions

Monolayer and few-layer structures of III-VI materials (GaS, GaSe, InS, InSe), Bi$_2$Se$_3$, monolayer Bi, and biased bilayer graphene all have a valence band that forms a ring in k-space. For monolayer Bi, the ring results from Rashba splitting of the spins. All of the other few-layer materials have valence bands in the shape of a 'Mexican hat.' For both cases, a band-edge that forms a ring in k-space is highly degenerate. It coincides with a singularity in the density of states and a near step-function turn-on of the density of modes at the band edge. The height of the step function is approximately proportional to the radius of the k-space ring.

As the radius of the k-space ring increases, the Fermi level at the maximum power factor or ZT moves higher into the bandgap away from the valence band edge. Nev-

ertheless, the hole concentration increases. The average energy carried by a hole with respect to the Fermi energy increases. As a result, the Seebeck coefficient increases. The dispersion with the largest radius coincides with the maximum power factor provided that the mean free paths are not too different. For the materials and parameters considered here, the dispersion with the largest radius also results in the largest ZT at room temperature.

The Mexican hat dispersion in the valence band of the III-VI materials exists for few-layer geometries, and it is most prominent for monolayers, which have the largest radius k_0 and the largest height ε_0. The existence of the Mexican hat dispersions and their qualitative features do not depend on the choice of functional, stacking, or the inclusion or omission of spin-orbit coupling, and recent calculations by others show that they are also unaffected by many-electron self-energy effects. [139] At a thickness of 8 layers, all of the III-VI valence band dispersions are parabolic.

The Mexican hat dispersion in the valence band of monolayer Bi_2Se_3 is qualitatively different from those in the monolayer III-VIs. It can be better described as a double-brimmed hat characterized by 4 points of extrema that lie within $\sim k_B T$ of each other at room temperature. Futhermore, when two layers are brought together to form a bilayer, the energy splitting of the two valence bands in each layer causes the highest band to lose most of its outer ring causing a large decrease in the density of modes and reduction in the thermoelectric properties. These trends also apply to Bi_2Te_3. [45]

With the exception of monolayer GaS, the conduction bands of few-layer n-type III-VI and Bi_2Se_3 compounds are at Γ with a significant p_z orbital component. In bilayers and multilayers, these bands couple and split pushing the added bands to higher energy above the thermal transport window. Thus, the number of low-energy states per layer is maximum for a monolayer. In monolayer GaS, the conduction band

is at M with 3-fold valley degeneracy. At thicknesses greater than a monolayer, the GaS conduction band is at Γ, the valley degeneracy is one, and the same splitting of the bands occurs as described above. Thus, the number of low-energy states per layer is also maximum for monolayer GaS. This results in maximum values for the n-type Seebeck coefficients, power factors, and ZTs at monolayer thicknesses for all of these materials.

For the chalcogenide materials where an inverted Mexican hat occurs in the valence band, the p-type ZT is enhanced by up to a factor of $\sim$17 over the ZT of the bulk giving a maximum value of ZT = 2.9 in Bi_2Se_3 and ZT = 2.4 in InS. Similar n-type values were found for few-layer transition metal dichalcogenides such as bilayer $MoSe_2$ [1]. A combination of these materials would provide an on-chip thermocouple for local thermal management or power scavanging. Bilayer graphene may serve as a test-bed to measure the predicted thermoelectric effects, since a cross-plane electric field linearly increases the diameter of the Mexican hat ring, and the features of the Mexican hat in bilayer graphene have recently been experimentally observed. [132]

Chapter 6

Charge density waves in transition metal dichalcogenides

6.1 Introduction and Motivation

A number of Group IV and Group V transition metal dichalcogenides exhibit a phase transition to a charge density wave (CDW) ground state. [15, 46] Below a transition temperature that is unique to each material a phase transition from a normal metallic state to a charge density wave state occurs. In reality, the the phase diagrams of the CDW transition that occurs in the TMD materials as a function of temperature is complex, with a number of intermediate phase transitions that can occur to either an incommensurate CDW (ICDW) or nearly-commensurate CDW (NCCDW) state. Summarized in Table 6.1 below are the transition temperatures and structural properties for a select number of transition metal dichalcogenides that undergo a CDW transition.

Although the charge density wave phenomena in bulk transition metal dichalcogenides have been studied extensively the ability to isolate single monolayers and

	1T-TaS$_2$	1T-TaSe$_2$	2H-TaSe$_2$	1T-TiSe$_2$
Transition Temperature				
T$_{ICDW}$ (K)	550	600	122	-
T$_{NCCDW}$ (K)	350	-	-	-
T$_{CCDW}$ (K)	180	473	90	200
Lattice distortion	$\sqrt{13} \times \sqrt{13}$	$\sqrt{13} \times \sqrt{13}$	$3 \times 3 \times 3$	$2 \times 2 \times 2$
Lattice constants				
a ($\mathring{A}$)	3.365	3.48	3.450	3.536
c ($\mathring{A}$)	5.883	6.27	13.057	6.004

Table 6.1: Experimental charge density wave properties of Group IV and Group V transition metal dichalcogenides obtained from Refs. [13–15]

few-monolayer films of the materials listed in Table 6.1 has motivated the study of charge density wave properties in their monolayer and few-layer structures. The objectives of this study are to:

1. Understand how the electronic structure of 1T-TiSe$_2$ and 1T-TaS$_2$ changes as they are confined to a single monolayer

2. Calculate the zone center phonons of 1T-TaSe$_2$ in its bulk, monolayer and few-layer structures in the normal and commensurate CDW phase. Relate these changes in the vibrational properties as a function of film thickness to experimental data.

The results of this study for each material is detailed in separate subsections below. The materials we study in this chapter include 1T-TaS$_2$, 1T-TaSe$_2$ and 1T-TiSe$_2$. in their bulk, few-layer and monolayer structures.

6.2   1T-TaSe$_2$

TaSe$_2$ can exist in many different polymorphs and polytypes; the 1T, 2H and 3R. In 1T-TaSe$_2$ as the temperature is lowered below T$_{IC}$=600 K, bulk 1T-TaSe2 transforms into the ICDW phase. Decreasing the temperature below T$_C$=473 K results in the first order phase transition to the C-CDW phase. During the ICDW to CCDW phase transition, the CDW supercell undergoes a $\sqrt{13} \times \sqrt{13}$ reconstruction in which the basal-plane lattice vectors increase by $\sqrt{13}$ and rotate by 13.9^o with respect to the original lattice vectors. Since there are strong modifications of the lattice as a function of temperature this results in strong modifications of the Raman spectra of 1T-TaSe$_2$. Illustrated in Figure 6.1 is the Raman spectra measured for 150 nm and 35 nm thick films of 1T-TaSe$_2$ over a range of temperatures. To understand the modification of the Raman spectra as a function of temperature ab-initio calculations of the bulk and monolayer structures of 1T-TaSe$_2$ in the normal and CCDW phase are done.

6.2.1   Computational Methods

The electronic properties of these materials are studied using density functional theory and the vibrational properties are studied using density functional perturbation theory. The calculations included DFT using the projector augmented wave method as implemented in the software package VASP and DFPT as implemented in the Quantum-ESPRESSO package. For the electronic structure calculations, a Monkhorst-Pack scheme was adopted to integrate over the BZ with a k-mesh 12 $\times$ 12 $\times$ 1 (12 $\times$ 12 $\times$ 6) for the monolayer (bulk) structures. A plane-wave basis kinetic energy cutoff of 500 eV was used. The van der Waals interactions in TaSe$_2$ were accounted for using a semi-empirical correction to the Kohn-Sham energies when optimizing the bulk structures. The optimized lattice parameters for bulk 2H- and 1T-
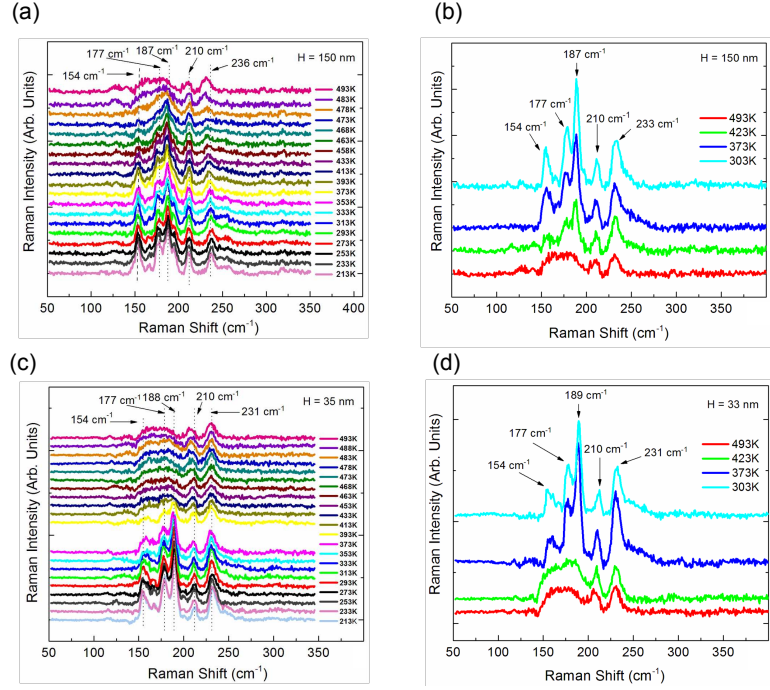
Figure 6.1: Normal (red) and commensurate reconstructed (green) Brillouin zone of bulk and monolayer TaSe$_2$. The equivalent Γ points in the first extended C-BZ and second extended C-BZ are connected to Γ by red and blue vectors, respectively. Figure reproduced with permission from [2]. Experiments conducted by R.Samnakay/A.Balandin (UC Riverside).

TaSe2 are a=3.45$\mathring{A}$, c=13.06$\mathring{A}$ and a=3.42$\mathring{A}$, c=6.22$\mathring{A}$, respectively. These structural parameters are consistent with prior experimental reports of the lattice parameters for the 2H and 1T structures. The lattice constants for the monolayer 2H- and 1T-TaSe$_2$ structures were obtained from the respective optimized bulk structures. The atomic coordinates within the monolayer TaSe$_2$ structures were optimized by introducing a 20-$\mathring{A}$ vacuum layer between the adjacent structures. Spin-orbit coupling was included self-consistently in each calculation. For the phonon dispersion calculations using Quantum-ESPRESSO, an energy cutoff of 500 eV was used in the plane wave basis for the bulk and monolayer structures,. The structures were optimized until the forces on the atoms were less than 0.005 eV/$\mathring{A}$. A 12×12×6 (12×12×1) k-point grid

and a Gaussian smearing of 0.05 eV was used to integrate over the electronic states in the Brillouin zone for the bulk (monolayer) structures. The dynamical matrices for the bulk (monolayer) structure were calculated using a 4×4×2 (4×4×1) q-point grid.

6.2.2   Results and Discussion

To rationalize the experimental data in Figure 6.1, we calculated the total energy of bulk and monolayer 2H- and 1T-TaSe$_2$ in their normal (existing for T$_\xi$T$_{IC}$) and C-CDW (existing for T$_i$T$_C$) phases. We first compare the relative stability of the 2H and 1T polytypes of bulk TaSe$_2$. The 2H polytype is the ground state stacking order and is lower in energy by 0.121 eV/Ta-atom compared to the 1T polytype. This energy difference is a factor of 7 lower than the energy barrier between the 2H and 1T polytypes of MoS$_2$ [201]. This small difference explains why the material grown by CVT contains 2H-TaSe$_2$ even when the synthesis process is optimized for 1T growth (i.e., rapid quenching). The differences in the ground state energies of the C-CDW phases and the normal phases of bulk and monolayer 1T and 2H TaSe$_2$ also were calculated. Figure 6.2 illustrates the CCDW structure for each polytype. 2H-TaSe$_2$ undergoes a commensurate (3×3×3) periodic lattice distortion while 1T-
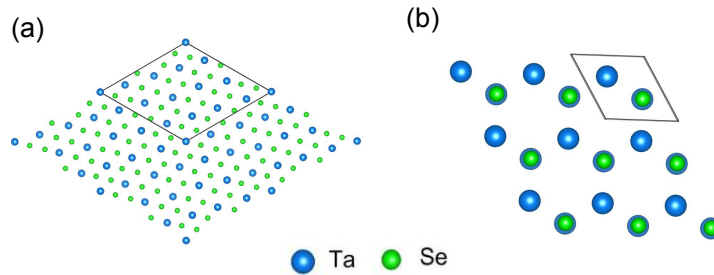
Figure 6.2: Commensurate CDW structures of TaSe$_2$. (a) $\sqrt{13} \times \sqrt{13}$ structure of 1T-TaSe$_2$ and (b) 3×3 structure of 2H-TaSe$_2$.

ΔE (meV/Ta-atom)	Bulk	1L
1T-TaSe2	-21.9	-19.4
2H-TaSe2	-3.50	-2.04

Table 6.2: Calculated Energy Reduction in 1T and 2H TaSe$_2$ C-CDW

TaSe$_2$ undergoes a commensurate ($\sqrt{(13)} \times \sqrt{(13)}$) periodic lattice distortion. For each calculation of the bulk and monolayer C-CDW reconstructed lattices, the lattice constants were fixed and the atomic coordinates were allowed to relax after the tantalum atoms had been displaced from their equilibrium positions. The results of these total energy calculations are summarized in Table 6.2, where ΔE=E$_N$-E$_{C-CDW}$ is the difference between the ground state energies of the normal structure and the C-CDW structure.

For each polytype and dimension, the commensurate CDW structure is predicted by DFT to be the ground state structure. The energy reduction of the bulk CDW supercell is greater than the energy reduction of the monolayer CDW supercell for both the 1T and 2H polytypes. These results are consistent with prior reports of total energy calculations on the bulk C-CDW supercells in 2H- and 1T-TaSe$_2$. [202, 203] A transition to a commensurate CDW lowers the electronic energy. A smaller energy reduction —ΔE— indicates a lower transition temperature. In order to explain the single peak that occurs at 152 - 154 cm^{-1}, the single q-point phonon frequencies of bulk and monolayer TaSe$_2$ were calculated using density functional perturbation theory (DFPT). The reconstruction of the lattice along the basal plane in the C-CDW state of TaSe$_2$results in a reduced Brillouin zone of the C-CDW structure (C-BZ). The C-BZ forms a subset of the normal Brillouin zone (N-BZ) of TaSe$_2$ in its normal undistorted state. Twelve points in the N-BZ get mapped back to Γ in the C-BZ. Figure 6.3 shows the structure of the N-BZ and the C-BZ and the 12 q-points in the N-BZ that are zone-folded to the Γ point of the C-BZ. These zone-folded modes can
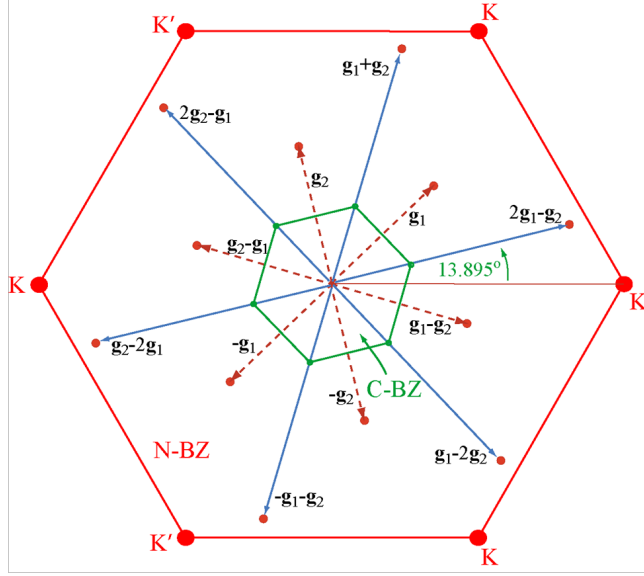
Figure 6.3: Normal (red) and commensurate reconstructed (green) Brillouin zone of bulk and monolayer TaSe$_2$. The equivalent Γ points in the first extended C-BZ and second extended C-BZ are connected to Γ by red and blue vectors, respectively

result in new peaks in the Raman spectrum. The 12 q-points in the N-BZ that map back to Γ in the C-BZ are $\pm g_1$, $\pm g_2$, $\pm(g_1 - g_2)$, $\pm(g_1 + g_2)$, $\pm(g_2 - 2g_1)$ and $\pm(2g_2 - g_1)$ where g_1 and g_1 are the reciprocal lattice constants of the C-BZ. The reciprocal lattice constants are $\mathbf{g}_1 = \frac{G}{13}(2\sqrt{3},-1)$ and $\mathbf{g}_2 = \frac{G}{13}(\frac{-\sqrt{3}}{2},\frac{7}{2})$ respectively, where G is the magnitude of the reciprocal lattice vector of the N-BZ. The normal-phase phonon frequencies at Γ, $q = g_1$ and $q = g_1 + g_2$ in the N-BZ are calculated and summarized in Table 6.3 for bulk and monolayer 1T-TaSe$_2$.

The 5 other q-points shown in Figure 6.3 with magnitude —g_1— have the same frequencies as those at g_1, and the 5 other q-points with magnitude —g_1+g_2— have the same frequencies as those at g_1+g_2. Only frequencies between 100 cm^{-1} and 270 cm^{-1} are shown. As shown in Table 6.3, the modes originating from the q-points in Figure 6.3 have energies of $\sim$152 - 154 cm^{-1} (highlighted in bold font). This indicates that all of these phonon modes may contribute to the Raman peak observed

103

q-point	Monolayer normal phase (cm^{-1})	Bulk normal phase (cm^{-1})
Γ	143 (IR), 143 (IR), 173 (R), 173(R), 188 (R), 210 (IR)	146 (IR), 146 (IR), 175 (R), 175 (R), 191(R), 219 (IR)
g_1	109, 118, 144, **154**, 180, 249	122, 149, **152**, 197, 215, 261
g_1+g_2	108, 117, 143, **154**, 165, 181, 249	121, 148, **153**, 172, 196, 214, 260

Table 6.3: Calculated phonon energies of normal-phase bulk and monolayer 1T-TaSe$_2$ at Γ and at the q points in the N-BZ that are folded back to Γ in the C-BZ. The IR active (IR) and Raman active (R) modes at Γ are indicated.

experimentally at 152 - 154 cm^{-1}. The fact that the 12 q-points in the N-BZ that are equivalent to Γ in the C-BZ have frequencies 152 - 154 cm^{-1} corresponding to the new Raman peak is consistent with the view that the new peak is the result of zone-folding associated with the re-constructed lattice. We also observe that the the Raman active modes of the normal bulk phase are close to the experimentally observed modes at 177 cm^{-1} and 187 - 189 cm^{-1} shown in Figs. 6.1. So far, we have considered phonon modes of the normal lattice consisting of 3 atoms per unit cell at momenta that are at equivalent Γ points of the reconstructed C-CDW lattice, and we find that one of their energies corresponds to a new peak in the Raman spectrum of the C-CDW phase. To further investigate the new Raman peaks of the C-CDW phase, we calculate the phonon energies of the C-CDW reconstructed lattice with 39 atoms in the unit cell for bulk and monolayer 1T-TaSe$_2$. Table 6.4 shows the calculated phonon frequencies between 100 cm^{-1} and 270 cm^{-1} which is a subset of the 117 phonon modes that occur in the bulk and monolayer C-CDW structures.

The modes are grouped according to the phonon energies of the normal phase listed in Table 6.3. The Γ-point phonon energies of the C-CDW phase are centered around the normal-phase phonon energies listed in Table 6.3 for both the bulk and monolayer structures. The number of phonon modes that occur within each frequency range is listed in parentheses. The splitting of the phonon energies is not unexpected

C-CDW Γ-point phonons (cm-1)	
Monolayer	Bulk
101 - 122 (15)	120 - 123 (9)
144 (9)	**151 - 158 (15)**
150 - 158 (12)	163 - 169
160 - 179 (13)	172 - 179 (8)
181 - 189 (11)	180 - 188 (9)
243 - 257 (18)	190 - 197 (7)
	201-217 (11)
	251 - 266 (10)

Table 6.4: Calculated Γ point phonons of the reconstructed C-CDW structure in monolayer and bulk 1T-TaSe$_2$ grouped by the normal-phase phonon energies in Table 6.3

since the 12 modes of the normal lattice are coupled by the C-CDW wavevectors **Q** which form the reciprocal lattice vectors of the commensurate Brillouin zone (C-BZ) shown in Fig. 6.3 Thus, the CDW potential V$_\mathbf{Q}$ couples and splits the phonon modes of the normal lattice. The calculated bulk Γ-valley phonons listed in Table 6.4 are within 1 cm^{-1} to 6 cm^{-1} of the zone folded normal-phase 152 cm^{-1} frequency given in Table 6.3 and the experimentally observed 154 cm^{-1} frequency shown in the Raman spectra in Figs. 6.1. In the bulk and monolayer C-CDW structures, the eigenvectors of the phonon frequencies in the range of 150 cm-1 to 158 cm-1 are a mixture of transverse and longitudinal displacements of the 26 Se atoms and 13 Ta atoms. As a result, they cannot be easily categorized as A$_{1g}$ or E$_{2g}$ modes, and their symmetry is not obvious. Assuming that these modes originate from a zone-folding of the low-symmetry points g$_1$ and g$_1$+g$_2$ in the N-BZ, this low symmetry would be expected. The eigenvectors of the normal-phase phonons at g$_1$ and g$_1$+g$_2$ are also a mix of transverse and longitudinal displacements, so it is not surprising that the new Raman mode that appears at Γ in the C-CDW phase is a mix of transverse and longitudinal

displacements. Since there is a possibility of 3R-TaSe$_2$ residue in CVT synthesized samples we theoretically analyzed the phonon spectrum of this polytype to exclude the possibility of the new Raman peaks arising from the 3R-TaSe$_2$ phonon modes. We calculated the Γ-point phonons and Raman active modes of bulk 3R-TaSe$_2$ using density functional perturbation theory. The 3R-TaSe$_2$ polytype has a space group R-3m. The unit cell consists of three monolayers of TaSe$_2$ that have a trigonal prismatic coordination of the Ta atom. The Raman modes of the 3R structure remain the out-of-plane A$_{1g}$ mode and the in-plane E$_{2g}$ mode. The calculations indicate that the A$_{1g}$ and E$_{2g}$ frequencies of bulk 3R-TaSe$_2$ are $\sim$230 cm^{-1} and $\sim$191 cm^{-1}, respectively. These frequencies are not in the range of the new Raman peak of interest and hence do not affect the interpretation of the zone-folded peak.

6.2.3 Conclusion

In summary, a comparison of the Raman data with ab initio calculations of the vibrational modes of both the normal and C-CDW phases gave a consistent picture of the zone-folding of the phonon modes following lattice reconstruction. The q-points of the normal lattice that lie at equivalent Γ points of the C-CDW reconstructed lattice all have a phonon mode at, or within 2 cm^{-1}, of the frequency of the new Raman peak. The calculated Γ-point phonon frequencies of the bulk reconstructed C-CDW lattice show a splitting of the modes into a cluster of frequencies between 151 and 158 cm^{-1}. These modes are a mixture of transverse and longitudinal displacements of the 26 Se atoms and 13 Ta atoms, and, as a result, they cannot be easily categorized as Raman active modes, and their symmetry is not obvious. The total energy calculations of the normal and C-CDW phases of bulk and monolayer 1T and 2H polytypes show that the energy difference between the normal and the C-CDW phase of the bulk is

greater than that of the monolayer, and this is consistent with a reduced transition temperature for a monolayer compared to that of the bulk. The experimental thicknesses did not come close to a monolayer, so we simply note that the trend of lower C-CDW temperature for lower thickness is consistent with the experimental trend.

6.3 1T-TiSe$_2$

1T-TiSe$_2$ is a transition metal dichalcogenide that also exhibits a charge density wave transition. The material undergoes a phase transition from its normal phase to a commensurate charge density wave phase below 200K. The electronic structure of bulk TiSe$_2$ has been intensely studied experimentally and theoretically. It is predicted to be either a semimetal [204, 205] or an indirect gap semiconductor [47, 206–208]. This has led to a range of interpretations of the CDW ground state and the periodic lattice distortion (PLD) observed below 200K in bulk TiSe$_2$. Explanations that range from a Jahn-Teller effect, [47, 209, 210] correlated mechanisms that lead to an excitonic insulator state [206, 211, 212] to the presence of chiral order in TiSe$_2$ at low temperatures [213, 214] have been suggested. A number of recent experimental results have shown that the CDW transition in 1T-TiSe$_2$ is driven by an excitonic insulator transition. [215] In the normal phase bulk TiSe$_2$ is a semi-metal with a hole pocket and electron pocket at the Γ_v and L_c valleys respectively. Photoemission experiments have shown these bands overlap by $\sim$200 meV above the CDW transition temperature. Ab-initio studies at the LDA and GGA level of theory have shown this overlap between the bands can vary between 180 meV and 250 meV in bulk TiSe$_2$. Neither local or semi-local approximations to density functional theory have been able to predict the presence of this excitonic insulator state in bulk TiSe$_2$. In this study we show that the excitonic gap in bulk TiSe$_2$ can be described using either the

hybrid range separated Heyd-Scuseria-Ernzerhof (HSE) functional or calculation of the quasi particle energies using the GW approximation. Applying these calculations to the bulk and monolayer structures results in a bandgap that is a factor of $\sim$2 larger than the bulk structure.

6.3.1 Computational Methods

We use ab-initio calculations of the bulk, monolayer, and bilayer $TiSe_2$ electronic structures. Fig. 6.4 illustrates a top-view of the atomic structure of a monolayer $TiSe_2$ supercell.
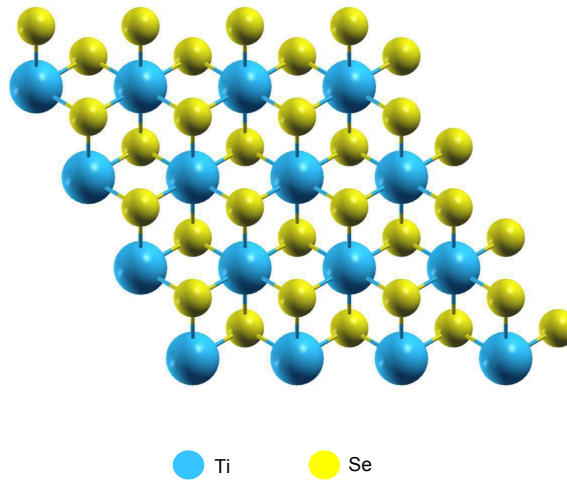
Figure 6.4: Top view of the atomic structure of 1T-$TiSe_2$ in the 2×2 supercell).

Density functional theory (DFT) as implemented in the Vienna Ab-initio Simulation Package ($VASP$) [216] are used to investigate the CDW instability in bulk and few-layer $TiSe_2$. The Perdew-Burke-Ernzerhof (PBE) Generalized Gradient Approximation (GGA) of DFT is used as an initial approximation in the calculations. Spin orbit coupling is self consistently included in the calculations and the results are compared to the results with no spin orbit interaction. The bulk structure of 1T-$TiSe_2$ is

optimized using the Grimme-D2 correction to the Kohn-Sham energies to account for van-der-Waal interactions. All atomic positions were fully optimized until the forces acting on each atom is less than 0.01 eV/$\mathring{A}$. A Monkhorst-Pack scheme is adopted to integrate over the Brillouin zone with a k-point mesh of $8 \times 8 \times 4$ for the bulk and $8 \times 8 \times 1$ for the thin films. The energy cut off of the plane wave basis is 500 eV. For the HSE calculations of the bulk and monolayer structures, 25% to 35% short-range exact Hartree-Fock (HF) exchange was used with the PBE correlation. The G_0W_0 calculations of the bulk structure are converged using a k-point grid of $12{\times}12{\times}6$ and 240 empty conduction bands. The G_0W_0 calculations of the monolayer structure use a k-point grid of $12{\times}12{\times}1$, 320 empty conduction bands and a $20\mathring{A}$ vacuum.

The vdW optimized lattice parameters for the bulk are 3.661 $\mathring{A}$ and 5.965 $\mathring{A}$ which is in agreement with previous experimental studies [217]. The optimized thickness of the monolayer thin film is 3.405 $\mathring{A}$ and the bilayer thin film is 10.912 $\mathring{A}$.

6.3.2   Results and Discussion

The PBE and GW band structures with no SOC for the normal bulk and monolayer 1T-TiSe$_2$ structures are plotted in Fig. 6.5. Our calculations show bulk TiSe$_2$ is a
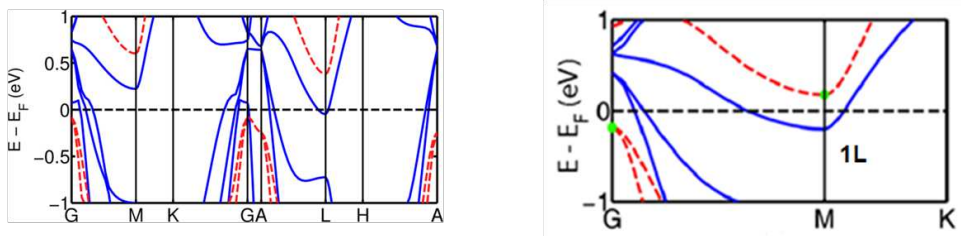
Figure 6.5: LDA (blue) and GW (red) bandstructure of (a) bulk and (b) monolayer TiSe$_2$).

semi-metal with a negative overlap of 280 meV of the hole and electron bands at the Γ and the L symmetry points respectively. When the bulk structure is confined to a

single monolayer or bilayer thin-film, our calculations continue to show an electronic structure that remains semi-metallic. In the monolayer and bilayer structures, the overlap of the hole and electron pockets is now at the Γ and M valleys respectively. Spin-orbit interaction does not change the properties of the PBE band structures. The PBE-SOC calculations of the bulk and monolayer structure of TiSe$_2$ still results in a semi-metallic band structure. The overlap of the electron and hole bands of the bulk (monolayer) structure with SOC included is 300 meV. Hence, the default level of theory in all the calculations discussed is LDA with no spin-orbit coupling.

The GW correction to the PBE energies results in a semi-metal to insulator transition. The bulk GW bandgap is 140 meV and the monolayer GW bandgap is 260 meV. We compare our results to the HSE calculation for a range of different exact exchange percentages. Increasing the amount of exact exchange in the HSE calculation of bulk TiSe$_2$ from 10% to to 35% increases the Γ_v to L$_c$ bandgap from 108 meV to 423 meV.

6.3.3   Conclusion

In conclusion the electronic structure of bulk and monolayer 1T-TiSe$_2$ is studied using the LDA, GW and HSE approximations of density functional theory. The LDA and GGA calculations of bulk TiSe$_2$ predict the material to be a semi-metal which is in disgareement with experimental results that demonstrate an excitonic insulating phase that follows the transition to a commensurate charge density wave phase. LDA and GGA and calculations of the monolayer structure predict semi-metallic behavior as well. GW calculations at the G$_0$W$_0$ level of theory and hybrid HSE calculations demonstrate the presence of a gapped state at the Γ_v and L$_c$ valleys of the bulk structure and Γ_v and M$_c$ valleys of the monolayer structure. Initial calculations of

the gap in the monolayer structure suggests that the value of the excitonic gap is larger in comparison to the bulk structure. However, further convergence of the GW and HSE calculations is necessary to obtain an accurate value of the excitonic gap in the monolayer TiSe$_2$ structure.

Chapter 7

Conclusion

There is growing interest in the controlled synthesis and characterization of different van-der-Waal materials beyond graphene. The electronic and vibrational properties of these materials qualitatively changed as they are confined from their bulk structures to the single monolayer limit. Growth and mechanical exfoliation of these layered materials also leads to interfaces that are misoriented with respect to each other, which in turn can affect the electronic and vibrational properties. Proximity between monolayers of layered materials can qualitatively alter the monolayer electronic and vibrational properties of interest. This can result in changes in the electrical conductivity, Seebeck coefficient, thermal conductivity and correlated phenomena (eg. charge density waves) in this class of materials.

In this work the bulk to monolayer electronic properties for a wide range two dimensional layered materials have been studied using ab-initio density functional theory. In Chapter 1 the different materials and phenomena studied is introduced. An overview of the ab-initio calculation methods used to study these materials and phenomena is summarized in Chapter 2. Chapters 3 and 4 investigate the electronic and thermoelectric properties of the semiconducting transition metal dichalcogenides

as a function of film thickness and misorientation. In these chapters changes in the band gaps, band offsets, effective masses are calculated for a range of Group VI TMDC materials using different levels of ab-initio DFT theory. The calculated band structures are used as an input to our Landauer model to calculate the thermoelectric properties of these materials in linear response. Chapter 5 investigates the electronic and thermoelectric properties of semiconducting layered materials that exhibit a Fermi ring in their electronic structure. In Chapter 6 the electronic and vibrational properties of the metallic and semi-metallic TMDCs are investigated and the results are compared to available experimental data.

The critical findings of this dissertation are summarized below:

1. The Group VI semiconducting TMDCs exhibit large n-type (p-type) band degeneracy as the K_c and Λ_c (K_v and Γ_v) conduction (valence) band valleys move within k_BT of each other for film thicknesses greater than two monolayers. The interlayer hybridization and energy level splitting determine how the number of conducting modes within k_BT of a valley minimum changes with layer thickness. The maximum number of conducting modes is directly proportional to the electrical conductance; the thickness at which this occurs is in general not a monolayer.

2. Misorientation between bilayers of MoS_2, $MoSe_2$, WS_2 and WSe_2 can increase the van-der-Waal gap distance between the individual monolayers, decrease interlayer coupling and increase the magnitude of the bandgap by up to 100 meV.

3. The valence band of the Group-III chalcogenides transforms from a parabolic to an inverted Mexican hat dispersion when confined from the bulk structure to a single monolayer. This dispersion gives rise to an anisotropic Fermi ring at the band edge which results in a singularity in the density of states, a step

function turn on in the density of modes and leads to an enhancement of the thermoelectric response of a material by up to an order of magnitude.

4. The transition to a commensurate charge density wave (CDW) phase in 1T-TaSe$_2$ results in a Brillouin zone that is rotated with respect to the normal Brillouin zone and is reduced by $\sqrt{13}$.

5. One of the zone folded phonon modes at Γ in the commensurate CDW phase of 1T-TaSe$_2$ occurs at 152-154 cm^{-1} in the bulk and monolayer structures, which is consistent with the experimental observation of a Raman peak at 154 cm^{-1} below the commensurate CDW transition temperature.

6. The excitonic insulator phase that occurs in 1T-TiSe$_2$ is described using ab-initio GW calculations of the bulk and monolayer structures. The GW bandgap of the bulk and monolayer structures is 140 meV and 260 meV respectively.

Appendix A

HSE calculations of layered metal dichalcogenides and monochalcogenides

The electronic properties of the layered materials investigated in this study are sensitive to the choice of exchange correlation approximation used. For a majority of the electronic and thermoelectric properties of the materials investigated in this study, a standard local or semi-local approximation to DFT provides the salient properties of each material. The Perdew-Wang-Ernzherhof (PBE) functional correctly describes each of the semiconducting layered dichalcogenides to have a bandgap and the band minima are predicted to be at the correct valleys in k-space (provided van-der-Waal interactions are accounted for during geometry optimization). However, the bandgaps predicted by the PBE functional are often underestimated compared to experimental results, which in turn affects the band-offsets between higher energy valleys. To correct for this we employ the hybrid HSE functional. The amount of exact exchange or the screening parameter is empirically tuned to match experimental reports of

Material	Effective Masses			Band Splitting	
	Direction	K_v (m_0)	K_c (m_0)	ΔK_v (meV)	ΔK_c (meV)
MoS$_2$	Longitudinal	0.485	0.407	188.6	9.9
	Transverse	0.480	0.404		
MoSe$_2$	Longitudinal	0.503	0.435	254.8	36.9
	Transverse	0.503	0.436		
MoTe$_2$	Longitudinal	0.576	0.501	317.4	43.7
	Transverse	0.565	0.500		
WS$_2$	Longitudinal	0.304	0.331	528.7	12.0
	Transverse	0.305	0.332		
WSe$_2$	Longitudinal	0.303	0.358	606.4	7.80
	Transverse	0.303	0.359		

Table A.1: Longitudinal and transverse electron and hole effective masses, band splitting at K for conduction and valence band calculated using the HSE function with spin orbit coupling

bandgaps. The HSE functional leads to corrections of the under-estimated PBE bandgaps, lower effective masses compared to the PBE functional, corrections to the band offsets between valleys and corrections to the splitting of the conduction and valence bands due to spin orbit coupling. The longitudinal and transverse effective masses of monolayers of the Group VI TMDs and the conduction and valence band splitting at K calculated with HSE is summarized in the Table below. The hybrid HSE functional also changes the energy offset between the band extrema and high energy valleys, specifically the energy difference between the conduction band valley, K_c, and the Sigma valley, Σ_c for the electrons and the valence band K_v valley and the Γ_v valley for the holes. The energy difference between these valleys for the electrons and holes for monolayers of the Group VI TMDs is illustrated below in Figure A.1. Applying corrections to standard LDA or GGA calculations of the monolayer and few-layer TMDs is not only essential to correct the underestimated bandgaps,
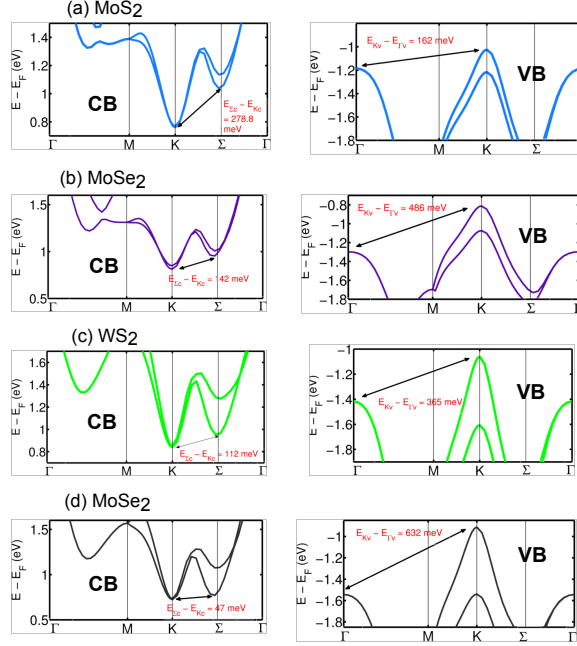
Figure A.1: Offsets between conduction band valley, K_c and Σ_c valley and valence band valley, K_v and the Γ_v valley for monolayer (a) MoS$_2$, (b) MoSe$_2$, (c) WS$_2$ and (d) WSe$_2$. Calculations are done using the hybrid HSE functional with spin orbit interaction

it also corrects the band offsets between higher energy valleys as a function of film thickness. Obtaining quantitatively accurate values of the bandoffsets is essential to correctly account the valley degeneracy introduced by the K, Σ_c and Γ_v valleys. The K_v and K_c have a degeneracy of 2, the Σ_c has a degeneracy of 6 and the Γ_v has a degeneracy of 1. Accounting for these degeneracy factors in the number of conducting modes and the density of states when modeling field-effect-transistor characteristics and thermoelectric performance is essential to ensure the correct trends as a function of film thickness are obtained. Illustrated in Figure A.2 below is the energy difference between the conduction band K_c and Σ_c valleys and valence band K_v and Γ_v valleys as a function of film thickness for the semiconducting TMDs. The band offset energies for each material as a function of film thickness is tabulated in Table A.2 below.

The correction to the underestimated bandgaps provided by the hybrid HSE func-
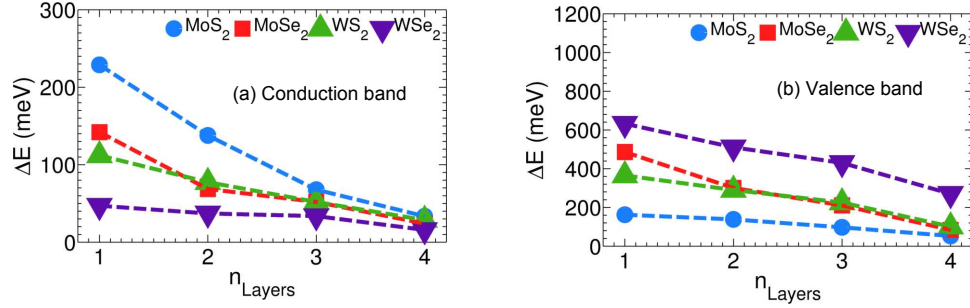
Figure A.2: Band offsets calculated using the hybrid HSE functional with spin orbit coupling for one to four monolayers of MoS_2, $MoSe_2$, WS_2 and WSe_2. (a) Offset between the conduction band K_c and Σ_c valleys, (b) Offset between the valence band K_v and Γ_v valleys.

Structure	Transition (meV)	MoS_2	$MoSe_2$	WS_2	WSe_2
1L	Γ_v to K_v	162.1	486.1	365.0	632.0
	K_c to Σ_c	228.8	142.0	112.0	47.0
2L	Γ_v to K_v	138.1	300.2	290.1	510.0
	K_c to Σ_c	137.7	68.6	77.4	37.0
3L	Γ_v to K_v	97.1	210.5	225.3	430.0
	K_c to Σ_c	67.7	51.9	50.6	33.6
4L	Γ_v to K_v	52.6	84.1	100.7	270.1
	K_c to Σ_c	33.4	23.9	28.5	15.8

Table A.2: HSE-SOC calculations of conduction and valence band offsets as a function of film thickness.

tional occurs due to shifts of the absolute valence and conduction band energies compared to the mean field PBE calculation. The hybrid HSE functional rigidly shifts the conduction band energies up with respect to the PBE conduction band energies. The HSE functional lowers the the valence band energies with respect to the PBE valence band energies but by an amount that is lower in comparison to the correction applied to the conduction band energies. Illustrated in Figure A.3 below are the natural band lineups between the monolayer semiconducting Group VI transition metal dichalcogenides and 1T and 2H SnS. Obtaining accurate descriptions of the natural band lineups between materials is essential to identify suitable material materials
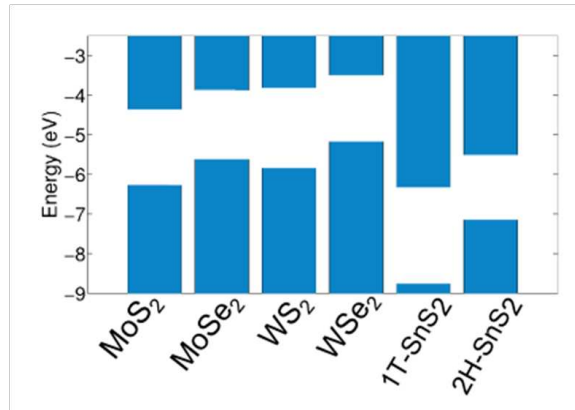
Figure A.3: Natural band line up between monolayers of MoS_2, $MoSe_2$, WS_2 and WSe_2 in a trigonal prismatic coordination and SnS in a trigonal prismatic (2H) and octahedral (1T) coordination. Calculations are done using the hybrid HSE functional with spin orbit interaction
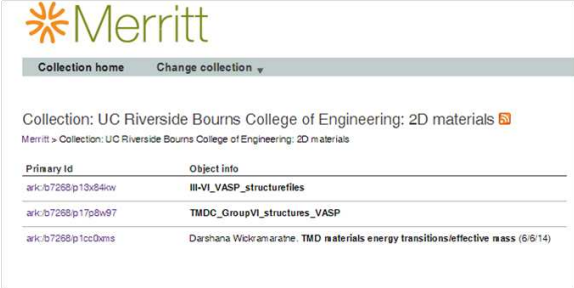
for applications in tunnel field effect transistors, photocatalytical water splitting and

photovoltaics.

Appendix B

2D Material Database

The structure files and data files generated through the course of this study have been uploaded to the *UC Riverside Bourns College of Engineering: 2D materials* Merritt repository which is hosted by the University of California Curation Center (UCR3). The URL for the repository can be accessed online through Ref. [218]. This persistent URL can be shared with any researcher which provides them access to the range of structure files, output data files and post-processing scripts that have been uploaded. The data sets that have been uploaded are listed in alphabetical order of the Primary Id as illustrated in Figure B.1 below. The steps to retrieve and add files from and

Figure B.1: Main page of 2D materials database

to the repository are listed below. Detailed documentation on managing data on the

repository can be found online in Ref. [219]

B.1 Retrieving Data

The *Primary Id* link provides access to the metadata associated with a data set along with the link to download the dataset using the *Download object* button. An example screen capture is illustred below.

Figure B.2: Data retrieval screen and object metadata on Merritt repository

B.2 Adding Data

Members of the *LAboratory For Terascale and Terahertz Electronics* have the ability to continue to add files to the repository. A wide range of data (images, text, etc.) and file types (.pdf, .tar, .zip) are supported. To upload data through the Merritt User Interface use the *Add Object* screen of the repository. An example screen capture is illustrated below.

Figure B.3: Data upload screen with Merritt repository

The minimum recommended requirements for an upload include

- A single object file that will be uploaded

- Metadata for the object file being uploaded. This includes a title name for the file, name of uploader and date of upload.

Appendix C

VASP Postprocessing Scripts

A number of MATLAB scripts have been used throughout this study to post-process the data generated by VASP. These scripts read the EIGENVAL and DOSCAR files output by VASP and are used to extract and plot band structure, total and orbital and site projected density of states and to calculate the density of modes which is used as input for the linear response calculations of material properties. These scripts organized by their function are listed in this section of the Appendix along with a brief tutorial on their use.

C.1   VASP bandstructure

To plot the bandstructure with VASP the EIGENVAL file following a bandstructure is required for the MATLAB code listed below.

```
clear all
```

```
%E-k plot from VASP data
```

```matlab
%% just for chalcogenides: bulk(hexagonal) and 2D


ev_to_ryd=13.6;
%%%%%%% Inputs %%%%%%


% Input file for E-k data in VASP:EIGVAL  %
%------------------------------------%


filename='EIGENVAL';


% Fermi energy of the system in eV %


%Ef=5.0265;
Nk=20;
Ne=32;


% number of directions%
% hex=7; 2D=3 %
Nd=3;
Ntotal=Nk*Ne*Nd;



%%%%%%%%  First Block: Reading  %%%%


fid=fopen(filename,'r');
col = zeros(Ntotal,1);
```

```matlab
%skip first 6 lines

for i = 1:6
    line=fgetl(fid);
end

colIndex = 1;

for ii=1:Nk*Nd

c = textscan(fid,'%d %f',Ne+2);
%c = textscan(fid,'%d %f %f',Ne+2);
col(colIndex:colIndex+Ne-1) = c{1,2}(3:Ne+2);
col(colIndex:colIndex+Ne-1) = c{1,2}(3:Ne+2);
colIndex = colIndex + Ne;
end
fclose(fid);

A=col;

clear col
A=A-Ef;
%%%
```

```matlab
%% for 2D structure: 1L, 2L %%

%{

l1=0.5774; l2=l1+0.3333; l3=l2+0.6667;

%l1=0.6667; l2=l1+0.5774; l3=l2+0.3333; %K - G - M -  K


%l1=0.6667; l2=l1+0.5774; l3 = l2+0.3333; % Used for K - G - M




k1=linspace(0,l1,Nk); k2=linspace(l1,l2,Nk);

k3=linspace(l2,l3,Nk);

kmesh=[k1' k2' k3'];


% for the vertical lines to show k directions

Emin=-2; Emax=3;

EE=[Emin Emax];

KD1=[l1 l1]; KD2=[l2 l2]; KD3=[l3 l3];


% for the horizontal line to show the Fermi level %

kmin=0; kmax=l3;

kk=[kmin kmax]; E=[0 0];

klabel=['G';'M';'K';'G'];



%}
```

```
%% for hexagonal bulk structure %%

% k mesh%%

c1=0.5774; c2=0.3334;
c3=0.6667; c4=0.1228;
%% G-M-K-G-A-L-H-A
%c1=0.5; c2=0.5; c3=0.4;
c4=0.5; %% G-M-K-G-A-L-H-A

%c1=0.1228; c2=0.5774;
c3=0.3334; c4=0.6667; %% G-A-L-H-A
%c1=0.1228; c2=0.6667;
c3=0.1228; c4=0.6667; %% H-K-G-A-H


l1=c1; l2=l1+c2; l3=l2+c3; l4=l3+c4; l5=l4+c1;
l6=l5+c2; l7=l6+c3;

k1=linspace(0,l1,Nk);
k2=linspace(l1,l2,Nk);
k3=linspace(l2,l3,Nk);
k4=linspace(l3,l4,Nk);
k5=linspace(l4,l5,Nk);
k6=linspace(l5,l6,Nk);
```

```matlab
k7=linspace(l6,l7,Nk);

kmesh=[k1' k2' k3' k4' k5' k6' k7'];


% for the vertical lines to show k directions

Emin=-2.8; Emax=2.8;

EE=[Emin Emax];

KD1=[l1 l1]; KD2=[l2 l2]; KD3=[l3 l3]; KD4=[l4 l4];

KD5=[l5 l5]; KD6=[l6 l6];


% for the horizontal line to show the Fermi level %

kmin=0; kmax=l3;

kk=[kmin kmax]; E=[0 0];

%klabel=['G';'M';'K';'G';'A'; 'L'; 'H'; 'A'];

%}



%% Find the band gap  %%

%% works only when Ef is inside the bandgap %%


Nkk=Nk*Nd;

cond_min=zeros(1,Nkk);

valence_max=zeros(1,Nkk);



for ii=1:Nkk

    Ekk= A((ii-1)*Ne+1:ii*Ne);
```

```matlab
    ind_valence = find(Ekk <= 0);

    ind_conduct = find(Ekk >= 0);

    valence_max(ii) = max(Ekk(ind_valence));

    cond_min(ii) = min(Ekk(ind_conduct));

end


[E_top_valence, ind_q_val] = max(valence_max);

[E_bot_conduct, ind_q_cond] = min(cond_min);


%kmeshplot=[k1 k2 k3 k4 k5 k6 k7];

kmeshplot=[k1 k2 k3 k4 ];


%kmeshplot=[k1 k2 k3];

%kmeshplot=[k1 k2];


k_top_valence=kmeshplot(ind_q_val)

k_bot_conduct=kmeshplot(ind_q_cond)



%figure('units','inches','position',[0.1 0.1 9 5]);

%%%%%%%%  Plotting  %%%

Ek_VB=[];

Ek_CB=[];

figure(2);

for jj=1:Nd

Ek=[]; Ni=Nk*jj;
```

```
for ii=1+(Ni-Nk):Ni

Ekk= A((ii-1)*Ne+1:ii*Ne);

Ek=[Ek;Ekk'];

end

hold on

plot(kmesh(:,jj),Ek,'r--','LineStyle','-','linewidth',[4]);

end

plot([0 kmax], [0.0 0.0], 'k--', 'linewidth', 4')

axis([kmin kmax Emin Emax])


% vertical lines to show each k directions


plot(KD1, EE, 'k','linewidth',[1])

plot(KD2, EE, 'k','linewidth',[1])

plot(KD3, EE, 'k','linewidth',[1])

plot(KD4, EE, 'k','linewidth',[1])

plot(KD5, EE, 'k','linewidth',[3])

%plot(KD6, EE, 'k','linewidth',[3])


%set(gca,'XTick',[0 l1 l2 l3 l4 l5 l6 l7])

set(gca,'XTick',[0 l1 l2 l3 l4 l5])


%set(gca,'XTick',[0 l1 l2 l3  ])


set(gca, 'XTickLabel',klabel)

box on
```

```
set(gcf, 'Color','w')

hold on


if E_bot_conduct < E_top_valence

    E_gap = 0;

    fprintf('\n Band gap = 0 eV\n')

else

    E_gap = E_bot_conduct - E_top_valence;

    fprintf('\n Band gap = %f eV\n', E_gap)

end
```

C.2   VASP Total and Projected Density of States

To calculate, plot and analyze the total and projected density of states of a material using VASP the DOSCAR file is required. The MATLAB code listed below parses the information contained within the DOSCAR file and enables the total and projected density of states to be plot.

```
%clear all


ev_to_ryd=13.6;


%%%%%%% Inputs %%%%%%


filename='DOSCAR';


Ef=-2.999;
```

```matlab
% number of energy points for each direction %

Ne=3000;


% Number of atoms, required for pdos only

Na=3;


fid=fopen(filename,'r');


%skip first 6 lines


for i = 1:6

    line=fgetl(fid);

end


c = textscan(fid,'%f %f %f',Ne);   %% read the data %

col1 = c{1,1}(1:Ne);

col2 = c{1,2}(1:Ne);

col3 = c{1,3}(1:Ne);


fclose(fid);


A=[col1 col2 col3];

E1=A(:,1)-Ef;
```

```matlab
dos=A(:,2);


break


Ntotal=Ne*Na;

fid=fopen(filename,'r');


col1 = zeros(Ntotal,1);

col2 = zeros(Ntotal,1);

col3 = zeros(Ntotal,1);

col4 = zeros(Ntotal,1);

col5 = zeros(Ntotal,1);

col6 = zeros(Ntotal,1);

col7 = zeros(Ntotal,1);

col8 = zeros(Ntotal,1);

col9 = zeros(Ntotal,1);

col10 = zeros(Ntotal,1);


%skip first Ne+6 lines


for i = 1:Ne+6

line=fgetl(fid);

end
```

```
% loop (skip first 1 line and read Ne lines) until end


colIndex = 1;
%order is s, py, pz, px, dxy, dyz, dz2-r2, dxz, dx2-y2
%PDOS is output for each atom
for ii=1:Na
c = textscan(fid,'%f %f %f %f %f %f %f %f %f %f',Ne+1);
col1(colIndex:colIndex+Ne-1) = c{1,2}(2:Ne+1);
col2(colIndex:colIndex+Ne-1) = c{1,3}(2:Ne+1);
col3(colIndex:colIndex+Ne-1) = c{1,4}(2:Ne+1);
col4(colIndex:colIndex+Ne-1) = c{1,5}(2:Ne+1);
col5(colIndex:colIndex+Ne-1) = c{1,6}(2:Ne+1);
col6(colIndex:colIndex+Ne-1) = c{1,7}(2:Ne+1);
col7(colIndex:colIndex+Ne-1) = c{1,8}(2:Ne+1);
col8(colIndex:colIndex+Ne-1) = c{1,9}(2:Ne+1);
col9(colIndex:colIndex+Ne-1) = c{1,10}(2:Ne+1);
col10(colIndex:colIndex+Ne-1) = c{1,1}(2:Ne+1);
colIndex = colIndex + Ne;
end


fclose(fid);


E2=col10(1:Ne)-Ef;
colt=col1+col2+col3+col4+col5+col6+col7+col8+col9;
colts=col1;
coltp=col2+col3+col4;   %%
```

```
coltd=col5+col6+col7+col8+col9;



%B=[colt col1 col2 col3 col4 col5 col6 col7 col8 col9];

B=[colt colts coltp coltd];


tdos=zeros(Ne,1);

ddos=zeros(Ne,1);

dz2dos=zeros(Ne,1);

dxydos=zeros(Ne,1);

dx2y2dos=zeros(Ne,1);

pzdos=zeros(Ne,1);

pxdos=zeros(Ne,1);

pydos=zeros(Ne,1);



%total Density of states from PDOS

for jj=1:Na

    tdos=tdos+colt(Ne*(jj-1)+1:jj*Ne);

end


%total d-orbital Density of states from PDOS

for jj=1:Na

ddos=ddos+coltd(Ne*(jj-1)+1:jj*Ne);

end
```

```
for jj=1:Na

dz2dos=dz2dos+col7(Ne*(jj-1)+1:jj*Ne);

dxydos=dxydos+col5(Ne*(jj-1)+1:jj*Ne);

dx2y2dos=dx2y2dos+col9(Ne*(jj-1)+1:jj*Ne);

end


for jj=1:Na

pzdos=pzdos+col3(Ne*(jj-1)+1:jj*Ne);

pxdos=pxdos+col4(Ne*(jj-1)+1:jj*Ne);

pydos=pydos+col2(Ne*(jj-1)+1:jj*Ne);


end
```

C.3   VASP Density of Modes

To calculate the thermoelectric properties in linear response in this work we numerically calculate the density of modes using the ab-initio simulation package, VASP. The density of modes for a given structure and material is computed by "counting" the number of bands that intersect within an energy range of interest over which the density of modes (DOM) is being computed. The band-counting approach for a 1D band is illustrated below.

Extrapolating this heuristic 1D band-counting method to a full numerical band structure requires the energy versus momentum dispersion for all k-points within the irreducible Brillouin zone of the material. These eigen-energies and bands at each k-point are calculated using VASP in this work. In principle, the energy versus momentum relation can be obtained from any electronic structure approach. The

MATLAB code that is used to count over the density of modes using an EIGENVAL file from VASP is detailed below.

```
 clear all


%% mode calculations from Vasp E-k data  %%
%% Written by Darshana Wickramaratne  %%


ah=3.818e-10; %lattice constant
kymax=(2*pi/ah)*(1/sqrt(3)); %TMDC


Lz=5.193e-10;


pre_factor = 1/pi
Eg_exp=1.9;
Eg_Vasp=1.68;
Eshift=(Eg_exp-Eg_Vasp)/2;


filename='Ek_1L_InS_51_51';


%Ef= 1.0591;


%----------------------------%
Nx=51; Ny=51;
Nk=Nx*Ny;
Nb=64;
```

```matlab
Nd=1;

Ntotal=Nk*Nb*Nd;

Ne=2001;

Emin=-2; Emax=2;

E = linspace(Emin,Emax,Ne);


fid=fopen(filename,'r');

col = zeros(Ntotal,1);


for i = 1:6

    line=fgetl(fid);

end


colIndex = 1;


for ii=1:Nk*Nd

    c = textscan(fid,'%d %f',Nb+2);

    col(colIndex:colIndex+Nb-1) = c{1,2}(3:Nb+2);

    colIndex = colIndex + Nb;

end


fclose(fid);


A=col-Ef;

clear col

Eshift = 0;
```

```matlab
for ii=1:Ntotal

    if A(ii)<0

        A(ii)=A(ii)-Eshift;

    else

        A(ii)=A(ii)+Eshift;

    end

end
%%%%


for ix=1:Nx

for iy=1:Ny

Ek(iy,:,ix)=A(1+(iy-1)*Nb+(ix-1)*Ny*Nb:(iy*Nb)+((ix-1)*Ny*Nb));

end

end

clear A

ME=zeros(1,Ne);

ky=0:kymax/(Ny-1):kymax;

dky=ky(2)-ky(1);


T=zeros(Nx,Ne);

for Iky=1:Ny-1

Ekk = squeeze(Ek(Iky,:,:))';

for jj = 1:Nx-1

[Iky jj]

id=(Iky-1)*Nx + jj;

index(id)=1;
```

```matlab
for hh = 1:Ne

for ii = 1:Nb

if ((Ekk(jj,ii) < E(hh)) && (Ekk(jj+1,ii)> E(hh)))

% for conduction band

|| ((Ekk(jj,ii) > E(hh)) && (Ekk(jj+1,ii)< E(hh)))

% for valence band

T(Iky,hh) = T(Iky,hh) + 1;

end;

end;

end;

end;

end;


for IE=1:Ne

    ME(IE)=pre_factor*(sum(squeeze(T(:,IE))*dky));

end


ME_3D = ME/Lz;  % in unit of /m^2 %%
save ME_Material E Ne Emin Emax ME ME_3D
```

The EIGENVAL file that is used as input for the script above should contain all the k-points that are sampled over in the irreducible Brillouin zone or the full Brillouin zone. The MATLAB friendly mat file that is saved at the end has an array of energy and the density of modes for the material. This energy versus density of modes relation can now be used to compute the properties of the material in linear response.

Bibliography

[1] D. Wickramaratne, F. Zahid, and R. K. Lake, "Electronic and thermoelectric properties of few-layer transition metal dichalcogenides," *The Journal of Chemical Physics*, vol. 140, no. 12, p. 124710, 2014.

[2] R. Samnakay, D. Wickramaratne, T. Pope, R. K. Lake, T. T. Salguero, and A. A. Balandin, "The zone-folded phonons and the commensurate–incommensurate charge-density-wave transition in 1T-TaSe2 thin films," *Nano Letters*, 2015.

[3] K. Bronsema, J. De Boer, and F. Jellinek, "On the structure of molybdenum diselenide and disulfide," *Zeitschrift fur anorganische und allgemeine Chemie*, vol. 540, no. 9-10, pp. 15–17, 2004.

[4] W. Schutte, J. D. Boer, and F. Jellinek, "Crystal structures of tungsten disulfide and diselenide," *Journal of Solid State Chemistry*, vol. 70, no. 2, pp. 207–209, 1987. [Online]. Available: http://www.sciencedirect.com/science/article/pii/0022459687900570

[5] K. K. Kam and B. A. Parkinson, "Detailed photocurrent spectroscopy of the semiconducting group vib transition metal dichalcogenides," *The Journal of*

Physical Chemistry, vol. 86, no. 4, pp. 463–467, 1982. [Online]. Available: http://pubs.acs.org/doi/abs/10.1021/j100393a010

[6] H. Zeng, G.-B. Liu, J. Dai, Y. Yan, B. Zhu, R. He, L. Xu, S. Xu, X. Chen, and X. Cui, "Optical signature of symmetry variations and spin-valley coupling in atomically thin tungsten dichalcogenides," *Nature Scientific Reports*, vol. 3, 2013.

[7] A. Kuhn, A. Chevy, and R. Chevalier, "Refinement of the 2H GaS-type," *Acta Crystallographica Section B: Structural Crystallography and Crystal Chemistry*, vol. 32, no. 3, pp. 983–984, 1976.

[8] A. Kuhn, C. A, and R. Chevalier, "Crystal structure and interatomic distances in GaSe," *Physica Status Solidi (a)*, vol. 31, no. 2, pp. 469–475, 1975.

[9] C. De Blasi, G. Micocci, S. Mongelli, and A. Tepore, "Large InSe single crystals grown from stoichiometric and non-stoichiometric melts," *Journal of Crystal Growth*, vol. 57, no. 3, pp. 482–486, 1982.

[10] S. Lei, L. Ge, S. Najmaei, A. George, R. Kappera, J. Lou, M. Chhowalla, H. Yamaguchi, G. Gupta, R. Vajtai, A. Mohite, and P. Ajayan, "Evolution of the electronic band structure and efficient photo-detection in atomic layers of InSe," *ACS Nano*, 2014.

[11] S. Nakajima, "The crystal structure of Bi2Te3-xSex," *Journal of Physics and Chemistry of Solids*, vol. 24, no. 3, pp. 479–485, 1963.

[12] T. Ohta, A. Bostwick, T. Seyller, K. Horn, and E. Rotenberg, "Controlling the electronic structure of bilayer graphene," *Science*, vol. 313, pp. 951 – 954, 2006.

[13] K. Rossnagel, "On the origin of charge-density waves in select layered transition-metal dichalcogenides," *Journal of Physics: Condensed Matter*, vol. 23, no. 21, p. 213001, 2011.

[14] E. Bjerkelund and A. Kjekshus, "On the structural properties of the TaSe2 phase," *Acta Chemica Scandinavica*, vol. 21, no. 2, pp. 513–526, 1967.

[15] J. A. Wilson, F. Di Salvo, and S. Mahajan, "Charge-density waves and super-lattices in the metallic layered transition metal dichalcogenides," *Advances in Physics*, vol. 24, no. 2, pp. 117–201, 1975.

[16] M. Chhowalla, H. S. Shin, G. Eda, L.-J. Li, K. P. Loh, and H. Zhang, "The chemistry of two-dimensional layered transition metal dichalcogenide nanosheets," *Nature chemistry*, vol. 5, no. 4, pp. 263–275, 2013.

[17] International Technology Roadmap for Semiconductors, Process Integration, Devices, and Structures, 2003 ed., p. 12.

[18] G. Fiori, F. Bonaccorso, G. Iannaccone, T. Palacios, D. Neumaier, A. Seabaugh, S. K. Banerjee, and L. Colombo, "Electronics based on two-dimensional materials," *Nature nanotechnology*, vol. 9, no. 10, pp. 768–779, 2014.

[19] V. V. Zhirnov, R. K. C. III, J. A. Hutchby, and G. I. Bourianoff, "Limits to binary logic switch scaling - a gedanken model," *Proc. IEEE*, vol. 91, no. 11, pp. 1934 – 1939, 2003.

[20] Q. H. Wang, K. Kalantar-Zadeh, A. Kis, J. N. Coleman, and M. S. Strano, "Electronics and optoelectronics of two-dimensional transition metal dichalcogenides," *Nature Nanotech.*, vol. 7, pp. 699–712, 2012.

[21] A. Geim and I. Grigorieva, "Van der waals heterostructures," *Nature*, vol. 499, pp. 419–425, 2013. [Online]. Available: http://www.nature.com/nature/journal/v499/n7459/abs/nature12385.html

[22] A. Koma, "Van der waals epitaxy a new epitaxial growth method for a highly lattice-mismatched system," *Thin Solid Films*, vol. 216, no. 1, pp. 72–76, 1992.

[23] Y. Alaskar, S. Arafin, D. Wickramaratne, M. A. Zurbuchen, L. He, J. McKay, Q. Lin, M. S. Goorsky, R. K. Lake, and K. L. Wang, "Towards van der waals epitaxial growth of GaAs on Si using a graphene buffer layer," *Advanced Functional Materials*, vol. 24, no. 42, pp. 6629–6638, 2014.

[24] Y. Huang, E. Sutter, J. T. Sadowski, M. Cotlet, O. L. Monti, D. A. Racke, M. R. Neupane, D. Wickramaratne, R. K. Lake, B. A. Parkinson *et al.*, "Tin Disulfide - an emerging layered metal dichalcogenide semiconductor: Materials properties and device characteristics," *ACS nano*, vol. 8, no. 10, pp. 10 743–10 755, 2014.

[25] Y. Kubota, K. Watanabe, O. Tsuda, and T. Taniguchi, "Deep ultraviolet light-emitting hexagonal boron nitride synthesized at atmospheric pressure," *Science*, vol. 317, no. 5840, pp. 932–934, 2007.

[26] T. Ueno, H. Yamamoto, K. Saiki, and A. Koma, "Van der waals epitaxy of metal dihalide," *Applied surface science*, vol. 113, pp. 33–37, 1997.

[27] R. W. Keyes, "The electrical properties of black phosphorus," *Physical Review*, vol. 92, no. 3, p. 580, 1953.

[28] M. Naguib, V. N. Mochalin, M. W. Barsoum, and Y. Gogotsi, "25th anniversary article: Mxenes: A new family of two-dimensional materials," *Advanced Materials*, vol. 26, no. 7, pp. 992–1005, 2014.

[29] P. Vogt, P. De Padova, C. Quaresima, J. Avila, E. Frantzeskakis, M. C. Asensio, A. Resta, B. Ealet, and G. Le Lay, "Silicene: compelling experimental evidence for graphenelike two-dimensional silicon," *Physical review letters*, vol. 108, no. 15, p. 155501, 2012.

[30] Z. Ni, Q. Liu, K. Tang, J. Zheng, J. Zhou, R. Qin, Z. Gao, D. Yu, and J. Lu, "Tunable bandgap in silicene and germanene," *Nano letters*, vol. 12, no. 1, pp. 113–118, 2011.

[31] R. Friend and A. Yoffe, "Electronic properties of intercalation complexes of the transition metal dichalcogenides," *Advances in Physics*, vol. 36, no. 1, pp. 1–94, 1987.

[32] R. A. Klemm, *Layered Superconductors*. Oxford University Press, 2011, vol. 153.

[33] M. S. Whittingham, "Chemistry of intercalation compounds: metal guests in chalcogenide hosts," *Progress in Solid State Chemistry*, vol. 12, no. 1, pp. 41–99, 1978.

[34] L. Mattheiss, "Band structures of transition-metal-dichalcogenide layer compounds," *Physical Review B*, vol. 8, no. 8, p. 3719, 1973.

[35] V. Podzorov, M. Gershenson, C. Kloc, R. Zeis, and E. Bucher, "High-mobility field-effect transistors based on transition metal dichalcogenides," *Applied Physics Letters*, vol. 84, no. 17, pp. 3301–3303, 2004.

[36] A. Ayari, E. Cobas, O. Ogundadegbe, and M. S. Fuhrer, "Realization and electrical characterization of ultrathin crystals of layered transition-metal

dichalcogenides," *Journal of Applied Physics*, vol. 101, no. 1, p. 014507, 2007. [Online]. Available: http://link.aip.org/link/?JAP/101/014507/1

[37] B. Radisavljevic, A. Radenovic, J. Brivio, V. Giacometti, and A. Kis, "Single-layer MoS2 transistors," *Nature Nanotechnology*, vol. 6, pp. 147 – 150, 2011. [Online]. Available: http://www.nature.com/nnano/journal/v6/n3/abs/nnano.2010.279.html

[38] A. Splendiani, L. Sun, Y. Zhang, T. Li, J. Kim, C.-Y. Chim, G. Galli, and F. Wang, "Emerging photoluminescence in monolayer MoS2," *Nano Letters*, vol. 10, no. 4, pp. 1271–1275, 2010, pMID: 20229981. [Online]. Available: http://pubs.acs.org/doi/abs/10.1021/nl903868w

[39] K. F. Mak, C. Lee, J. Hone, J. Shan, and T. F. Heinz, "Atomically thin MoS2: A new direct-gap semiconductor," *Phys. Rev. Lett.*, vol. 105, p. 136805, Sep 2010. [Online]. Available: http://link.aps.org/doi/10.1103/PhysRevLett.105.136805

[40] A. D. Yoffe, "Layer compounds," *Annual Review of Materials Science*, vol. 3, no. 1, pp. 147–170, 1973.

[41] M. S. Dresselhaus, G. Chen, M. Y. Tang, R. G. Yang, H. Lee, D. Z. Wang, Z. F. Ren, J.-P. Fleurial, and P. Gogna, "New directions for low-dimensional thermoelectric materials," *Advanced Materials*, vol. 19, no. 8, pp. 1043–1053, 2007. [Online]. Available: http://dx.doi.org/10.1002/adma.200600527

[42] C. J. Vineis, A. Shakouri, A. Majumdar, and M. G. Kanatzidis, "Nanostructured thermoelectrics: big efficiency gains from small features," *Advanced Materials*, vol. 22, no. 36, pp. 3970–3980, 2010.

[43] L. D. Hicks and M. S. Dresselhaus, "Effect of quantum-well structures on the thermoelectric figure of merit," *Phys. Rev. B*, vol. 47, pp. 12 727–12 731, May 1993. [Online]. Available: http://link.aps.org/doi/10.1103/PhysRevB.47.12727

[44] F. Zahid, L. Liu, Y. Zhu, J. Wang, and H. Guo, "A generic tight-binding model for monolayer, bilayer and bulk MoS2," *AIP Advances*, vol. 3, no. 5, p. 052111, 2013. [Online]. Available: http://link.aip.org/link/?ADV/3/052111/1

[45] J. Maassen and M. Lundstrom, "A computational study of the thermoelectric performance of ultrathin Bi2Te3 films," *Applied Physics Letters*, vol. 102, no. 9, p. 093103, 2013. [Online]. Available: http://link.aip.org/link/?APL/102/093103/1

[46] G. Grüner, "The dynamics of charge-density waves," *Rev. Mod. Phys.*, vol. 60, no. 4, pp. 1129–1181, Oct 1988.

[47] K. Rossnagel, L. Kipp, and M. Skibowski, "Charge-density-wave phase transition in $1T - \mathrm{TiSe_2}$: excitonic insulator versus band-type jahn-teller mechanism," *Phys. Rev. B*, vol. 65, p. 235101, May 2002. [Online]. Available: http://link.aps.org/doi/10.1103/PhysRevB.65.235101

[48] K. Rossnagel, E. Rotenberg, H. Koh, N. V. Smith, and L. Kipp, "Fermi surface, charge-density-wave gap, and kinks in $2H$-TaSe$_2$," *Phys. Rev. B*, vol. 72, p. 121103, Sep 2005. [Online]. Available: http://link.aps.org/doi/10.1103/PhysRevB.72.121103

[49] L. Perfetti, P. Loukakos, M. Lisowski, U. Bovensiepen, H. Berger, S. Biermann, P. Cornaglia, A. Georges, and M. Wolf, "Time evolution of the electronic structure of 1T-TaS2 through the insulator-metal transition," *Physical review letters*, vol. 97, no. 6, p. 067402, 2006.

[50] C. Arguello, S. Chockalingam, E. Rosenthal, L. Zhao, C. Gutiérrez, J. Kang, W. Chung, R. Fernandes, S. Jia, A. Millis *et al.*, "Visualizing the charge density wave transition in 2H-NbSe2 in real space," *Physical Review B*, vol. 89, no. 23, p. 235115, 2014.

[51] J. Smith, J. Tsang, and M. Shafer, "Raman spectra of several layer compounds with charge density waves," *Solid State Communications*, vol. 19, no. 4, pp. 283–286, 1976.

[52] M. Yoshida, Y. Zhang, J. Ye, R. Suzuki, Y. Imai, S. Kimura, A. Fujiwara, and Y. Iwasa, "Controlling charge-density-wave states in nano-thick crystals of 1T-TaS2," *Scientific reports*, vol. 4, 2014.

[53] A. Thompson, R. Gamble, and J. Revelli, "Transitions between semiconducting and metallic phases in 1T-TaS2," *Solid State Communications*, vol. 9, no. 13, pp. 981–985, 1971.

[54] P. Hohenberg and W. Kohn, "Inhomogeneous electron gas," *Physical review*, vol. 136, no. 3B, p. B864, 1964.

[55] W. Kohn and L. J. Sham, "Self-consistent equations including exchange and correlation effects," *Physical Review*, vol. 140, no. 4A, p. A1133, 1965.

[56] M. C. Payne, M. P. Teter, D. C. Allan, T. Arias, and J. Joannopoulos, "Iterative minimization techniques for ab initio total-energy calculations: molecular dynamics and conjugate gradients," *Reviews of Modern Physics*, vol. 64, no. 4, p. 1045, 1992.

[57] S. Baroni, S. De Gironcoli, A. Dal Corso, and P. Giannozzi, "Phonons and related crystal properties from density-functional perturbation theory," *Reviews of Modern Physics*, vol. 73, no. 2, p. 515, 2001.

[58] Y. Yoon, K. Ganapathi, and S. Salahuddin, "How good can monolayer MoS2 transistors be?" *Nano Letters*, vol. 11, no. 9, pp. 3768–3773, 2011. [Online]. Available: http://pubs.acs.org/doi/abs/10.1021/nl2018178

[59] H. Fang, S. Chuang, T. C. Chang, K. Takei, T. Takahashi, and A. Javey, "High-performance single layered WSe2 p-fets with chemically doped contacts," *Nano Letters*, vol. 12, no. 7, pp. 3788–3792, 2012.

[60] K. Alam and R. K. Lake, "Monolayer MoS_2 transistors beyond the technology road map," *IEEE Trans. Electron Devices*, vol. 59, no. 12, p. 3250, 2012.

[61] A. N. Han Liu and P. Ye, "Channel length scaling of MoS_2 mosfets," *ACS Nano*, vol. 6, no. 10, pp. 8563–8569, 2012.

[62] T. Li and G. Galli, "Electronic properties of MoS2 nanoparticles," *The Journal of Physical Chemistry C*, vol. 111, no. 44, pp. 16 192–16 196, 2007. [Online]. Available: http://pubs.acs.org/doi/abs/10.1021/jp075424v

[63] D. Xiao, G.-B. Liu, W. Feng, X. Xu, and W. Yao, "Coupled spin and valley physics in monolayers of MoS_2 and other group-VI dichalcogenides," *Phys. Rev. Lett.*, vol. 108, p. 196802, May 2012. [Online]. Available: http://link.aps.org/doi/10.1103/PhysRevLett.108.196802

[64] K. S. Novoselov and A. H. C. Neto, "Two-dimensional crystals-based heterostructures: materials with tailored properties," *Physica Scripta*, vol. 2012,

no. T146, p. 014006, 2012. [Online]. Available: http://stacks.iop.org/1402-4896/2012/i=T146/a=014006

[65] M. Xu, T. Liang, M. Shi, and H. Chen, "Graphene-like two-dimensional materials," *Chemical Reviews*, vol. 113, no. 5, pp. 3766–3798, 2013. [Online]. Available: http://pubs.acs.org/doi/abs/10.1021/cr300263a

[66] S. Z. Butler, S. M. Hollen, L. Cao, Y. Cui, J. A. Gupta, H. R. Gutirrez, T. F. Heinz, S. S. Hong, J. Huang, A. F. Ismach, E. Johnston-Halperin, M. Kuno, V. V. Plashnitsa, R. D. Robinson, R. S. Ruoff, S. Salahuddin, J. Shan, L. Shi, M. G. Spencer, M. Terrones, W. Windl, and J. E. Goldberger, "Progress, challenges, and opportunities in two-dimensional materials beyond graphene," *ACS Nano*, vol. 7, no. 4, pp. 2898–2926, 2013. [Online]. Available: http://pubs.acs.org/doi/abs/10.1021/nn400280c

[67] Y. Sun, H. Cheng, S. Gao, Q. Liu, Z. Sun, C. Xiao, C. Wu, S. Wei, and Y. Xie, "Atomically thick bismuth selenide freestanding single layers achieving enhanced thermoelectric energy harvesting," *Journal of the American Chemical Society*, vol. 134, no. 50, pp. 20 294–20 297, 2012. [Online]. Available: http://pubs.acs.org/doi/abs/10.1021/ja3102049

[68] V. Goyal, D. Teweldebrhan, and A. A. Balandin, "Mechanically-exfoliated stacks of thin films of Bi2Te3 topological insulators with enhanced thermoelectric performance," *Applied Physics Letters*, vol. 97, no. 13, p. 133117, 2010. [Online]. Available: http://link.aip.org/link/?APL/97/133117/1

[69] P. Ghaemi, R. S. K. Mong, and J. E. Moore, "In-plane transport and enhanced thermoelectric performance in thin films of the topological insulators

Bi$_2$Te$_3$ and Bi$_2$Se$_3$," *Phys. Rev. Lett.*, vol. 105, p. 166603, Oct 2010. [Online]. Available: http://link.aps.org/doi/10.1103/PhysRevLett.105.166603

[70] F. Zahid and R. Lake, "Thermoelectric properties of Bi2Te3 atomic quintuple thin films," *Applied Physics Letters*, vol. 97, no. 21, p. 212102, 2010. [Online]. Available: http://link.aip.org/link/?APL/97/212102/1

[71] F.Zahid and R.K.Lake, Unpublished.

[72] A. Amara, Y. Frongillo, M. J. Aubin, S. Jandl, J. M. Lopez-Castillo, and J. P. Jay-Gerin, "Thermoelectric power of TiS$_2$," *Phys. Rev. B*, vol. 36, pp. 6415–6419, Oct 1987. [Online]. Available: http://link.aps.org/doi/10.1103/PhysRevB.36.6415

[73] H. Imai, Y. Shimakawa, and Y. Kubo, "Large thermoelectric power factor in TiS$_2$ crystal with nearly stoichiometric composition," *Phys. Rev. B*, vol. 64, p. 241104, Dec 2001. [Online]. Available: http://link.aps.org/doi/10.1103/PhysRevB.64.241104

[74] H. Guo, T. Yang, P. Tao, Y. Wang, and Z. Zhang, "High pressure effect on structure, electronic structure, and thermoelectric properties of MoS2," *Journal of Applied Physics*, vol. 113, no. 1, p. 013709, 2013. [Online]. Available: http://link.aip.org/link/?JAP/113/013709/1

[75] M. Buscema, M. Barkelid, V. Zwiller, H. S. J. van der Zant, G. A. Steele, and A. Castellanos-Gomez, "Large and tunable photothermoelectric effect in single-layer MoS2," *Nano Letters*, vol. 0, no. 0, p. null, 0. [Online]. Available: http://pubs.acs.org/doi/abs/10.1021/nl303321g

[76] W. Huang, H. Da, and G. Liang, "Thermoelectric performance of MX2(M=Mo,W;X=S,Se) monolayers," *Journal of Applied Physics*, vol. 113, no. 10, p. 104304, 2013. [Online]. Available: http://link.aip.org/link/?JAP/113/104304/1

[77] C. Lee, J. Hong, M.-H. Whangbo, and J. H. Shim, "Enhancing the thermoelectric properties of layered transition-metal dichalcogenides 2H-MQ2 (M = Mo, W; Q = S, Se, Te) by layer mixing: Density functional investigation," *Chemistry of Materials*, vol. 25, no. 18, pp. 3745–3752, 2013. [Online]. Available: http://pubs.acs.org/doi/abs/10.1021/cm402281n

[78] P. E. Blöchl, "Projector augmented-wave method," *Phys. Rev. B*, vol. 50, no. 24, pp. 17 953–17 979, 1994.

[79] J. P. Perdew, K. Burke, and M. Ernzerhof, "Generalized Gradient Approximation Made Simple," *Phys. Rev. Lett.*, vol. 77, pp. 3865–3868, 1996.

[80] M. Ernzerhof and G. E. Scuseria, "Assessment of the Perdew-Burke-Ernzerhof exchange-correlation functional," *J. Chem. Phys.*, vol. 110, pp. 5029–5036, 1999.

[81] G. Kresse and J. Hafner, "Ab initio molecular dynamics for open-shell transition metals," *Phys. Rev. B*, vol. 48, no. 17, pp. 13 115–13 118, 1993.

[82] G. Kresse and J. Furthmuller, "Efficiency of ab-initio total energy calculations for metals and semiconductors using a plane-wave basis set," *Comput. Mater. Sci.*, vol. 6, no. 1, pp. 15–50, 1996.

[83] S. Grimme, "Semiempirical GGA-type density functional constructed with a long-range dispersion correction," *Journal of Computational*

Chemistry, vol. 27, no. 15, pp. 1787–1799, 2006. [Online]. Available: http://dx.doi.org/10.1002/jcc.20495

[84] J. Heyd, G. E. Scuseria, and M. Ernzerhof, "Hybrid functionals based on a screened coulomb potential," *The Journal of Chemical Physics*, vol. 118, no. 18, pp. 8207–8215, 2003. [Online]. Available: http://scitation.aip.org/content/aip/journal/jcp/118/18/10.1063/1.1564060

[85] C. Jeong, R. Kim, M. Luisier, S. Datta, and M. Lundstrom, "On landauer versus boltzmann and full band versus effective mass evaluation of thermoelectric transport coefficients," *Journal of Applied Physics*, vol. 107, no. 2, p. 023707, 2010. [Online]. Available: http://link.aip.org/link/?JAP/107/023707/1

[86] A. Paul, S. Salamat, C. Jeong, G. Klimeck, and M. Lundstrom, "An efficient algorithm to calculate intrinsic thermoelectric parameters based on Landauer approach," *Journal of Computational Electronics*, vol. 11, no. 1, pp. 56–66, 2012.

[87] R. Kim, S. Datta, and M. S. Lundstrom, "Influence of dimensionality on thermoelectric device performance," *Journal of Applied Physics*, vol. 105, no. 3, p. 034506, 2009. [Online]. Available: http://link.aip.org/link/?JAP/105/034506/1

[88] R. Mansfield and S. A. Salam, "Electrical properties of molybdenite," *Proceedings of the Physical Society. Section B*, vol. 66, no. 5, p. 377, 1953. [Online]. Available: http://stacks.iop.org/0370-1301/66/i=5/a=305

[89] S. Thakurta and A. Dutta, "Electrical conductivity, thermoelectric power and hall effect in p-type molybdenite (MoS2) crystal," *Journal of Physics and Chemistry of Solids*, vol. 44, no. 5, pp. 407–416, 1983.

[90] K. Kaasbjerg, K. S. Thygesen, and K. W. Jacobsen, "Phonon-limited mobility in n-type single-layer MoS_2 from first principles," *Phys. Rev. B*, vol. 85, p. 115317, Mar 2012. [Online]. Available: http://link.aps.org/doi/10.1103/PhysRevB.85.115317

[91] V. Varshney, S. S. Patnaik, C. Muratore, A. K. Roy, A. A. Voevodin, and B. L. Farmer, "MD simulations of molybdenum disulphide (MoS2): Force-field parameterization and thermal transport behavior," *Computational Materials Science*, vol. 48, no. 1, pp. 101 – 108, 2010. [Online]. Available: http://www.sciencedirect.com/science/article/pii/S0927025609004583

[92] C. Chiritescu, D. G. Cahill, N. Nguyen, D. Johnson, A. Bodapati, P. Keblinski, and P. Zschack, "Ultralow thermal conductivity in disordered, layered WSe2 crystals," *Science*, vol. 315, no. 5810, pp. 351–353, 2007.

[93] H. Jiang, "Electronic band structures of molybdenum and tungsten dichalcogenides by the gw approach," *The Journal of Physical Chemistry C*, vol. 116, no. 14, pp. 7664–7671, 2012. [Online]. Available: http://pubs.acs.org/doi/abs/10.1021/jp300079d

[94] R. Coehoorn, C. Haas, J. Dijkstra, C. J. F. Flipse, R. A. de Groot, and A. Wold, "Electronic structure of $MoSe_2$, MoS_2, and WSe_2. I. band-structure calculations and photoelectron spectroscopy," *Phys. Rev. B*, vol. 35, pp. 6195–6202, Apr 1987. [Online]. Available: http://link.aps.org/doi/10.1103/PhysRevB.35.6195

[95] Y. Ding, Y. Wang, J. Ni, L. Shi, S. Shi, and W. Tang, "First principles study of structural, vibrational and electronic properties of graphene-like MX2 (M=Mo, Nb, W, Ta; X=S, Se, Te) monolayers," *Physica B: Condensed*

Matter, vol. 406, no. 11, pp. 2254 – 2260, 2011. [Online]. Available: http://www.sciencedirect.com/science/article/pii/S092145261100265

[96] A. Kuc, N. Zibouche, and T. Heine, "Influence of quantum confinement on the electronic structure of the transition metal sulfide $T\mathrm{S}_2$," *Phys. Rev. B*, vol. 83, p. 245213, Jun 2011.

[97] L. Liu, S. Bala Kumar, Y. Ouyang, and J. Guo, "Performance limits of monolayer transition metal dichalcogenide transistors," *Electron Devices, IEEE Transactions on*, vol. 58, no. 9, pp. 3042–3047, 2011.

[98] A. Ramasubramaniam, "Large excitonic effects in monolayers of molybdenum and tungsten dichalcogenides," *Phys. Rev. B*, vol. 86, p. 115409, Sep 2012. [Online]. Available: http://link.aps.org/doi/10.1103/PhysRevB.86.115409

[99] T. Cheiwchanchamnangij and W. R. Lambrecht, "Quasiparticle band structure calculation of monolayer, bilayer, and bulk MoS_2," *Phys. Rev. B*, vol. 85, p. 205302, May 2012. [Online]. Available: http://link.aps.org/doi/10.1103/PhysRevB.85.205302

[100] H. Shi, H. Pan, Y.-W. Zhang, and B. I. Yakobson, "Quasiparticle band structures and optical properties of strained monolayer MoS_2 and WS_2," *Phys. Rev. B*, vol. 87, p. 155304, Apr 2013. [Online]. Available: http://link.aps.org/doi/10.1103/PhysRevB.87.155304

[101] F. Zahid, L. Liu, Y. Zhu, J. Wang, and H. Guo, "A generic tight-binding model for monolayer, bilayer and bulk MoS2," *AIP Advances*, vol. 3, no. 5, p. 052111, 2013. [Online]. Available: http://link.aip.org/link/?ADV/3/052111/1

[102] P. Pichanusakorn and P. R. Bandaru, "The optimal seebeck coefficient for obtaining the maximum power factor in thermoelectrics," *Applied Physics Letters*, vol. 94, no. 22, pp. –, 2009. [Online]. Available: http://scitation.aip.org/content/aip/journal/apl/94/22/10.1063/1.3147186

[103] W. Li, J. Carrete, and N. Mingo, "Thermal conductivity and phonon linewidths of monolayer MoS2 from first principles," *Applied Physics Letters*, vol. 103, no. 25, pp. –, 2013. [Online]. Available: http://scitation.aip.org/content/aip/journal/apl/103/25/10.1063/1.4850995

[104] Y. Cai, J. Lan, G. Zhang, and Y.-W. Zhang, "Lattice vibrational modes and phonon thermal conductivity of monolayer MoS2," *Phys. Rev. B*, vol. 89, p. 035438, Jan 2014. [Online]. Available: http://link.aps.org/doi/10.1103/PhysRevB.89.035438

[105] C. Muratore, V. Varshney, J. J. Gengler, J. J. Hu, J. E. Bultman, T. M. Smith, P. J. Shamberger, B. Qiu, X. Ruan, A. K. Roy, and A. A. Voevodin, "Cross-plane thermal properties of transition metal dichalcogenides," *Applied Physics Letters*, vol. 102, no. 8, pp. –, 2013. [Online]. Available: http://scitation.aip.org/content/aip/journal/apl/102/8/10.1063/1.4793203

[106] R. Yan, J. R. Simpson, S. Bertolazzi, J. Brivio, M. Watson, X. Wu, A. Kis, T. Luo, A. R. Hight Walker, and H. G. Xing, "Thermal conductivity of monolayer molybdenum disulfide obtained from temperature-dependent raman spectroscopy," *ACS Nano*, vol. 8, no. 1, pp. 986–993, 2014. [Online]. Available: http://pubs.acs.org/doi/abs/10.1021/nn405826k

[107] H.-P. Komsa and A. V. Krasheninnikov, "Electronic structures and optical properties of realistic transition metal dichalcogenide heterostructures from first principles," *Physical Review B*, vol. 88, no. 8, p. 085318, 2013.

[108] T. Georgiou, R. Jalil, B. Belle, L. Britnell, R. Gorbachev, S. Morozov, Y.Kim, A. Gholina, S. Haigh, O. Makarovsky, L. Ponomarenko, A. Geim, K. Novoselov, , and A. Mischenko, "Vertical field-effect transistor based on graphene-ws2 heterostructures for flexible and transparent electronics," *Nature Nanotech.*, vol. 8, pp. 100–103, 2013.

[109] H. Yuan, M. S. Bahramy, K. Morimoto, S. Wu, K. Nomura, B.-J. Yang, H. Shimotani, R. Suzuki, M. Toh, C. Kloc *et al.*, "Zeeman-type spin splitting controlled by an electric field," *Nature Physics*, vol. 9, no. 9, pp. 563–569, 2013.

[110] S. Wu, J. S. Ross, G.-B. Liu, G. Aivazian, A. Jones, Z. Fei, W. Zhu, D. Xiao, W. Yao, D. Cobden *et al.*, "Electrical tuning of valley magnetic moment through symmetry control in bilayer MoS2," *Nature Physics*, vol. 9, no. 3, pp. 149–153, 2013.

[111] Y. Zhan, Z. Liu, S. Najmaei, P. M. Ajayan, and J. Lou, "Large-area vapor-phase growth and characterization of MoS2 atomic layers on a SiO2/ substrate," *Small*, vol. 8, no. 7, pp. 966–971, 2012. [Online]. Available: http://dx.doi.org/10.1002/smll.201102654

[112] Y. Shi, W. Zhou, A.-Y. Lu, W. Fang, Y.-H. Lee, A. L. Hsu, S. M. Kim, K. K. Kim, H. Y. Yang, L.-J. Li, J.-C. Idrobo, and J. Kong, "van der waals epitaxy of MoS2 layers using graphene as growth templates," *Nano Letters*, vol. 12, no. 6, pp. 2784–2791, 2012. [Online]. Available: http://pubs.acs.org/doi/abs/10.1021/nl204562j

[113] G. Trambly de Laissardiere, D. Mayou, and L. Magaud, "Localization of dirac electrons in rotated graphene bilayers," *Nano letters*, vol. 10, no. 3, pp. 804–808, 2010.

[114] J. Hass, F. Varchon, J.-E. Millan-Otoya, M. Sprinkle, N. Sharma, W. A. de Heer, C. Berger, P. N. First, L. Magaud, and E. H. Conrad, "Why multilayer graphene on 4H-SiC(000-1) behaves like a single sheet of graphene," *Physical Review Letters*, vol. 100, no. 12, p. 125504, 2008.

[115] J. He, K. Hummer, and C. Franchini, "Stacking effects on the electronic and optical properties of bilayer transition metal dichalcogenides MoS2, MoSe2, WS2, and WSe2," *Physical Review B*, vol. 89, no. 7, p. 075409, 2014.

[116] F. J. Crowne, M. Amani, A. G. Birdwell, M. L. Chin, T. P. ORegan, S. Najmaei, Z. Liu, P. M. Ajayan, J. Lou, and M. Dubey, "Blueshift of the a-exciton peak in folded monolayer 1H-MoS 2," *Physical Review B*, vol. 88, no. 23, p. 235302, 2013.

[117] A. van der Zande, J. Kunstmann, A. Chernikov, D. Chenet, Y. You, X. Zhang, P. Y. Huang, T. C. Berkelbach, L. Wang, F. Zhang *et al.*, "Tailoring the electronic structure in bilayer molybdenum disulfide via interlayer twist," *Nano Letters*, 2014.

[118] W.-T. Hsu, Z.-A. Zhao, L.-J. Li, C.-H. Chen, M.-H. Chiu, P.-S. Chang, Y.-C. Chou, and W.-H. Chang, "Second harmonic generation from artificially stacked transition metal dichalcogenide twisted bilayers," *ACS nano*, vol. 8, no. 3, pp. 2951–2958, 2014.

[119] K. Liu, L. Zhang, T. Cao, C. Jin, D. Qiu, Q. Zhou, A. Zettl, P. Yang, S. G. Louie, and F. Wang, "Evolution of interlayer coupling in twisted molybdenum disulfide bilayers," *Nature communications*, vol. 5, 2014.

[120] H. Terrones, F. López-Urías, and M. Terrones, "Novel hetero-layered materials with tunable direct band gaps by sandwiching different metal disulfides and diselenides," *Scientific reports*, vol. 3, 2013.

[121] J. Kang, J. Li, S.-S. Li, J.-B. Xia, and L.-W. Wang, "Electronic structural moiré pattern effects on MoS2/MoSe2 2d heterostructures," *Nano letters*, vol. 13, no. 11, pp. 5485–5490, 2013.

[122] P. Koskinen, I. Fampiou, and A. Ramasubramaniam, "Density-functional tight-binding simulations of curvature-controlled layer decoupling and band-gap tuning in bilayer MoS2," *Physical review letters*, vol. 112, no. 18, p. 186802, 2014.

[123] H. Fang, C. Battaglia, C. Carraro, S. Nemsak, B. Ozdol, J. S. Kang, H. A. Bechtel, S. B. Desai, F. Kronast, A. A. Unal *et al.*, "Strong interlayer coupling in van der waals heterostructures built from single-layer chalcogenides," *Proceedings of the National Academy of Sciences*, vol. 111, no. 17, pp. 6198–6202, 2014.

[124] N. Lu, H. Guo, L. Wang, X. Wu, and X. C. Zeng, "van der waals trilayers and superlattices: modification of electronic structures of MoS2 by intercalation," *Nanoscale*, vol. 6, no. 9, pp. 4566–4571, 2014.

[125] S. Shallcross, S. Sharma, E. Kandelaki, and O. Pankratov, "Electronic structure of turbostratic graphene," *Physical Review B*, vol. 81, no. 16, p. 165105, 2010.

[126] K. M. Habib, S. S. Sylvia, S. Ge, M. Neupane, and R. K. Lake, "The coherent interlayer resistance of a single, rotated interface between two stacks of ab graphite," *Applied Physics Letters*, vol. 103, no. 24, p. 243114, 2013.

[127] A. Tkatchenko, R. A. DiStasio Jr, R. Car, and M. Scheffler, "Accurate and efficient method for many-body van der waals interactions," *Physical review letters*, vol. 108, no. 23, p. 236402, 2012.

[128] T. Stauber, N. Peres, F. Guinea, and A. C. Neto, "Fermi liquid theory of a fermi ring," *Physical Review B*, vol. 75, no. 11, p. 115425, 2007.

[129] V. Zolyomi, N. Drummond, and V. Fal'ko, "Band structure and optical transitions in atomic layers of hexagonal gallium chalcogenides," *Physical Review B*, vol. 87, no. 19, p. 195403, 2013.

[130] V. Zolyomi, N. D. Drummond, and V. I. Fal'ko, "Electrons and phonons in single layers of hexagonal indium chalcogenides from ab initio calculations," *Phys. Rev. B*, vol. 89, p. 205416, May 2014. [Online]. Available: http://link.aps.org/doi/10.1103/PhysRevB.89.205416

[131] F. Zhang, B. Sahu, H. Min, and A. H. MacDonald, "Band structure of a b c-stacked graphene trilayers," *Physical Review B*, vol. 82, no. 3, p. 035409, 2010.

[132] A. Varlet, D. Bischoff, P. Simonet, K. Watanabe, T. Taniguchi, T. Ihn, K. Ensslin, M. Mucha-Kruczyński, and V. I. Fal'ko, "Anomalous sequence of quantum hall liquids revealing a tunable lifshitz transition in bilayer graphene," *Phys. Rev. Lett.*, vol. 113, p. 116602, Sep 2014. [Online]. Available: http://link.aps.org/doi/10.1103/PhysRevLett.113.116602

[133] Y. M. Blanter, M. Kaganov, A. Pantsulaya, and A. Varlamov, "The theory of electronic topological transitions," *Physics Reports*, vol. 245, no. 4, pp. 159–257, 1994.

[134] X. Wang, L. Wang, J. Liu, and L. Peng, "Camel-back band-induced power factor enhancement of thermoelectric lead-tellurium from boltzmann transport calculations," *Applied Physics Letters*, vol. 104, no. 13, p. 132106, 2014.

[135] H. Peng, N. Kioussis, and G. J. Snyder, "Elemental tellurium as a chiral p-type thermoelectric material," *Physical Review B*, vol. 89, no. 19, p. 195206, 2014.

[136] A. Takayama, T. Sato, S. Souma, and T. Takahashi, "Giant out-of-plane spin component and the asymmetry of spin polarization in surface rashba states of bismuth thin film," *Physical Review Letters*, vol. 106, no. 16, p. 166401, 2011.

[137] P. Hu, L. Wang, M. Yoon, J. Zhang, W. Feng, X. Wang, Z. Wen, J. C. Idrobo, Y. Miyamoto, D. B. Geohegan, and K. Xiao, "Highly responsive ultrathin GaS nanosheet photodetectors on rigid and flexible substrates," *Nano Letters*, vol. 13, no. 4, pp. 1649–1654, 2013.

[138] H. L. Zhuang and R. G. Hennig, "Single-layer group-III monochalcogenide photocatalysts for water splitting," *Chemistry of Materials*, vol. 25, no. 15, pp. 3232–3238, 2013.

[139] T. Cao, Z. Li, and S. G. Louie, "Tunable magnetism and half-metallicity in hole-doped monolayer GaSe," *arXiv preprint arXiv:1409.4112*, 2014.

[140] S. Wu, X. Dai, H. Yu, H. Fan, J. Hu, and W. Yao, "Magnetisms in p-type monolayer gallium chalcogenides (GaSe, GaS)," *arXiv preprint arXiv:1409.4733*, 2014.

[141] S. Lei, L. Ge, Z. Liu, S. Najmaei, G. Shi, G. You, J. Lou, R. Vajtai, and P. M. Ajayan, "Synthesis and photoresponse of large GaSe atomic layers," *Nano Letters*, vol. 13, no. 6, pp. 2777–2781, 2013.

[142] P. Hu, Z. Wen, L. Wang, P. Tan, and K. Xiao, "Synthesis of few-layer GaSe nanosheets for high performance photodetectors," *ACS Nano*, vol. 6, no. 7, pp. 5988–5994, 2012.

[143] D. J. Late, B. Liu, J. Luo, A. Yan, H. Matte, M. Grayson, C. Rao, and V. P. Dravid, "GaS and GaSe ultrathin layer transistors," *Advanced Materials*, vol. 24, no. 26, pp. 3549–3554, 2012.

[144] X. Li, M.-W. Lin, A. A. Puretzky, J. C. Idrobo, C. Ma, M. Chi, M. Yoon, C. M. Rouleau, I. I. Kravchenko, D. B. Geohegan, and K. Xiao, "Controlled vapor phase growth of single crystalline, two-dimensional GaSe crystals with high photoresponse," *Scientific reports*, vol. 4, 2014.

[145] M. Mahjouri-Samani, M. Tian, K. Wang, A. Boulesbaa, C. M. Rouleau, A. A. Puretzky, M. A. McGuire, B. R. Srijanto, K. Xiao, G. Eres, G. Duscher, and D. B. Geohegan, "Digital transfer growth of patterned 2D metal chalcogenides by confined nanoparticle evaporation," *ACS Nano*, 2014.

[146] Y. Saeed, N. Singh, and U. Schwingenschlögl, "Thickness and strain effects on the thermoelectric transport in nanostructured Bi2Se3," *Applied Physics Letters*, vol. 104, no. 3, p. 033105, 2014.

[147] H. Min, B. Sahu, S. K. Banerjee, and A. H. MacDonald, "Ab initio theory of gate induced gaps in graphene bilayers," *Phys. Rev. B*, vol. 75, no. 15, p. 155115, Apr 2007.

[148] G. D. Mahan and J. O. Sofo, *The Best Thermoelectric.* Washington, DC: National Academy of Sciences, 1996, vol. 93, pp. 7436 – 7439.

[149] J. P. Heremans, V. Jovovic, E. S. Toberer, A. Saramat, K. Kurosaki, A. Charoenphakdee, S. Yamanaka, and G. J. Snyder, "Enhancement of thermoelectric efficiency in PbTe by distortion of the electronic density of states," *Science*, vol. 321, no. 5888, pp. 554–557, 2008.

[150] J. P. Heremans, B. Wiendlocha, and A. M. Chamoire, "Resonant levels in bulk thermoelectric semiconductors," *Energy & Environmental Science*, vol. 5, no. 2, pp. 5510–5530, 2012.

[151] Y. M. Blanter, A. Varlamov, A. Pantsulaya, and D. Parsons, "Thermoelectric power and topological transitions in quasi-2d electron systems," *Soviet physics, JETP*, vol. 73, no. 4, pp. 688–692, 1991.

[152] G. J. Snyder and E. S. Toberer, "Complex thermoelectric materials," *Nature Materials*, vol. 7, no. 2, pp. 105–114, 2008.

[153] L. E. Bell, "Cooling, heating, generating power, and recovering waste heat with thermoelectric systems," *Science*, vol. 321, no. 5895, pp. 1457–1461, 2008.

[154] P. Wang and A. Bar-Cohen, "On-chip hot spot cooling using silicon thermoelectric microcoolers," *Journal of Applied Physics*, vol. 102, no. 3, p. 034503, 2007.

[155] A. Shakouri, "Recent developments in semiconductor thermoelectric physics and materials," *Materials Research*, vol. 41, no. 1, p. 399, 2011.

[156] Y. Pei, H. Wang, and G. Snyder, "Band engineering of thermoelectric materials," *Advanced Materials*, vol. 24, no. 46, pp. 6125–6135, 2012.

[157] J.-H. Lee, J. Wu, and J. C. Grossman, "Enhancing the thermo-electric power factor with highly mismatched isoelectronic doping," *Phys. Rev. Lett.*, vol. 104, p. 016602, Jan 2010. [Online]. Available: http://link.aps.org/doi/10.1103/PhysRevLett.104.016602

[158] M. Zebarjadi, K. Esfarjani, Z. Bian, and A. Shakouri, "Low-temperature thermoelectric power factor enhancement by controlling nanoparticle size distribution," *Nano Letters*, vol. 11, no. 1, pp. 225–230, 2011. [Online]. Available: http://pubs.acs.org/doi/abs/10.1021/nl103581z

[159] A. Balandin and K. L. Wang, "Effect of phonon confinement on the thermoelectric figure of merit of quantum wells," *Journal of Applied Physics*, vol. 84, no. 11, pp. 6149–6153, 1998. [Online]. Available: http://link.aip.org/link/?JAP/84/6149/1

[160] W. Kim, J. Zide, A. Gossard, D. Klenov, S. Stemmer, A. Shakouri, and A. Majumdar, "Thermal conductivity reduction and thermoelectric figure of merit increase by embedding nanoparticles in crystalline semiconductors," *Phys. Rev. Lett.*, vol. 96, p. 045901, Feb 2006. [Online]. Available: http://link.aps.org/doi/10.1103/PhysRevLett.96.045901

[161] L. D. Hicks and M. S. Dresselhaus, "Thermoelectric figure of merit of a one-dimensional conductor," *Phys. Rev. B*, vol. 47, pp. 16 631–16 634, Jun 1993. [Online]. Available: http://link.aps.org/doi/10.1103/PhysRevB.47.16631

[162] Y. Pei, X. Shi, A. LaLonde, H. Wang, L. Chen, and G. J. Snyder, "Convergence of electronic bands for high performance bulk thermoelectrics," *Nature*, vol. 473, no. 7345, pp. 66–69, 2011.

[163] J. R. Sootsman, D. Y. Chung, and M. G. Kanatzidis, "New and old concepts in thermoelectric materials," *Angewandte Chemie*, vol. 48, pp. 8616 – 8639, 2009.

[164] M. K. Fuccillo, Q. D. Gibson, M. N. Ali, L. M. Schoop, and R. J. Cava, "Correlated evolution of colossal thermoelectric effect and kondo insulating behavior," *APL Materials*, vol. 1, no. 6, pp. –, 2013. [Online]. Available: http://scitation.aip.org/content/aip/journal/aplmater/1/6/10.1063/1.4833055

[165] P. Sun, N. Oeschler, S. Johnsen, B. B. Iversen, and F. Steglich, "Huge thermoelectric power factor: FeSb2 versus FeAs2 and RuSb2," *Applied Physics Express*, vol. 2, no. 9, p. 091102, 2009. [Online]. Available: http://stacks.iop.org/1882-0786/2/i=9/a=091102

[166] Y. Zhang, M. S. Dresselhaus, Y. Shi, Z. Ren, and G. Chen, "High thermoelectric figure-of-merit in kondo insulator nanowires at low temperatures," *Nano Letters*, vol. 11, no. 3, pp. 1166–1170, 2011.

[167] J. P. Heremans, V. Jovovic, E. S. Toberer, A. Saramat, K. Kurosaki, A. Charoenphakdee, S. Yamanaka, and G. J. Snyder, "Enhancement of Thermoelectric Efficiency in PbTe by Distortion of the Electronic Density of States," *Science*, vol. 321, no. 5888, pp. 554–557, 2008. [Online]. Available: http://www.sciencemag.org/cgi/content/abstract/321/5888/554

[168] J. Yu, S. Mitrovic, D. Tham, J. Varghese, and J. Heath, "Reduction of thermal conductivity in phononic nanomesh structures," *Nature Nanotechnology*, vol. 5, pp. 718 – 721, 2010.

[169] I. Chowdhury, R. Prasher, K. Lofgreen, G. Chrysler, S. Narasimhan, R. Mahajan, D. Koester, R. Alley, and R. Venkatasubramanian, "On-chip cooling by

superlattice-based thin-film thermoelectrics," *Nature Nanotechnology*, vol. 4, no. 4, pp. 235–238, 2009.

[170] R. Venkatasubramanian, C. Watkins, D. Stokes, J. Posthill, and C. Caylor, "Energy harvesting for electronics with thermoelectric devices using nanoscale materials," in *Electron Devices Meeting, 2007. IEDM 2007. IEEE International.* IEEE, 2007, pp. 367–370.

[171] Z. Yan, G. Liu, J. M. Khan, and A. A. Balandin, "Graphene quilts for thermal management of high-power gan transistors," *Nature Communications*, vol. 3, p. 827, 2012.

[172] K. Wu, L. Rademaker, and J. Zaanen, "Bilayer excitons in two-dimensional nanostructures for greatly enhanced thermoelectric efficiency," *Physical Review Applied*, vol. 2, no. 5, p. 054013, 2014.

[173] R. Dhall, M. Neupane, D. Wickramaratne, M. Mecklenburg, Z. Li, C. Moore, R. K. Lake, and S. Cronin, "Bulk direct band gap $MoS2$ by plasma induced layer decoupling," *Advanced Materials, In Press*, 2014.

[174] H. Fang, C. Battaglia, C. Carraro, S. Nemsak, B. Ozdol, J. S. Kang, H. A. Bechtel, S. B. Desai, F. Kronast, A. A. Unal, G. Conti, C. Conlon, G. Palsson, M. Martin, A. Minor, C. Fadley, E. Yablonovitch, R. Maboudian, and A. Javey, "Strong interlayer coupling in van der waals heterostructures built from single-layer chalcogenides," *Proceedings of the National Academy of Sciences*, vol. 111, no. 17, pp. 6198–6202, 2014.

[175] S. Datta, *Quantum Transport Atom to Transistor*. Cambridge: Cambridge University Press, 2005.

[176] Y. A. Bychkov and E. I. Rashba, "Oscillatory effects and the magnetic susceptibility of carriers in inversion layers," *Journal of physics C: Solid state physics*, vol. 17, no. 33, p. 6039, 1984.

[177] K. Ishizaka, M. Bahramy, H. Murakawa, M. Sakano, T. Shimojima, T. Sonobe, K. Koizumi, S. Shin, H. Miyahara, A. Kimura, K. Miyamoto, T. Okuda, H. Namatame, M. Taniguchi, R. Arita, N. Nagaosa, K. Kobayashi, Y. Murakami, R. Kumai, Y. Kaneko, Y. Onosoe, and Y. Tokura, "Giant rashba-type spin splitting in bulk BiTeI," *Nature Materials*, vol. 10, no. 7, pp. 521–526, 2011.

[178] F. I. Ismailov, G. A. Akhundov, and O. R. Vernich, "Investigation of electrical conductivity and hall effect in GaSe single crystals," *Physica Status Solidi (b)*, vol. 17, no. 2, pp. K237–K240, 1966. [Online]. Available: http://dx.doi.org/10.1002/pssb.19660170269

[179] G. Micocci, R. Rella, P. Siciliano, and A. Tepore, "Investigation of electronic properties of gallium sulfide single crystals grown by iodine chemical transport," *Journal of Applied Physics*, vol. 68, no. 1, pp. 138–142, 1990.

[180] D. Krishna and P. Reddy, "Electrical conductivity, structure and hall effect measurements of InSe films," *Thin Solid Films*, vol. 105, no. 2, pp. 139 – 147, 1983. [Online]. Available: http://www.sciencedirect.com/science/article/pii/004060908390202X

[181] R. Mane and C. Lokhande, "Studies on structural, optical and electrical properties of indium sulfide thin films," *Materials Chemistry and Physics*, vol. 78, no. 1, pp. 15–17, 2003.

[182] R. A. Hoffman and D. Frankl, "Electrical transport properties of thin bismuth films," *Physical Review B*, vol. 3, no. 6, p. 1825, 1971.

[183] Y. S. Hor, A. Richardella, P. Roushan, Y. Xia, J. G. Checkelsky, A. Yazdani, M. Z. Hasan, N. P. Ong, and R. J. Cava, "*p*," *Phys. Rev. B*, vol. 79, p. 195208, May 2009. [Online]. Available: http://link.aps.org/doi/10.1103/PhysRevB.79.195208

[184] C.-R. Wang, W.-S. Lu, L. Hao, W.-L. Lee, T.-K. Lee, F. Lin, I.-C. Cheng, and J.-Z. Chen, "Enhanced thermoelectric power in dual-gated bilayer graphene," *Physical Review Letters*, vol. 107, no. 18, p. 186602, 2011.

[185] M. Alzhdanov, M. Nadzhafzade, and Z. Y. Seidov, "Thermal conductivity of gallium sulfide," *Physics of the Solid State*, vol. 41, no. 1, pp. 20–21, 1999.

[186] D. Spitzer, "Lattice thermal conductivity of semiconductors: A chemical bond approach," *Journal of Physics and Chemistry of Solids*, vol. 31, no. 1, pp. 19–40, 1970.

[187] L. Cheng, H. Liu, X. Tan, J. Zhang, J. Wei, H. Lv, J. Shi, and X. Tang, "Thermoelectric properties of a monolayer bismuth," *The Journal of Physical Chemistry C*, 2013.

[188] H. J. Goldsmid, *Introduction to Thermoelectricity.* Springer, 2009, vol. 121.

[189] A. A. Balandin, "Thermal properties of graphene and nanostructured carbon materials," *Nature Materials*, vol. 10, no. 8, pp. 569–581, 2011.

[190] B. Kong, S. Paul, M. B. Nardelli, and K. Kim, "First-principles analysis of lattice thermal conductivity in monolayer and bilayer graphene," *Physical Review B*, vol. 80, no. 3, p. 033406, 2009.

[191] S. Ghosh, W. Bao, D. L. Nika, S. Subrina, E. P. Pokatilov, C. N. Lau, and A. A. Balandin, "Dimensional crossover of thermal transport in few-layer graphene," *Nature Materials*, vol. 9, no. 7, pp. 555–558, 2010.

[192] Z. Zhu, Y. Cheng, and U. Schwingenschlögl, "Topological phase transition in layered GaS and GaSe," *Physical Review Letters*, vol. 108, no. 26, p. 266805, 2012.

[193] W. An, F. Wu, H. Jiang, G.-S. Tian, and X.-Z. Li, "Systematic investigation on topological properties of layered *gas* and *gase* under strain," *The Journal of chemical physics*, vol. 141, no. 8, p. 084701, 2014.

[194] Y. L. Chen, J. G. Analytis, J.-H. Chu, Z. K. Liu, S.-K. Mo, X. L. Qi, H. J. Zhang, D. H. Lu, X. Dai, Z. Fang, S. C. Zhang, I. R. Fisher, Z. Hussain, and Z.-X. Shen, "Experimental realization of a three-dimensional topological insulator, $Bi2Te3$," *Science*, vol. 325, no. 5937, pp. 178–181, 2009. [Online]. Available: http://www.sciencemag.org/content/325/5937/178.abstract

[195] G. Yin, D. Wickramaratne, and R. K. Lake, "Tunneling spectroscopy of chiral states in ultra-thin topological insulators," *Journal of Applied Physics*, vol. 113, no. 6, p. 063707, 2013.

[196] J. Checkelsky, Y. Hor, R. Cava, and N. Ong, "Bulk band gap and surface state conduction observed in voltage-tuned crystals of the topological insulator Bi2Se3," *Physical Review Letters*, vol. 106, no. 19, p. 196801, 2011.

[197] Y. Zhang, K. He, C.-Z. Chang, C.-L. Song, L.-L. Wang, X. Chen, J.-F. Jia, Z. Fang, X. Dai, W.-Y. Shan, S.-Q. Shen, Q. Niu, X.-L. Qi, S.-C. Zhang, X.-C. Ma, and Q.-K. Xue, "Crossover of the three-dimensional topological insulator

Bi2Se3 to the two-dimensional limit," *Nature Physics*, vol. 6, no. 8, pp. 584–588, 2010.

[198] W. Liu, X. Peng, X. Wei, H. Yang, G. M. Stocks, and J. Zhong, "Surface and substrate induced effects on thin films of the topological insulators Bi2Se3 and Bi2Te3," *Physical Review B*, vol. 87, no. 20, p. 205315, 2013.

[199] Y. Zhang, T.-T. Tang, C. Girit, Z. Hao, M. C. Martin, A. Zettl, M. F. Crommie, Y. R. Shen, and F. Wang, "Direct observation of a widely tunable bandgap in bilayer graphene," *Nature*, vol. 459, no. 7248, p. 820, 2009.

[200] E. McCann, "Asymmetry gap in the electronic band structure of bilayer graphene," *Phys. Rev. B*, vol. 74, p. 161403R, 2006. [Online]. Available: dx.doi.org/10.1103/PhysRevB.74.161403

[201] M. Calandra, "Chemically exfoliated single-layer mos 2: Stability, lattice dynamics, and catalytic adsorption from first principles," *Physical Review B*, vol. 88, no. 24, p. 245428, 2013.

[202] Y. Ge and A. Y. Liu, "Effect of dimensionality and spin-orbit coupling on charge-density-wave transition in 2h-tase$_2$," *Phys. Rev. B*, vol. 86, p. 104101, Sep 2012. [Online]. Available: http://link.aps.org/doi/10.1103/PhysRevB.86.104101

[203] ——, "First-principles investigation of the charge-density-wave instability in 1T-TaSe 2," *Physical Review B*, vol. 82, no. 15, p. 155133, 2010.

[204] G. Li, W. Z. Hu, D. Qian, D. Hsieh, M. Z. Hasan, E. Morosan, R. J. Cava, and N. L. Wang, "Semimetal-to-semimetal charge density wave transition in

$1T$-TiSe$_2$," *Phys. Rev. Lett.*, vol. 99, p. 027404, Jul 2007. [Online]. Available: http://link.aps.org/doi/10.1103/PhysRevLett.99.027404

[205] F. J. Di Salvo, D. E. Moncton, and J. V. Waszczak, "Electronic properties and superlattice formation in the semimetal tise$_2$," *Phys. Rev. B*, vol. 14, pp. 4321–4328, Nov 1976. [Online]. Available: http://link.aps.org/doi/10.1103/PhysRevB.14.4321

[206] T. E. Kidd, T. Miller, M. Y. Chou, and T.-C. Chiang, "Electron-hole coupling and the charge density wave transition in TiSe$_2$," *Phys. Rev. Lett.*, vol. 88, p. 226402, May 2002. [Online]. Available: http://link.aps.org/doi/10.1103/PhysRevLett.88.226402

[207] J. C. E. Rasch, T. Stemmler, B. Müller, L. Dudy, and R. Manzke, "$1T$-TiSe$_2$: Semimetal or semiconductor?" *Phys. Rev. Lett.*, vol. 101, p. 237602, Dec 2008. [Online]. Available: http://link.aps.org/doi/10.1103/PhysRevLett.101.237602

[208] M. Cazzaniga, H. Cercellier, M. Holzmann, C. Monney, P. Aebi, G. Onida, and V. Olevano, "*Ab initio* many-body effects in TiSe$_2$: A possible excitonic insulator scenario from gw band-shape renormalization," *Phys. Rev. B*, vol. 85, p. 195111, May 2012. [Online]. Available: http://link.aps.org/doi/10.1103/PhysRevB.85.195111

[209] M. H. Whangbo and E. Canadell, "Analogies between the concepts of molecular chemistry and solid-state physics concerning structural instabilities. electronic origin of the structural modulations in layered transition metal dichalcogenides," *Journal of the American Chemical Society*, vol. 114, no. 24, pp. 9587–9600, 1992. [Online]. Available: http://pubs.acs.org/doi/abs/10.1021/ja00050a044

[210] H. P. Hughes, "Structural distortion in TiSe2 and related materials-a possible jahn-teller effect?" *Journal of Physics C: Solid State Physics*, vol. 10, no. 11, p. L319, 1977. [Online]. Available: http://stacks.iop.org/0022-3719/10/i=11/a=009

[211] T. Pillo, J. Hayoz, H. Berger, F. Lévy, L. Schlapbach, and P. Aebi, "Photoemission of bands above the fermi level: The excitonic insulator phase transition in $1T - \mathrm{TiSe}_2$," *Phys. Rev. B*, vol. 61, pp. 16 213–16 222, Jun 2000. [Online]. Available: http://link.aps.org/doi/10.1103/PhysRevB.61.16213

[212] Z. Zhu, Y. Cheng, and U. Schwingenschlögl, "Origin of the charge density wave in $1T$-TiSe_2," *Phys. Rev. B*, vol. 85, p. 245133, Jun 2012. [Online]. Available: http://link.aps.org/doi/10.1103/PhysRevB.85.245133

[213] J. Ishioka, Y. H. Liu, K. Shimatake, T. Kurosawa, K. Ichimura, Y. Toda, M. Oda, and S. Tanda, "Chiral charge-density waves," *Phys. Rev. Lett.*, vol. 105, p. 176401, Oct 2010. [Online]. Available: http://link.aps.org/doi/10.1103/PhysRevLett.105.176401

[214] J. van Wezel, "Chirality and orbital order in charge density waves," *EPL (Europhysics Letters)*, vol. 96, no. 6, p. 67011, 2011. [Online]. Available: http://stacks.iop.org/0295-5075/96/i=6/a=67011

[215] T. Rohwer, S. Hellmann, M. Wiesenmayer, C. Sohrt, A. Stange, B. Slomski, A. Carr, Y. Liu, K. M. S. M. L. K. K. R. Avila, Luis Miaja, and M. Bauer, "Collapse of long-range charge order tracked by time-resolved photoemission at high momenta," *Nature*, vol. 471, no. 7339, pp. 490–493, 2011.

[216] G. Kresse and J. Hafner, "Ab initio molecular dynamics for liquid metals," *Phys. Rev. B*, vol. 47, no. 1, pp. 558–561, Jan 1993.

[217] S. S. Jaswal, "Lattice dynamics of TiSe$_2$," *Phys. Rev. B*, vol. 20, pp. 5297–5300, Dec 1979. [Online]. Available: http://link.aps.org/doi/10.1103/PhysRevB.20.5297

[218] http://merritt.cdlib.org/m/ucr_bcoe_2dmaterials.

[219] http://merritt.cdlib.org/help/aboutmerritt.